High-Energy and High-Power Multi-Octave Pulse Generation

Haochuan Wang

München 2020

High-Energy and High-Power Multi-Octave Pulse Generation

Haochuan Wang

Dissertation
an der Fakultät für Physik
der Ludwig–Maximilians–Universität
München

vorgelegt von
Haochuan Wang
aus Zhejiang, China

München, den 30 Juni 2020

Erstgutachter: Prof. Dr. Ferenc Krausz
Zweitgutachter: Prof. Dr. Oleg Pronin
Tag der mündlichen Prüfung: 09.10.2020

献给一路默默支持我的妻子：鑫

工欲善其事，必先利其器。

—— 孔子《论语》

The mechanic, who wishes to do his work well, must first sharpen his tools.

—— Analects of Confucius

Zusammenfassung

Die Ultrakurzzeit-Spektroskopie unter Anwendung von Laserpulsen auf äußerst kurzen Zeitskalen (Attosekunden bis Femtosekunden) ermöglichte die Untersuchung von elektronischen oder molekularen Dynamiken in physikalischen und chemischen Prozessen. Der Fortschritt in der Attosekunden- und Femtosekunden-Spektroskopie profitiert direkt von der Verfügbarkeit von Ultrabreitband-Pulsen bei hoher Spitzen- und Durchschnittsleistung, um nichtlineare Interaktionen effizient auszulösen und die Messempfindlichkeit zu erhöhen. Heutige Yb:YAG Laser können Pulse mit verschiedensten Energien und Wiederholraten erzeugen und dabei eine deutlich höhere Durchschnittsleistung als Ti:Sa Laser erreichen. Der schmalbandige Emissionsquerschnitt und der Gain-Narrowing-Effekt begrenzen jedoch ihre Pulsdauer. In dieser Arbeit wird die Erzeugung von Ultrabreitband-Pulsen mit einem Yb:YAG Laser in zwei verschiedenen Bereichen gezeigt: (I) Hochenergetischer Kilohertz-Bereich und (II) niederenergetischer Megahertz-Bereich.

Im hochenergetischen Kilohertz-Bereich, aufbauend auf dem Konzept der parallelen Feldsynthese, ist die Kombination von optischer parametrischer Verstärkung mit Yb:YAG Lasern für die gleichzeitige Skalierung von Energie und Leistung von Lichttransienten vielversprechend. In dieser Hinsicht wird ein mehrere Oktaven breites Superkontinuum mit einer stabilen Träger-Einhüllenden-Phase erzeugt, das den Wellenlängenbereich vom sichtbaren bis zum nahen Infrarot abdeckt, um einen parellelen Feld-Synthesizer zu speisen. Die Verstärkung des Superkontinuums in zwei einstufigen optischen parametrischen Verstärkern ergibt 18 fs Pulse bei 2 μm, und 6 fs bei 1 μm. Die kohärente Synthese dieser Pulse könnte 3 fs, 25 μJ Lichttransienten ergeben. Einer numerischen Untersuchung zufolge lässt sich die Energie der Lichttransienten bis zu 4 mJ skalieren, indem man die verbleibende Energie der Yb:YAG Laser nutzt, um zusätzliche optische parametrische Verstärker zu pumpen. Solch ein breitbandiger phasenstabiler Laser bietet auch ein enormes Potential für die Spektroskopie, insbesondere im Bereich der feldauflösenden Spektroskopie im nahen Infrarot. Die kurzen Pulse des Frontends werden zum ersten mal für die feldaufgelöste Spektroskopie der Kombinationsbänder von Wassermolekülen genutzt. Schließlich wird eine neue Variante der Feldsynthese basierend auf kreuzpolarisierten Superkontinua vorgeschlagen und numerisch untersucht. Flexibel anpassbare Lichtransienten mit hoher Spitzen- und Durchschnittsleistung können mit diesen Quellen erzeugt werden und stellen eine aussichtsreiche

Möglichkeit dar, die Attosekunden- und Hochfeldphysik weiter voranzubringen.

Laser mit hohen Wiederholraten sind in der Spektroskopie vorteilhaft, um das Signal-Rausch-Verhältnis zu erhöhen und die die Messzeit zu reduzieren. Daher wird eine breitbandige und kohärente Quelle mit einer Wiederholrate von 16 Megahertz entwickelt. Dank der Verwendung einer externen nichtlinearen spektralen Verbreiterung auf Grundlage einer festkörperbasierten Multipass-Kompression und einer gasgefüllten photonischen Kristall-Hohlfaser werden die 265 fs Pulse eines 6 μJ Yb:YAG Dünnscheiben-Ozillators auf 9 fs komprimiert. Die spektrale Abdeckung der Quelle wird mit einer Intra-Puls Differenzfrequenzerzeugung von Femtosekundenpulsen in einem phasenangepassten $LiGaS_2$ (LGS) Kristall und in zufällig quasi-phasenangepassten ZnSe und ZnS Polykristallen zum mittleren Infrarot erweitert. Die Verfügbarkeit von Terahertz-Pulsen mit einer höheren Durchschnittsleistung und Wiederholrate ist von großer Bedeutung für zahlreiche Terahertz-Anwendungen. Die optische Gleichrichtung von Femtosekundenpulsen hoher Leistung wird daher in Galliumphosphid demonstriert. Solche eine breitbandige kohärente Pulserzeugung vom sichtbaren bis zum Terahertz Bereich bei MHz Wiederholrate ist ein bedeutsamer Schritt hin zu einer Spektroskopie mit einem höherem Signal-Rausch-Verhältnis.

Abstract

Ultrafast spectroscopy employing laser pulses on extremely short time scales (attoseconds to femtoseconds) enabled the study of electronic or molecular dynamics in physical and chemical processes. Advancements in attosecond and femtosecond spectroscopies benefit directly from the availability of ultra-broadband pulses at high peak and average power to trigger nonlinear interactions efficiently and to enhance the detection sensitivity. Nowadays, Yb:YAG lasers are capable of delivering pulses at a variety of energies and repetition rates, with a much higher output power compared to Ti:Sa lasers. However, the narrowband emission cross-section in addition to the gain narrowing limits their pulse duration. In this thesis, ultra-broadband pulse generation from Yb:YAG lasers at two different regimes are demonstrated: (I) High-energy kilohertz regime and (II) Low-energy, megahertz regime.

In high-energy kilohertz regime, based on the concept of parallel field synthesis, combining optical parametric chirped pulse amplification and Yb:YAG lasers holds promise for simultaneous scaling of energy and power of light transients. In this regard, a carrier envelope phase-stable, multi-octave supercontinuum covering visible to near-infrared wavelength range is generated to seed a parallel field synthesizer. Amplification of the supercontinuum in two single-stage optical parametric chirped-pulse amplifiers yield 18 fs pulses at 2 μm, and 6 fs pulse at 1 μm. Coherent synthesis of these pulses could result in 3 fs, 25 μJ light transients. According to numerical investigation, the energy of the light transients can be scaled to 4 mJ by using the remaining energy of the Yb:YAG laser to pump additional optical parametric amplifiers. Such a broadband phase-stable laser also provides enormous potential for spectroscopy, especially field-resolved near-infrared spectroscopy. The short pulses of the frontend are used for field-resolved spectroscopy of combination bands in water molecules for the first time. Lastly, a new type of field synthesis based on cross-polarized supercontinuum is proposed and numerically studied. High peak- and average-power tailored light transients from these sources holds great potential in advancing attosecond and high-field physics.

High repetition rate lasers are desired in spectroscopy to increase the signal-to-noise ratio and reduce data acquisition time. Therefore, a broadband and coherent source operating at 16 megahertz repetition rate is developed. By employing external nonlinear spectral broadening based on a multi-pass bulk compression and gas-filled hollow-core photonic

crystal fiber, the 265 fs pulses of a 6 μJ Yb:YAG thin-disk oscillator are compressed to 9 fs. The spectral coverage of the source is extended to mid-infrared by intra-pulse difference-frequency generation of few-cycle pulses in a phase-matched $LiGaS_2$ (LGS) crystal and random quasi-phase-matched ZnSe and ZnS polycrystals. Availability of terahertz pulses with a higher average power and repetition rate is of great interest to various terahertz applications. In this regard, optical rectification in gallium phosphide crystal driven by high power few-cycle pulses is demonstrated. Such broadband coherent pulse generation from visible to terahertz range at MHz repetition rate holds promise to pave the way for spectroscopy at a higher signal-to-noise ratio.

Contents

List of Figures

List of Tables

List of Abbreviations

AGS	$AgGaS_2$
AOPDF	acousto-optic programmable dispersive filter
AR	anti-reflective
BaF_2	barium fluoride
BBO	beta barium borate
BiBO	bismuth borate
BOC	balanced optical cross-correlation
CaF_2	Calcium fluoride
CCD	charge-coupled device
CEP	carrier-envelope phase
CPA	chirped pulse amplification
CW	continuous wave
DFG	difference-frequency generation
DOPA	degenerate optical parametric amplification
EOS	electro-optic sampling
FID	free-induction decay
FROG	frequency-resolved optical gating
FS	fused silica
FTIR	Fourier transform infrared
FTL	Fourier transform limit
FW	fundamental wave
FWHM	full width at half maximum
FWM	four-wave mixing
FOPA	frequiency domain optical parametric amplification
FRS	field-resolved spectroscopy
GaP	Gallium Phosphide
Ge	Germanium

GD	group delay
GDD	group delay dispersion
GVD	group velocity dispersion
GaSe	gallium selenide
HCF	hollow-core fiber
HC	Herriott-type imaging cell
HHG	high-harmonic generation
IAP	isolated attosecond pulse
IPDFG	intra-pulse difference frequency generation
KLM	Kerr-lens mode-locking
keV	kiloelectronvolt
LBO	lithium triborate
LGS	$LiGaS_2$
LGSe	$LiGaSe_2$
$LiNbO_3$	lithium niobate
LIS	$LiInS_2$
LISe	$LiInSe_2$
MIR	mid-infrared
MgF2	Magnesium fluoride
MHz	megahertz
MW	megawatt
NIR	near-infrared
NOPA	non-collinear optical parametric amplification
OPA	optical parametric amplification
OPCPA	optical parametric chirped pulse amplification
OPO	optical parametric oscillator
PCF	photonic crystal fiber
PPLN	periodically poled lithium niobate
QPM	Quasi-phase-matching
RMS	root mean square
ROC	radius of curvature
RQPM	Random Quasi-phase-matching
SAM	self-amplitude modulation
SC	supercontinuum
SESAM	semiconductor saturable absorber mirror

SFG	sum-frequency generation
SH	second-harmonic
SH-FROG	second-harmonic frequency-resolved optical gating
SHG	second-harmonic generation
SISYFOS	Simulation System for Optical Science
SNR	signal-to-noise ratio
SPM	self-phase modulation
SR-PCF	single-ring hollow-core photonic-crystal fiber
TD	thin-disk
TFP	thin-film polarizer
THG	third-harmonic generation
THz	terahertz
Ti:Sa	titanium-doped sapphire
TOD	third-order dispersion
UV	ultraviolet
VIS	visible
XPM	cross-phase modulation
XPW	cross-polarized wave
YAG	yttrium aluminum garnet
Yb:YAG	ytterbium-doped yttrium aluminum garnet
ZDW	zero dispersion wavelength
ZnS	zinc sulfide
ZnSe	zinc selenide

Chapter 1

Introduction

Ever since human beings learned to use fire in the ancient time, light sources always accompanied us in exploring the world around us. Sources like sun or fire emit light with a huge bandwidth, however, not coherent. Since the first demonstration of laser by Theodore Maiman in 1960 [1], such coherent source played important roles in numerous applications with various bandwidth. On one hand, for precision measurement, narrow linewidth ultra-stable lasers were used in LIGO's laser interferometer which enabled measuring tiny changes in spatial distances when a gravitational wave passed through [2]. On the other hand, to resolve the fastest processes in nature, broadband lasers emitting ever shorter pulses opened door to many applications in physics, chemistry and biology [3–7].

Based on the Fourier theory, the pulse duration is inversely proportional to the spectral bandwidth. The shorter the pulse duration, the broader the spectral bandwidth has to be. Besides, it also depends on the central frequency of the spectrum. However, the bandwidth of a laser is limited to its emission cross-section, and is often not easily tunable. To overcome this limitation, different approaches have been introduced to broaden the spectrum or convert the laser energy to desired wavelength while at the same time preserving the advantageous properties, like short pulse duration, good spatial profile, and the coherence.

The invention of titanium-doped sapphire (Ti:Sa) oscillators, Kerr-lens mode-locking (KLM), and multi-layer chirped mirrors enabled few-cycle sub-10 fs pulse generation [8–12]. With chirped pulse amplification (CPA) the peak power of such pulses could be amplified by orders of magnitude [13]. External spectral broadening of few-cycle, mJ-level pulses of a CPA-based amplifier in a hollow-core fiber (HCF) and their subsequent pulse compression resulted in 4 fs pulses at 800 nm carrier wavelength [14]. With the ability to control the carrier-envelope phase (CEP) of such few-cycle pulses, the first isolated attosecond pulse (IAP) was demonstrated and led to a new research field of attosecond physics [4]. However, due to the excessive ionization, thermal instabilities and damage in the HCF, the highest possible peak power is limited to 1 TW and the average power is limited to 10 W [15, 16]. Although the broadened spectrum from HCF supported a

shorter pulse duration, the bandwidth limitation of one-octave imposed by chirped mirrors restricted the compressed pulses to 4 fs. Light field synthesis can overcome this limitation by dividing the ultra-broadband spectrum from the HCF into several spectral regions [17], with individual compression of each spectral region and their coherent superposition, sub-cycle light transients could be generated.

Nowadays, ytterbium-doped yttrium aluminum garnet (Yb:YAG) lasers in rod, slab, fiber or thin-disk geometry [18] are delivering higher average and peak powers compared to Ti:Sa lasers. However, the narrow-band emission cross-section [19] in addition to the gain narrowing limit their pulse duration to several picoseconds at joule and hundreds of femtoseconds at μJ energy. Various applications would greatly benefit from their pulse compression to few-cycle regime at different central frequencies. In this thesis, ultra-broadband pulse generation from Yb:YAG lasers at two different regimes are studied:

(I) High-energy kilohertz regime: Yb:YAG amplifiers in thin-disk geometry are capable of delivering high energy pulses up to 200 mJ at 5 kHz [20]. Based on the concepts introduced in [21, 22], combining optical parametric chirped pulse amplification (OPCPA), Yb:YAG pump lasers and coherent field synthesis holds promise for simultaneous scaling of energy and power of light transients. Such high-energy light transients can be used to generate attosecond pulses efficiently. It's been shown that by temporal field synthesis of a few-cycle pulse at 2 μm and weaker few-cycle pulses at its second and third harmonics, optimized, non-sinusoidal light transients can be generated [23]. Such non-sinusoidal light transients at mJ-level, hold promise to extend the cutoff energy in high-harmonic generation (HHG) to kiloelectronvolt (keV) regime at higher photon flux [24].

Not only high-energy physics benefits from the broadband lasers developed in this spectral range. There is also enormous potential for spectroscopy. Recently it's been shown the detection limits in broadband transmission spectroscopy of biological systems in aqueous environment can be overcome by field-resolved spectroscopy (FRS) in MIR [25]. In this approach, waveform-stable, few-cycle MIR pulses are used to impulsively excite molecular vibrations, by electro-optic sampling (EOS) of the electric-field emitted in the wake of the excitation pulse, the retarded molecular signal is isolated from the excitation background, which results in an enhanced sensitivity and dynamic range.

Similar information to infrared spectroscopy can be obtained in near-infrared (NIR) spectroscopy by exciting the first overtone of infrared-active vibrational modes, providing similar information on the molecular composition, structure, and conformation. For example, NIR spectroscopy is routinely used for the detection of the overtone and combination bands of the C-H, O-H, and N-H compositions. As the NIR spectral range supports a smaller diffraction limit than infrared, molecular information with higher spatial resolution can be obtained. Moreover, the lower cross-section of the overtone excitation allows for deeper penetration of the injected field to the sample, allowing for in-depth spectral

imaging. Therefore NIR spectroscopy offers great potential for high-resolution, in-depth, label-free biological spectro-microscopy.

In this thesis for the first time, field-resolved spectroscopy at NIR spectral range is shown. Here, molecules are excited with NIR, CEP-stable ultrashort pulses, and the transmitted complex electric field of NIR pulses, which contains the molecular response is measured directly by EOS. Therefore, field-resolved NIR spectroscopy allows for the extraction of full spectral phase information of the molecular response, adding a new dimension to the gained spectroscopic data. Similar to FRS reported in [25], due to the short pulse duration used for excitation, and the delayed response of the sample known as free-induction decay (FID), the molecular response is detected free of background, eliminating the influence of the intensity noise of the laser source.

The demonstrated experiment operates at kHz repetition rate. However, to increase the signal-to-noise ratio and reduce data acquisition time, higher repetition rates are desired. Therefore, novel, intense, broadband and coherent sources operating at megahertz (MHz) repetition rate, are required to enable resolving signals which were below the noise floor of previous experiments. The development of such sources is the focus of the second part of this thesis.

(II) Low-energy, megahertz regime: Yb:YAG mode-locked oscillators in thin-disk geometry at multi-MHz repetition rate are capable of delivering up to 155 watts pulses with 140 fs pulse duration [26]. Nonlinear external compression can be used to shorten the output pulses from the oscillator. Nonlinear propagation inside gas-filled HCF [27] and filamentation in noble gas [28] have been methods of choice due to their homogeneous spectral broadening. However, these approaches require high pulse energy (>100 μJ), which is beyond the capability of high power Yb:YAG mode-locked oscillators. Large mode area silica photonic crystal fiber (PCF) has shown large pulse compression factor at high average power [29–31], but is limited to low peak power due to the self-focusing in silica. Compressing of high average- and peak-power pulses (tens of megawatt (MW)) has been shown in gas-filled hollow-core Kagome PCF [32, 33]. However this requires specially designed hollow-core Kagome PCF, gas chamber and very well controlled beam pointing at the PCF entrance. Alternatively, spectral broadening in bulk can be used [34, 35]. However, this technique suffers from low efficiency and spatial chirp.

In 2016, a new scheme to overcome the spatial inhomogeneity with an improved optical-to-optical conversion efficiency was demonstrated [36]. In this scheme the beam propagates in a geometry similar to an optical cavity, while the self-phase modulation (SPM) is induced via multiple passes through a nonlinear medium placed inside the cavity. The nonlinear phase shift is kept much smaller than π for each pass. The final spectral bandwidth is defined by the total accumulated nonlinear phase shift, while only the fundamental spatial mode survives the optical cavity at the output. Based on this method, more than 90%

optical-to-optical efficiency with 10-fold spectral broadening and 5-fold temporal compression was demonstrated [36–38]. Combining Herriot-cells with the resonator stability condition around the nonlinear medium enables a table-top setup with more than 50 passes through the nonlinear medium [37]. Using multiple Herriot-cells, a further increase of the spectral broadening factor to 22 was demonstrated [39].

In this thesis, the temporal compression of 265 fs pulses from a 100 W Yb:YAG thin-disk oscillator [26] to 18 fs by employing two external nonlinear spectral broadening stages [40] is demonstrated. In order to further extend the spectral bandwidth towards sub-5 fs regime, external nonlinear spectral broadening stage based on gas filled single-ring hollow-core photonic crystal fiber (SR-PCF) is developed [40, 41].

While these efforts concentrated on extending the spectral bandwidth at the oscillator's central frequency to generate ultra-short pulses in NIR, two techniques are studied to extend the generated spectrum towards MIR. Compressed short pulses at NIR are used to drive phase-matched intra-pulse difference frequency generation (IPDFG) in $LiGaS_2$ (LGS) crystal and Random Quasi-phase-matching (RQPM) IPDFG in polycrystalline zinc selenide (ZnSe) and zinc sulfide (ZnS). Finally, extension of the bandwidth of the laser to terahertz (THz) by optical rectification in Gallium Phosphide (GaP) driven by high power few-cycle pulses is demonstrated.

1.1 Thesis outline

The thesis is outlined as following:

Chapter 2: introduces briefly the fundamentals of nonlinear processes, which are closely related to this thesis.

Chapter 3: presents the development of a 5 kHz repetition rate system for high-energy light field synthesis and its first application in field-resolved NIR spectroscopy. In the first section, high-energy parallel field synthesis is introduced. A home-built, diode-pumped Yb:YAG thin-disk regenerative amplifier is introduced. Design and implementation of a CEP-stable multi-octave seed generation setup is described. The possibility of extending the spectrum of CEP-stable seed pulses towards MIR is discussed and numerically simulated. Afterwards, broadband optical parametric amplification centered at 2 μm and 1 μm with the compression of amplified pulses down to 18 fs and 6 fs respectively are presented. EOS for resolving electric field of the amplified 2 μm pulses is shown, and the relative timing fluctuations between the two arms of the synthesizer are discussed. Furthermore, the concept and proof of principle experiment of NIR field-resolved spectroscopy are proposed and experimentally explored. In the second section, the new concept of cross-polarized synthesis is introduced and numerically studied. Moreover, generation of a super-octave seed pulse with mixed polarization, required in this scheme is demonstrated experimentally.

Chapter 4: is devoted to the development of a multi-MHz repetition rate system to overcome the limitation of signal-to-noise ratio and long measurement time posed by the low repetition rate. The chapter starts with description on a high power Yb:YAG thin-disk oscillator and the following broadening stages based on Herriott-type imaging cell (HC) and single-ring hollow-core photonic crystal fiber (SR-PCF). Afterwards, MIR generation via IPDFG in different mediums are presented and characterized by EOS. Furthermore, super-octave high average power THz generation in GaP is demonstrated.

Chapter 5: summarises the results and conclude the thesis with future developments, and improvements.

Chapter 2

Theoretical Background

In this chapter, a brief introduction of the ultrafast and nonlinear optics theory related to this work is given. There are several excellent classical textbooks and review articles providing a thorough and insightful overview of the field, a few examples are Ref. [3, 42–49]. Part of this chapter is adapted from Ref. [42, 45, 47, 48].

2.1 Ultrashort pulse fundamentals

A linear polarized ultrashort pulse at a fixed position in space can be described by its time dependent electric field:

$$E(t) \;=\; A(t)\,cos\big(\phi(t)\big) \;\;=\; \frac{1}{2}\,A(t)\,e^{i\,(\omega_0 t+\phi_a(t)+\phi_0)} \;+\; c.c. \tag{2.1}$$

where $A(t)$ is the temporal amplitude or envelope, $\phi(t)$ is the temporal phase, ω_0 is the carrier frequency, $\phi_a(t)$ is a time dependent phase function and ϕ_0 is an absolute phase or carrier-envelope phase(CEP). The pulse duration is defined by the full width at half maximum (FWHM) of the temporal intensity

$$I(t) \;=\; \frac{1}{2}\,\varepsilon_0\,c\,n\,A(t)^2 \tag{2.2}$$

where ε_0 is the vacuum permitivity, c is the speed of light and n is the refractive index.

To simplify the mathematics, it is often convenient to ignore the complex conjugate term in Eq. 2.1, therefore yields the complex analytic signal

$$E^+(t) \;=\; A(t)\,e^{i\,(\omega_0 t+\phi_a(t)+\phi_0)} \tag{2.3}$$

Fourier transform of the complex analytic signal $E^+(t)$ gives the complex electric field

in the frequency domain:

$$\tilde{E}^{+}(\omega) \;=\; \int_{-\infty}^{\infty} E^{+}(t)\, e^{-i\,\omega\, t}\, dt \tag{2.4}$$

where $\tilde{E}^{+}(\omega)$ has nonzero values only for positive values of the frequency ω, and can be separated into amplitude and phase terms

$$\tilde{E}^{+}(\omega) \;=\; \sqrt{S(\omega)}\, e^{-i\varphi(\omega)} \tag{2.5}$$

where $S(\omega)$ is the spectral intensity and $\varphi(\omega)$ is the spectral phase.

The temporal phase $\phi(t)$ in Eq. 2.1 contains frequency vs. time information, and the instantaneous frequency is defined as

$$\omega_{inst}(t) \;=\; \frac{d\phi\,(t)}{dt} \;=\; \omega_0 + \frac{d\phi_a\,(t)}{dt} \tag{2.6}$$

Similarly the spectral phase contains time vs. frequency information, and it's common to expand $\varphi(\omega)$ in a Taylor series around ω_0:

$$\varphi(\omega) \;=\; \sum_{j=0}^{\infty} \frac{\varphi^{(j)}(\omega_0)}{j!}\cdot(\omega-\omega_0)^{j} \tag{2.7}$$

with the spectral phase coefficients usually denoted by D_j:

$$\varphi^{(j)}(\omega_0) \;=\; D_j(\omega_0) \;=\; \left.\frac{\partial^{j}\varphi(\omega)}{\partial\omega^{j}}\right|_{\omega_0} \tag{2.8}$$

The zeroth order phase term $D_0 = \varphi(\omega_0)$ is the counterpart of the CEP in time domain ($\phi_0 = -\varphi(\omega_0)$). It describes the relative phase of carrier wave with respect to the envelope (Fig. 2.1a). In the frequency domain, a pulse train is represented by a frequency comb, CEP corresponds to a shift called carrier-envelope offset frequency f_{CEO} imposed on the equally spaced frequency comb (Fig. 2.1b). While the CEP has negligible effect on the pulse shape for longer duration pulses, the influence become significant on few-cycle pulses as shown in Fig. 2.1a. The measurement and control of CEP are essential for studying light-matter interactions in the few-cycle regime [50, 51] and for frequency metrology using frequency combs [52]. In this work, CEP-stable few-cycle pulses play an important role in generating stable light transients [17, 53] and in field-resolved measurements [30, 53, 54]. CEP can be tracked and active-stabilized in oscillators by self-referencing schemes like f-to-2f [55, 56]. Or alternatively passive stabilized by employing nonlinear interection of difference-frequency generation (DFG) [50], which will be discussed later.

The first-order term $D_1 = \frac{\partial\varphi(\omega)}{\partial\omega}|_{\omega_0}$ is known as group delay (GD), which leads to a temporal delay of the pulse envelop in the time domain. While the higher order coefficients

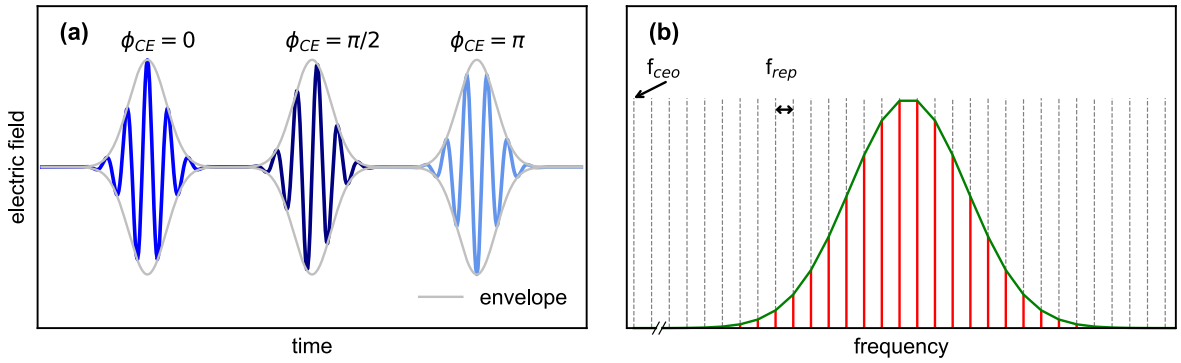

Figure 2.1: (a) CEP influence on few-cycle pulses for $\phi_{CE} = 0$ (blue pulse), $\phi_{CE} = \pi/2$ (dark blue pulse) and $\phi_{CE} = \pi$ (light blue pulse). (b) In frequency domain, CEP corresponds to a shift of carrier-envelope offset frequency f_{CEO} imposed on the equally spaced frequency comb.

changes the temporal structure of the electric field. The second order term $D_2 = \frac{\partial^2 \varphi(\omega)}{\partial \omega^2}|_{\omega_0}$ is known as the group delay dispersion (GDD), and results in the linear chirp of the laser pulse. The third order term $D_3 = \frac{\partial^3 \varphi(\omega)}{\partial \omega^3}|_{\omega_0}$ is known as the third-order dispersion (TOD), and leads to asymmetric temporal pulse shapes. Precise control of the spectral phase $\varphi(\omega)$ in the experiment creates changes in the real electric field strength $E(t)$, and can be obtained by material propagation, prisms, gratings, chirped mirrors or adaptive optics [57].

2.2 Perturbative nonlinear optics

In ultrashort pulses the entire energy of the radiation field is concentrated in a very short time interval, resulting in high peak power and intensity. Therefore, ultrashort pulses propagating in a medium, easily experience high intensity effects – nonlinear optical effects.

As a special form of electromagnetic fields, the propagation of optical pulses can be described by the wave equation derived from the Maxwell's equations. Consider a linearly polarized plane wave $E(z,t)$ propagating through a medium in the direction of z. The wave equation can be expressed as:

$$\frac{\partial^2 E(z,t)}{\partial z^2} - \frac{1}{c_0^2}\frac{\partial^2 E(z,t)}{\partial t^2} = \mu_0 \frac{\partial^2 P(z,t)}{\partial t^2} \tag{2.9}$$

where $E(z,t)$ is the electric field, $P(z,t)$ is the induced polarization, μ_0 is the permeability in vacuum and c_0 is the speed of light in vacuum. The induced polarization $P(z,t)$

can be written as

$$\begin{aligned} P(z,t) &= \varepsilon_0 \chi^{(1)} E(z,t) + \varepsilon_0 \chi^{(2)} E^2(z,t) + \varepsilon_0 \chi^{(3)} E^3(z,t) + \dots \\ &= P^{(1)}(z,t) + P^{NL}(z,t) \end{aligned} \tag{2.10}$$

where $\chi^{(1)}$ is the linear susceptibility, and $\chi^{(2)}$ and $\chi^{(3)}$ are the second-order and third-order nonlinear susceptibilities of the material, respectively. The right-hand side of Eq. 2.10 can be split into the liner part of the polarization $P^{(1)}(z,t)$ and the nonlinear part of the polarization $P^{NL}(z,t)$ induced by strong electric field.

Consider Eq. 2.10 and the electric displacement field due to the linear polarisation of the material $D(z,t) = \varepsilon_0 E(z,t) + P^{(1)}(z,t)$, the general form of the wave equation with nonlinear processes can be expressed as:

$$\frac{\partial^2 E(z,t)}{\partial z^2} - \mu_0 \frac{\partial^2 D(z,t)}{\partial t^2} = \mu_0 \frac{\partial^2 P^{NL}(z,t)}{\partial t^2} \tag{2.11}$$

The right-hand side of the Eq. 2.11 acts as a source term, and is the origin of various nonlinear optical effects.

2.2.1 Second-order nonlinear processes

When consider only the second order nonlinear optical effects, the nonlinear polarization reduce to

$$P^{NL}(z,t) = P^{(2)}(z,t) = \varepsilon_0 \chi^{(2)} E^2(z,t) = 2\varepsilon_0 d_{eff} E^2(z,t) \tag{2.12}$$

where d_{eff} is the effective nonlinear optical coefficient and depends on the specific components of the $\chi^{(2)}$. In the general case of second-order nonlinearity, where three interacting monochromatic waves at distinct frequencies propagate along the z-direction. The electric field can be represented in the form of

$$E(z,t) = \frac{1}{2}\left[A_1(z)\, e^{i(\omega_1 t - k_1 z)} + A_2(z)\, e^{i(\omega_2 t - k_2 z)} + A_3(z)\, e^{i(\omega_3 t - k_3 z)}\right] + c.c. \tag{2.13}$$

Replacing the electric field in $P^{NL}(z,t) = 2\varepsilon_0 d_{eff} E^2(z,t)$ with its expression in Eq. 2.13, the second order polarization response has spectral contributions at the fowllowing frequencies:

$$\underbrace{2\omega_1,\, 2\omega_2,\, 2\omega_3}_{SHG},\, \underbrace{\omega_1+\omega_2,\, \omega_1+\omega_3,\, \omega_2+\omega_3}_{SFG},\, \underbrace{\omega_3-\omega_1,\, \omega_3-\omega_2,\, \omega_2-\omega_1}_{DFG} \tag{2.14}$$

Here only the terms at frequencies $\omega_1+\omega_2\,(=\omega_3)$, $\omega_3-\omega_2\,(=\omega_1)$ and $\omega_3-\omega_1\,(=\omega_2)$ are considered, those could satisfy the phase-matching condition. The resulting forcing term

$\partial^2 P^{NL}(z,t) \,/\, \partial t^2$ is:

$$\begin{aligned}\frac{\partial P^{NL}(z,t)}{\partial t^2} \;=\; &-\,\varepsilon_0\, d_{eff}\, \omega_1^2\, A_2^*(z)\cdot A_3(z)\cdot e^{i[\omega_1 t-(k_3-k_2)z]} \\ &-\,\varepsilon_0\, d_{eff}\, \omega_2^2\, A_1^*(z)\cdot A_3(z)\cdot e^{i[\omega_2 t-(k_3-k_1)z]} \\ &-\,\varepsilon_0\, d_{eff}\, \omega_3^2\, A_1(z)\cdot A_2(z)\cdot e^{i[\omega_3 t-(k_1+k_2)z]} \;+\; c.c.\end{aligned} \tag{2.15}$$

Assuming the slowly varying envelope approximation $|\partial^2 A/\partial z^2| \ll |2k\partial A/\partial z|$, and substituting the Eq. 2.15 into Eq. 2.11, the following coupled wave equation can be derived:

$$\begin{aligned}\frac{\partial A_1}{\partial z} &= -i\sigma_1 A_2^*\, A_3\cdot e^{-i\Delta k z} \\ \frac{\partial A_2}{\partial z} &= -i\sigma_2 A_1^*\, A_3\cdot e^{-i\Delta k z} \\ \frac{\partial A_3}{\partial z} &= -i\sigma_3 A_1\, A_2\cdot e^{i\Delta k z}\end{aligned} \tag{2.16}$$

where $\sigma_j = d_{eff}\omega_j / c_0 n_j$, $n_j = \sqrt{\varepsilon_{rj}}$ is the refractive index, and $\Delta k = k_3 - k_2 - k_1$ is the wavevector mismatch. As the first two equations are in the same form, it means ω_1 and ω_2 fields play the same role in the interaction.

With the boundary condition that the initial field $A_3(0) = 0$, Eq. 2.16 describes a process that two fields $A_1(0)$ at ω_1 and $A_2(0)$ at ω_2 interact and generate a new field $A_3(0)$ at $\omega_3 = \omega_1 + \omega_2$, known as sum-frequency generation (SFG). In special case when $\omega_1 = \omega_2$, it describes the second-harmonic generation (SHG) process.

With the boundary condition that the initial field $A_2(0) = 0$, Eq. 2.16 describes a process that two fields $A_3(0)$ at ω_3 and $A_1(0)$ at ω_1 interact and generate a new field $A_2(0)$ at $\omega_2 = \omega_3 - \omega_1$, known as DFG or optical parametric amplification (OPA). DFG and OPA are similar processes, they both involve two input fields and generate a new field at their difference frequency. However, DFG usually involves the input fields ω_3 and ω_1 with comparable intensities, while OPA involves an intense pump field at ω_3 and a weak seed field at ω_1. At a special case when $\omega_3 \approx \omega_1$, the process called optical rectification occurs, which can be used to generate THz radiation.

2.2.2 Third-order nonlinear processes

When consider only the third order nonlinear optical effects, the nonlinear polarization reduces to

$$P^{NL}(z,t) \;=\; P^{(3)}(z,t) \;=\; \varepsilon_0\, \chi^{(3)}\, E^3(z,t) \tag{2.17}$$

Third-order nonlinearity is present in materials regardless of their spatial symmetry. In centrosymmetric media where second order nonlinear processes do not occur, third order is the lowest order of nonlinearity. Third-order nonlinear processes include a large variety of four-wave-mixing processes. The simplest process is third-harmonic generation (THG), where three fields at frequency of ω interact to create a new field at frequency of 3ω. Other processes such as self-focusing and self-phase modulation can be explained by the intensity dependent refractive index associated with the third-order nonlinear susceptibility $\chi^{(3)}$.

Third order (cubic) nonlinear susceptibility $\chi^{(3)}$ leads to an intensity-dependent refractive index $n = n_0 + n_2 I$, where I is the pulse intensity, n_0 is the linear refractive index and n_2 is the nonlinear refractive index related to the $\chi^{(3)}$ of the material. n_2 is positive in the transparency range of dielectric media. As a result, self-phase modulation (SPM) and self-focusing Kerr-effect occurs.

Self-phase modulation: In SPM, the temporal phase of the pulse receives the same profile via a nonlinear phase shift related to nonlinear refractive index of the material

$$\phi_{nl}(t) = -\frac{\omega_0}{c} n_2 I(t) L \tag{2.18}$$

where ω_0 is the carrier frequency and L is the propagation distance. This produces a frequency change $\delta\omega(t) = \frac{d}{dt}\phi_{nl}(t)$ that results in the time-varying instantaneous frequency

$$\omega(t) = \omega_0 + \delta\omega(t) \tag{2.19}$$

This contributes to spectral broadening by inducing a negative shift of the instantaneous frequency at the pulse front and a positive shift at the pulse tail (Fig.2.2). The spectrum will be modified and can be strongly broadened than that of the incident pulse.

SPM and four-wave mixing (FWM) are the dominant nonlinear interactions behind the spectral broadening of intense few-cycle pulses in waveguides, filaments and bulk material.

Self-focusing and supercontinuum generation: With the presence of intensity dependent refractive index $n = n_0 + n_2 I$ and a positive n_2 in the transparency range of dielectric media, the spatial distribution of the beam intensity leads to a higher refractive index at the center of the beam comparing to its edges. As a result, the material acts like a lens and enforces the beam to self-focus. Known as self-focusing or Kerr-lens, it is the basis of KLM and supercontinuum (SC) generation via filamentation.

The threshold for self-focusing defined as the critical power P_{cr}, can be expressed for a cylindrically symmetric Gaussian beam as [58]:

$$P_{cr} = \frac{3.72\,\lambda^2}{8\,\pi\,n_0\,n_2} \tag{2.20}$$

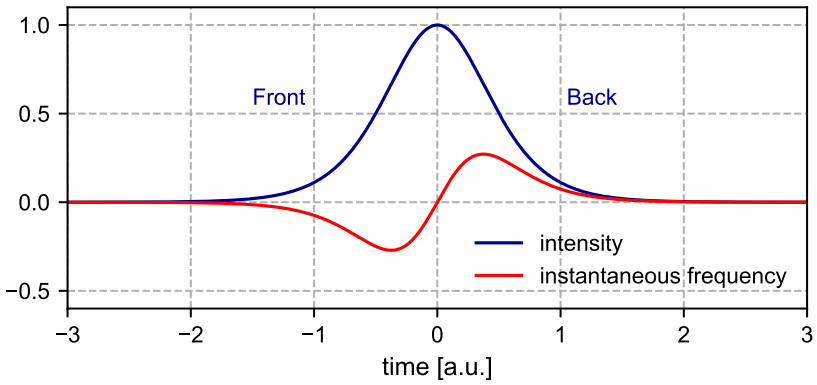

Figure 2.2: Self-phase modulation induces a negative shift of the instantaneous frequency at the pulse front and a positive shift at the pulse tail.

where λ is the laser wavelength. Critical power P_{cr} represent the power for balancing the effect of self-focusing and diffractive spreading of the beam. For power level exceeds P_{cr}, collimated input Gaussian beam will self-focus at a nonlinear focus after distance

$$z_{sf} = \frac{0.367\, z_R}{\sqrt{[(P/P_{cr})^{1/2} - 0.852]^2 - 0.0219}} \tag{2.21}$$

where $z_R = \pi\, n_0\, w_0^2 / \lambda$ is the Rayleigh length for the input Gaussian beam with a radius of w_0. This effect could cause severe damage to the optical components, while under careful control it could lead to filamentation and a dramatic spectral broadening.

Filaments, which can propagate much longer distance than the usual diffraction length while retaining a small beam size without any guiding mechanism, originates from the interplay and coupling between self-focusing, SPM, dispersion, self-steepening, ionisation and plasma generation. The interplay of the processes results in the generation of an ultra-broadband, spatially and temporally coherent SC emission [58]. Due to the material dispersion, the generated SC radiation obtains a regular chirp and therefore exhibits good compressibility. SC radiation produced by a single filament maintains the polarization state and preserve the CEP of the pump pulses. The generated ultra-broadband SC pulses can be directly applied to experiments or serve as a seed pulse for OPAs.

Cross-polarized wave generation cross-polarized wave (XPW) is a third order nonlinear phenomenon, where part of the incident wave along one polarization is converted to a cross-polarized wave at the same frequency [59, 60]. It is a degenerate four-wave mixing process that occurs in cubic crystals with $\chi^{(3)}$ anisotropy. Therefore, phase matching is automatically fulfilled. Besides, the CEP is preserved during XPW process [61]. Using the

slowly evolving envelope approximation, the following coupled wave equations for XPW can be derived [62]:

$$-i\frac{dA_1}{dz} = \gamma_1 A_1 A_1^* A_1 + \gamma_2 A_1 A_1 A_2^* + 2\gamma_2 A_1 A_1^* A_2 + 2\gamma_3 A_1 A_2^* A_2 + \gamma_3 A_2 A_2 A_1^* + \gamma_4 A_2 A_2^* A_2,$$

$$-i\frac{dA_2}{dz} = \gamma_5 A_2 A_2^* A_2 + \gamma_4 A_2 A_2 A_1^* + 2\gamma_4 A_1 A_2 A_2^* + 2\gamma_3 A_1 A_2 A_1^* + \gamma_3 A_1 A_1 A_2^* + \gamma_2 A_1 A_1^* A_1,$$

where A_1 and A_2 are the complex amplitudes of the input and XPW signal, respectively. ξ is the propagation direction. Coefficients γ_i depend on the crystal orientation and the components of $\chi^{(3)}$, can be referred to different third-order nonlinear processes. γ_1 and γ_5 describe SPM; γ_3 cross-phase modulation (XPM); γ_2 and γ_4 describe XPW.

As a third-order process, the temporal and spatial contrast of XPW signal become enhanced due to the proportion relation between the envelope of the generated XPW pulse and the third order of the input pulse envelope [63]. The pedestal and side pulses with lower intensities are therefore suppressed. Moreover, the generated XPW pulse has a shortened pulse duration by $1/\sqrt{3}$ in unsaturated regime, which corresponds to a spectral broadening by a factor of $\sqrt{3}$. Despite its low conversion efficiency, XPW eliminates the need for additional compression stage. Therefore, it provides a simple approach for pulse-shortening, and can be applied in cases where its low conversion efficiency could be tolerated.

2.3 Ultrashort pulse generation

2.3.1 Mode-locked lasers

The invention of laser started a decades long research in generating powerful laser pulses with ever shorter duration [3]. Since the laser gain media usually have excited-state lifetime τ longer than microseconds, additional control in releasing stored energy is needed to generate pulses in shorter time scale. Generating femtosecond ultrashort pulses from lasers requires mode-locking techniques.

The longitudinal modes of a laser resonator are equally spaced by the repetition frequency f_{rep}, which are emitted within the gain-bandwidth of the laser gain medium (Fig. 2.3a). Without control, these modes can be in phase or out of phase at any given time. Summation of the possible resonator modes results in interference in the time domain (Fig. 2.3b). When there is a fixed phase relation between these modes, which correspond to sinusoidal electric fields of different frequencies, single pulses usually significantly shorter than the round-trip time $T = f_{rep}$ can be formed in the time domain. The pulse width is inversely

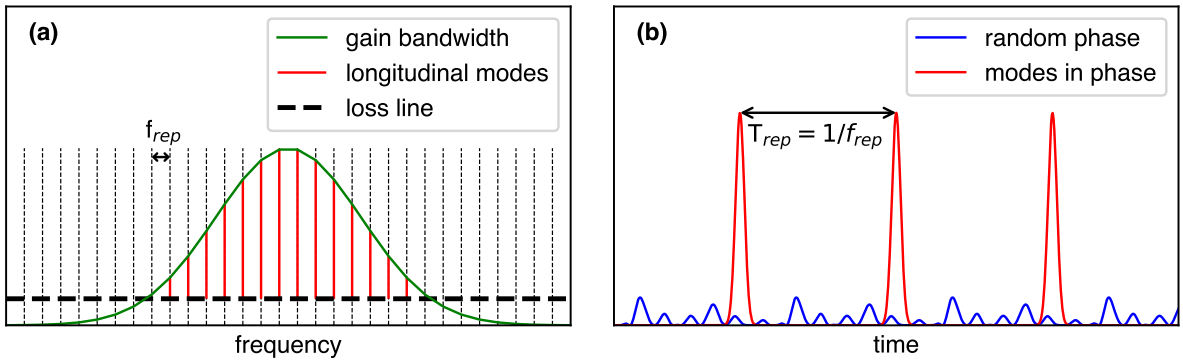

Figure 2.3: Laser mode locking in the frequency and time domain. (a) In the frequency domain, the equally spaced longitudinal modes of a laser resonator that are under the gain bandwidth can be emitted. (b) In the time domain, these longitudinal modes with a locked phase lead to the formation of short pulses, otherwise with random phase only generates noise.

proportional to the number of coupled modes inside the laser oscillator. That means for a given mode spacing, the broader the gain bandwidth, the more modes are coupled, and the shorter the pulse. In case when the modes have random phases, no constructively interference happens in time, the emitted light is weak and random at all times. So the simultaneous oscillation of a large number of phase-locked longitudinal modes in a laser yields an ultrashort pulse, which concentrates the entire energy of the radiation field.

To lock the phase between longitudinal modes, optical loss modulator using the acousto-optic or electro-optic effect can be applied, which is known as active mode-locking. However, the introduced loss modulation is usually slow and far from femtosecond regime. Passive mode-locking using saturable absorber is another way to obtain self-amplitude modulation (SAM) inside the laser cavity, and can obtain much shorter pulses due to the fast loss modulation of saturable absorber compared to electronically driven loss modulation. The discovery of self-mode-locking in a Ti:Sa laser in 1991 [9], which was later known as the result of KLM, has led to remarkable progress in femtosecond pulses genertion with solid-state lasers. The shortest pulses from laser oscillator in the few optical cycle regime can be generated, using KLM together with a broadband gain media Ti:Sa. Nowadays, femtosecond pulse has been generated based on KLM in a wide range of other solid-state lasers as well, and further passive mode locking technique based on semiconductor saturable absorber mirror (SESAM) were also developed [64, 65].

The shortest pulses from a KLM Yb:YAG thin-disk oscillator can be 140 fs [26], reaching the limitation imposed by the emission bandwidth of the gain media. In experiments where few-cycle pulses are needed, additional post compression has been demonstrated to reach

down to sub-10 fs [29, 66].

2.3.2 Chirped pulse amplifiers

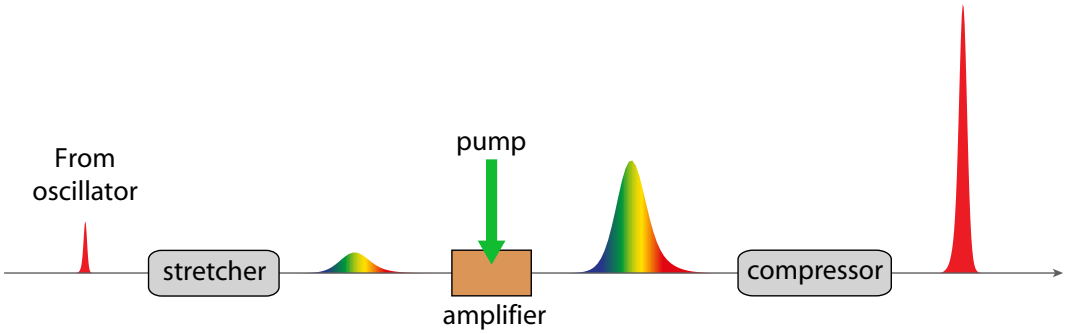

Figure 2.4: Concept of chirped pulse amplification.

Ultrashort pulses provide high optical fields that drive many important processes in physics. However, for many applications, the peak power delivered by mode-locked laser oscillators in the range of megawatt is not sufficient. Further increase of the pulse energy is therefore necessary with the help of amplifier systems, typically in the configuration of multi-pass amplifier or regenerative amplifier. To avoid limitations imposed by high average power, pockels cell based pulse picker can be used to reduce the repetition rate of seed pulses. As pulse energy increases during amplification, the high peak power of short pulses causes severe damage to the laser gain medium or amplifier optics. The demonstration of CPA concept in laser amplification by Strickland and Mourou in 1985 [13] brought a solution to this problem. As illustrated in Fig. 2.4, in CPA the seed pulses are temporally stretched by adding positive dispersion, and recompressed after amplification by introducing negative dispersion. The positive dispersion for stretching is usually given by a highly dispersive setup such as a long optical fiber or a grating stretcher [67, 68], with a typical stretching factor of hundreds to thousands of times. Therefore, the intensity inside the amplifier is reduced by orders of magnitude, which allows for a safe operation of the amplifier. CPA revolutionized high energy ultrafast laser development and was awarded the 2018 Nobel prize in physics. Nowadays, CPA-based Yb:YAG thin-disk regenerative amplifiers at 5-kHz repetition rate are capable of delivering over 1 kW average power with pulse energies up to 200 mJ and a pulse durations below 1 ps [20].

2.3.3 Spectral broadening

The main limitation of ultrafast Yb:YAG thin-disk lasers originated from its relatively narrow gain bandwidth. As a result, the shortest pulses fully employing the gain bandwidth from Yb:YAG thin-disk oscillator is 140 fs. The amplified pulses typically has a duration of few hundreds of femtoseconds to a few picoseconds due to gain narrowing. Therefore, external pulse compression is needed for many experiments to have a larger frequency coverage and reach few-cycle regime.

Spectral broadening of Yb:YAG thin-disk lasers is usually achieved with SPM in bulk materials [36, 39, 69], microstructured optical fiber [29, 66], gas-filled hollow waveguide [70] or gas filaments, or with supercontinuum generation in bulk materials [58]. In special cases, XPW generation can be used for self-compressed spectral broadening [60]. These broadened spectra are centered around the emission wavelength of the driving laser. Bandwidth extension beyond this limit requires nonlinear conversion, which will be discussed in the next section.

2.4 Optical parametric amplifier

As many experiments in time-resolved spectroscopy and high-field physics require femtosecond pulses with broadly tunable frequency, the use of Yb:YAG lasers are therefore restricted due to its fixed central wavelength at 1030 nm. For example in HHG process, driving pulse with longer wavelength is preferred to achieve better phase-matching and extend the cutoff energy [24]. And in MIR FRS, molecular vibrational excitation with few-cycle waveform-stable MIR pulses is a key point to reach an enhanced sensitivity and dynamic range [25]. Second order nonlinear optical effect known as OPA can be employed to cover a broad spectral range from visible to MIR.

OPA occurs in a suitable nonlinear crystal (non-centrosymmetric structure) with non-zero second order nonlinearity $\chi^{(2)}$, in the presence of a high energy, high frequency pump pulse (at frequency ω_3) and a lower energy, lower frequency seed pulse (at frequency ω_1). In this process, energy is transferred from the pump pulse towards the seed pulse, while at the same time an additional pulse named idler pulse (at frequency ω_2) is generated, which fulfills the energy conservation:

$$\hbar\omega_1 + \hbar\omega_2 = \hbar\omega_3 \tag{2.22}$$

Momentum has to be conserved as well for efficient energy transfer, so that all interacting pulses maintain a fixed phase relation during amplification:

$$k_1 + k_2 = k_3 \tag{2.23}$$

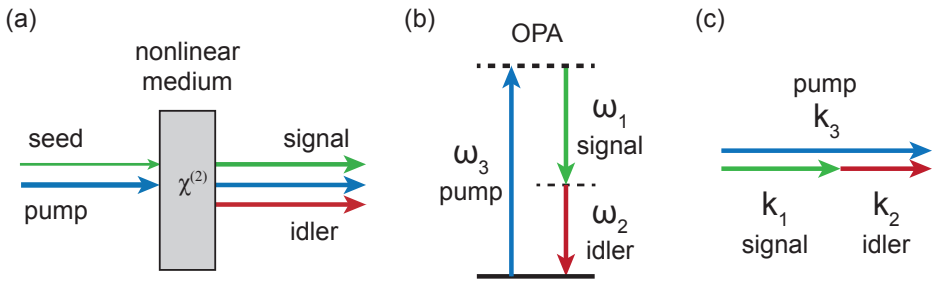

Figure 2.5: (a) Scheme of the OPA process. Spatial and temporal overlap pump and seed pulses in a nonlinear medium results in the amplification of signal pulse and a newly generated idler pulse due to the energy conservation. (b) The photon picture of the OPA process. The energetic pump photon excites the nonlinear medium to a virtual state, with the presence of the seed photon, the signal transition is stimulated and therefore amplify the seed energy, while at the same time an idler photon which fulfills the energy conservation is generated. (c) The momentum conservation needs to be fulfilled for an efficient energy transfer.

where k_i is wave vector.

This nonlinear process can be understood via photon picture of light with virtual energy levels inside the nonlinear crystal (Fig. 2.5(b)). The energetic pump photon brings the nonlinear medium to a virtual level, from where it falls back to the ground level via coherent emission. With the presence of the seed photon, this process is stimulated and the seed energy is amplified, while at the same time an idler photon is generated to fulfill the energy conservation. Different from laser gain medium, due to the absence of a real energy level, there is no energy storage in the nonlinear medium. After excitation to the virtual level by the pump photon, population fall back to the ground level nearly instantaneously [71]. This requires all interacting waves to be overlapped both in time and space.

Considering the coupled equations describing OPA (in Eq. 2.16), and assuming that the pump field is not depleted during the interaction, so that $A_3(0) \approx constant$, the intensities of signal and idler after an interaction length L are:

$$\begin{aligned} I_1(L) &= I_{10}\left\{1 + \left[\frac{\Gamma}{g} sinh(gL)\right]^2\right\} \\ I_2(L) &= I_{10}\frac{\omega_2}{\omega_1}\left[\frac{\Gamma}{g} sinh(gL)\right]^2 \end{aligned} \tag{2.24}$$

where the nonlinear coefficient $\Gamma^2 = \frac{2\, d_{eff}^2\, \omega_1\, \omega_2}{\varepsilon_0\, c_0^3\, n_1\, n_2\, n_3} I_3$ and the small signal gain $g = \sqrt{\Gamma^2 - \left(\frac{\Delta k}{2}\right)^2}$.

The parametric gain $G(L)$ of an OPA is therefore:

$$G(L) = \frac{I_1(L)}{I_{10}} = [\,1 + \frac{\Gamma^2}{g^2}\, sinh^2(gL)\,] \tag{2.25}$$

Under the large-gain approximation ($gL \gg 1$), the parametric gain $G(L)$ could be simplied to

$$G(L) \simeq \frac{\Gamma^2}{g^2}\frac{e^{2gL}}{4} \tag{2.26}$$

It is clear to see that the gain strongly depends on small signal gain g and reaches its maximum value at perfect phase-matching condition with $\Delta k = k_3 - k_2 - k_1 = 0$. This can be understood in the wave picture that the newly generated frequencies from different position of the nonlinear medium has to have a same phase, such that a constructive interference could happen and build up the output. It means the forcing term $\partial^2 P^{NL}(z,t)\,/\,\partial t^2$ should propagate at the same speed as the phase velocity of the newly generated beam. In the OPA process, known from the Eq. 2.15, the forcing term propagates as $e^{i[\omega_2 t-(k_3-k_1)z]}$, and the idler frequency ω_2 propagates as $e^{i(\omega_2 t-k_2 z)}$. To match the corresponding phase velocity means $(k_3-k_1)/\omega_2 = k_2/\omega_2$, which occurs when Eq. 2.23 is fulfilled. That is the phase-matching condition.

Although broadband OPAs only offer low conversion efficiency in the order of 10-30%, they are favored for short pulse generation for the advantages in: (i) broadband amplification with different available crystals in various central frequencies from ultraviolet (UV) to MIR [72–76], (ii) the preservation of CEP during the amplification process, (iii) scalability in energy and average power, and (iv) relative simplicity.

When OPA is combined with CPA, the so-called OPCPA offers higher achievable output energy. With the use of energetic pump lasers in sub-picosecond to nanoseconds durations, the stretching and recompression of the seed pulses ensures a good temporal match, therefore an efficient extraction of pump energy during the amplification [77, 78].

Difference frequency generation As mentioned before, DFG process is the same as OPA. However, in DFG the main interest is in the newly generated idler pulse at frequency $\omega_2 = \omega_3 - \omega_1$. This process is particularly interesting due to its ability in generating MIR pulse with passively stabilized CEP.

By mixing the pulses from a Yb:YAG thin-disk laser at 1030 nm (ω_1=291 THz) and the 680 nm (ω_3=441 THz) spectral components of their SC generation in bulk, one could generate the idler pulses at 2000 nm (ω_2=441-291=150 THz). Since ultrashort pulses contain a broad spectrum, DFG could also occur between frequencies contained within the spectrum of one single pulse, namely IPDFG.

DFG process can also be employed to generate CEP-stable pulses. Deriving from the coupled equations Eq. 2.16, the CEP of the involved pulses in DFG process ($\omega_{DFG} = \omega_2 = \omega_3 - \omega_1$) are related as [79]

$$\varphi_{DFG} = \varphi_2 = \varphi_3 - \varphi_1 - \pi / 2 \tag{2.27}$$

Here the CEP of the idler pulse is related to the signal and the pump pulses. If signal and pump pulse were from the same laser source, then both possess same CEP fluctuations φ, with a difference of a constant phase c accumulated due to propagation. Then $\varphi_3 = \varphi$, $\varphi_1 = \varphi + c$, and consequently $\varphi_{DFG} = \varphi_3 - \varphi_1 - \pi / 2 = constant$. In such a way, the fluctuations of φ are cancelled out, and the generated DFG is CEP stablized. As an all-optical technique, such passive CEP stablization is a simple approach to generate CEP-stable pulses.

2.4.1 Phase-matching

Since phase matching is not achievable in isotropic media with positive dispersion due to the required different refractive indices for interacting waves, birefringence phase-matching or quasi-phase-matching can be used to fulfill the phase-matching condition [45, 80].

In the first approach, the birefringence of the nonlinear crystal with different polarization states of the input beams are employed, such that the ordinary refractive index n_o of one beam matches the other one with extraordinary index $n_e(\theta)$ (Fig. 2.6(a)). θ is the so-called phase-matching angle, it represents the angle between propagation direction and the optical axis.

While in quasi-phase-matching (Fig. 2.6(b)), a periodic modulation to the sign of the nonlinear coefficient is applied, leading to an average macroscopic net exchange of energy between the fields [81]. The modulation of the nonlinear coefficient is achieved by applying a suitable voltage to the crystal periodically along the beam propagation direction. After each coherence length L_c where the phase mismatch is accumulated to π, the alignment of the ferroelectric domains in the crystal is reversed, so that the electric field of the new frequency could continue to build up. As a result of such modulation with a period of $\Lambda = 2L_c$, a corresponding grating wave-vector $K_g = 2\pi/\Lambda$ is introduced and included in the phase matching equation $\Delta k = k_3 - k_2 - k_1 - K_g = 0$. Therefore for Quasi-phase-matching (QPM), the main parameter in fulfilling the phase-matching condition is the poling period Λ of the crystal.

For broadband phase-matching, the group velocity of signal and idler has to be matched. In collinear geometry, this is typically achieved with Type-I phase-matching at degeneracy point, where signal and idler have the same frequency and polarisation. Such scheme

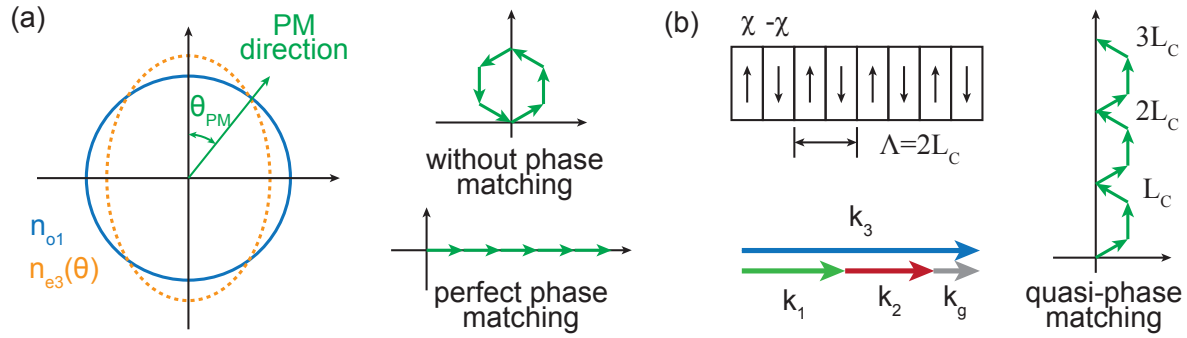

Figure 2.6: (a) Birefringence phase-matching in a negative uniaxial crystal. θ_{PM} is the phase-matching angle, where $n_{o1} = n_{e3}(\theta)$. The figures on the right side show the complex domain, and the green arrows illustrate the phasors corresponding to the complex amplitude contributions of the newly generated signal waves at different length of the nonlinear crystal. Without phase matching, the energy transfer direction changes periodically, which depends on the periodically changing phase relation between the interacting waves. With perfect phase matching, these contributions build up constructively. (b) In quasi-phase-matching, the sign of the nonlinear coefficient is periodic modulated with a period of $\Lambda = 2L_c$. A corresponding grating wave-vector $K_g = 2\pi/\Lambda$ is induced in the phase matching equation $\Delta k = k_3 - k_2 - k_1 - K_g = 0$. The figure on the right side show the complex domain, as the sign of the nonlinear coefficient is flipped after every coherence length, the complex amplitude contributions continue to build up at a lower conversion efficiency compare to the perfectly phase matched case.

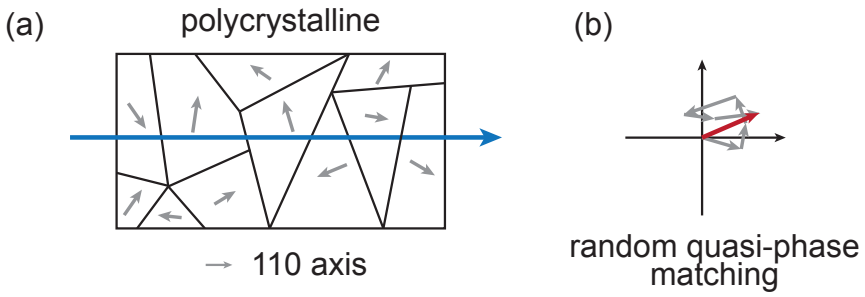

Figure 2.7: (a) In RQPM, the random distribution of the grain axis in polycrystalline material along the beam path (blue arrow) results in phase randomization and a non-zero nonlinear susceptibility. (b) In the complex domain, due to the random size and orientation of each grain, the complex amplitude contributions have random amplitude and phase. The accumulated complex amplitude contributions after several grains will not average to zero.

is called degenerate optical parametric amplification (DOPA) [72]. In the non-collinear optical parametric amplification (NOPA) scheme [82] an angle between signal and idler pulse is introduced, which leads to temporal overlap between signal and idler pulse. Further broadband phase-matching scheme e.g. frequiency domain optical parametric amplification (FOPA) [83] was developed to distribute the requirement of phase-matching into several different crystals.

With the above mentioned methods, phase matching can be achieved in single-crystalline materials. However, it is also possible to generate second-order nonlinear processes in polycrystalline material, based on so-called RQPM [84]. The random distribution of the grain axis in polycrystalline material along the beam path results in phase randomization and a non-zero nonlinear susceptibility (Fig. 2.7), which leads to a generated nonlinear signal much higher than the contribution of a single coherence length. This process does not require a specific crystal orientation or input beam polarization, and can be applied for broadband MIR generation via DFG process [85].

2.5 Light field synthesis

Either with mode-locked laser oscillators, external spectral broadening techniques, or broadband OPAs, few-optical-cycle pulses can be routinely generated. Dictated by the Fourier theorem, short light pulse requires a broad spectral bandwidth and a flat spectral phase. However, further reducing the pulse duration approaching sub-optical-cycle regime faces limitation imposed by emission bandwidth in lasers or dispersion control and/or phase-matching bandwidth in OPA. To overcome these limitations, coherent combination

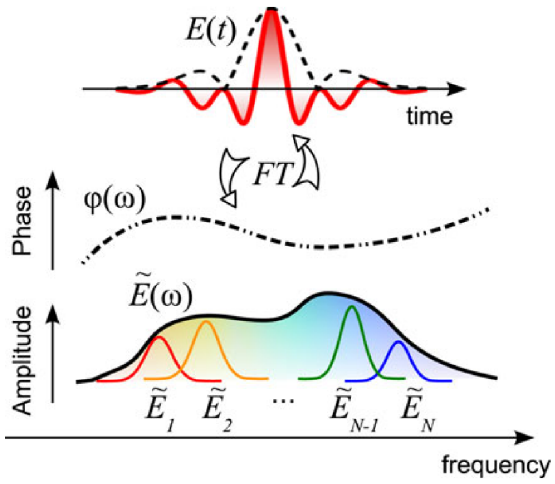

Figure 2.8: The electric field of a light transient $E(t)$ and its spectrum $\tilde{E}(\omega)$ in the frequency domain are associated by Fourier transform (FT). The spectrum $\tilde{E}(\omega)$ can be seen as the superposition of narrow sub-bands $\tilde{E}_j(\omega)$. Adapted with permission from [79].

or synthesis of separately generated ultrashort pulses at different central frequencies is a promising technique.

As shown by Manzoni et al. in [79], coherent superposition of longer pulses at different spectral sub-bands leads to pulse synthesis (Fig. 2.8). The electric field of a light transient $E(t)$ described by Eq. 2.1 is associated with the complex spectrum $\tilde{E}(\omega)$ in the frequency domain:

$$E(t) = \int_{-\infty}^{\infty} \tilde{E}(\omega) e^{i\omega t} d\omega = \int_{-\infty}^{\infty} |\tilde{E}(\omega)| e^{i\varphi(\omega)} \cdot e^{i\omega t} d\omega \tag{2.28}$$

And the spectrum $\tilde{E}(\omega)$ can be decomposed into sub-bands $\tilde{E}_j(\omega)$:

$$\begin{aligned} \tilde{E}(\omega) &= \tilde{E}_1(\omega) + \tilde{E}_2(\omega) + \cdots + \tilde{E}_N(\omega) \\ &= |\tilde{E}_1(\omega)| e^{i\varphi_1(\omega)} + |\tilde{E}_2(\omega)| e^{i\varphi_2(\omega)} + \cdots + |\tilde{E}_N(\omega)| e^{i\varphi_N(\omega)} \end{aligned} \tag{2.29}$$

Which relates to the time domain relation due to the linearity of the Fourier transform operator:

$$E(t) = E_1(t) + E_2(t) + \cdots + E_N(t) \tag{2.30}$$

where each transient $E_j(N)$ corresponds to spectral sub-band $\tilde{E}_j(\omega)$ may be significantly longer than the overall synthesized field $E(t)$.

In 1990, T. W. Hänsch proposed the idea about superposition of six harmonics created

by two continuous wave (CW)-lasers [86], where by controlling the relative phases among the six harmonics, sub-femtosecond pulses could be generated. Following this idea, a few years ago, based on molecular modulation [87] and manipulating the relative phase and amplitude of five discrete harmonics, it is shown that optical fields with a shape of square, sawtooth, and sub-cycle sine and cosine pulses can be produced in a controlled way [88]. Other efforts have been made to synthesis different spectral components from two synchronized oscillators [89], or two erbium-doped fiber amplifiers seeded by a common mode-locked erbium-doped fiber oscillator [90]. However, these sources were not CEP-stabled. For generating controlled waveform further CEP control would be needed but challenging to implement. Ti:Sa oscillators can be CEP stabilized. Using a double-LCD prism-based pulse shaper allows the control of spectral phase and amplitude, results in output pulses with a controlled waveform [91]. Nevertheless, the bandwidth is limited by the frontend, and the highest energy and average power is limited by the pulse shaper.

In 2011, the energy and bandwidth of light transient was scaled by using a CEP-stable Ti:Sa amplifier and its subsequent spectral broadening in a gas-filled HCF [17]. Such frontend typically provides hundreds of micro-joule, octave spanning spectrum. By splitting and recombining the broad spectrum into three or four spectral channels with dichroic mirrors, each channel was individually compressed to its Fourier limit by chirped mirrors. Controlling relative timing and phase among different spectral channels allowed the generation of sub-cycle light transients. The waveform characterization of the sub-cycle transients was performed by attosecond streaking. However the maximum output energy of such synthesizer is limited to a few hundreds of micro-joule, restricted by the driving laser source.

To further scale the average and peak-power of light transients, coherent combination of pulses from multiple broadband OPCPA is a promising strategy [21, 92, 93], which is discussed and investigated in the next chapter.

Chapter 3

High-Energy, Multi-Octave Source

Ever shorter pulses are generated since the invention of laser, by means of temporal shaping and precise control of the dispersion of the light in sub-cycle regime. The shape of the electric field of a pulse in time domain is determined by (i) spectral bandwidth following Fourier theory, (ii) relative spectral intensity of different spectral components, and (iii) the spectral phase. Ultrashort pulse shaping from picosecond (ps) down to sub-ten femtosecond (fs) has been demonstrated by employing various tools including: prisms, gratings, dispersive mirrors [67, 94, 95], spatial light modulators [96, 97] and acousto-optic programmable dispersive filters [98]. These tools allow for controlling the spectral phase of a pulse, and also the amplitude in the latter two cases. Such flexibility enables generating desired ultrashort pulses. However, all the mentioned approaches are limited in terms of either the spectral bandwidth or the pulse energy, or both.

These limitations were overcome in 2011 [17]. By coherent electric field synthesis, a μJ-level, super-octave spectrum generated from a gas-filled HCF was compressed to its Fourier limit [99]. The bandwidth limitation imposed by chirped mirrors were overcome by splitting a broadband spectrum into several spectral regions, and compressing each spectral region to its Fourier transform limit. By coherent superposition of all channels interferometrically, light transients were produced. One can shape the light transients by controlling the relative temporal delay and the relative spectral intensity of each channel. Therefore, such an interferometer requires CEP-stable input pulses. Nowadays in laboratories, μJ-level light transients at sub-ten kilohertz (kHz) repetition rates are routinely generated, providing unparalleled flexibility for steering light-matter interactions, as well as on triggering and probing electron dynamics with sub-fs precision [100, 101]. Nevertheless, peak- and average-power are limited in this approach. To overcome this limitation and to further scale the average and peak-power of light transients, coherent combination of pulses from multiple broadband OPCPA is proposed [21, 92, 93]. This method requires peak- and average-power scalable pump lasers and CEP-stable broadband seed pulses.

In comparison to the available laser media, Yb-doped materials are most capable for

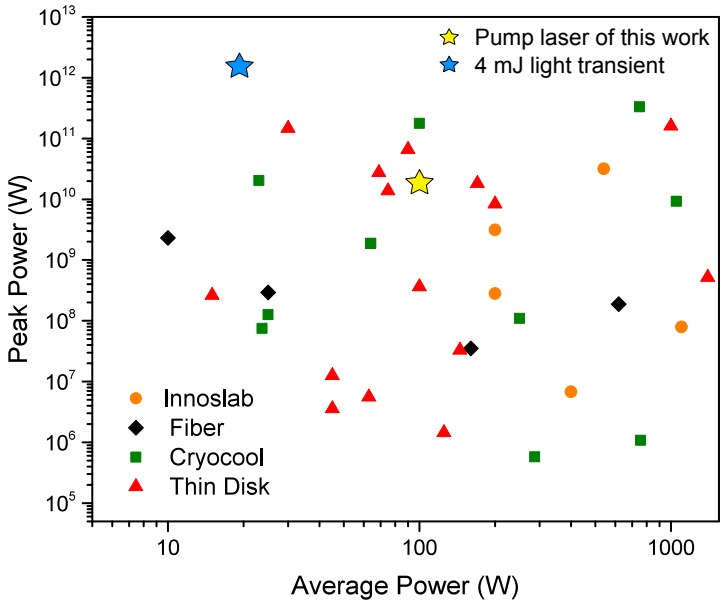

Figure 3.1: Summary of the recorded performances of Yb-doped lasers in four different geometries in terms of average and peak powers. The orange dots show the performance of Yb:YAG Innoslab lasers corresponding to Refs [104, 106, 108–110]. The purple dots demonstrate Yb:YAG fiber lasers corresponding to [111–114]. The green dots represent the Yb:YAG cryo-cooled sources [103, 107, 115–123]. The performance of the Yb:YAG thin-disk lasers are demonstrated by red dots [20, 70, 124–137]. The yellow star indicates the pump laser in thin-disk geometry used in this chapter. And the simulated 4 mJ light transient from the prototype OPCPA-based parallel field synthesizer pumped by this laser is shown by the blue star. Adapted from [22] © [2019] IEEE.

simultaneous scaling of the peak- and average-power with pulse duration in the range of sub-picosecond to a few picoseconds [21, 102–107]. Therefore, they are excellent pump sources for OPCPA. Within a wide range of different Yb-doped gain media, Yb:YAG is particularly suitable for high-power operation with emission at 1030 nm. Yb:YAG has a low quantum defect, which reduces thermal effects. Its absorption band with peaks around 940 nm and 969 nm allows direct pumping by cost-effective diode lasers. Together with a good thermal conductivity and the absence of excited-state absorption, Yb:YAG shows a superior performance in high-power operation.

Yb:YAG lasers can be implemented in several geometries, such as rod, slab, fiber or thin-disk [18], and are capable of delivering pulses at variety of energies and repetition rates. As can be seen in Fig. 3.1, Yb:YAG thin-disk lasers deliver a wide range of average

powers at a relatively higher peak power compared to other technologies. In the case of thin-disk geometry, the simultaneous energy and average-power scaling is due to the efficient heat removal from the gain medium. The gain medium is cooled by a water-cooled heat sink, which is attached to the back of the thin-disk. This geometry makes the heat to flow efficiently in one-dimension along the laser beam prorogation direction. High pump absorption efficiency of 90 % can be achieved, with a multi-pass arrangement of the pump beam, which allows for tens of double-passes via the thin-disk gain medium. Combined with CPA, these enable energy, and average-power scalability, while at the same time maintains an excellent beam quality. Yb:YAG lasers in thin-disk geometry have been demonstrated with an output energy in joule-level [138, 139] or average power in kilowatt-level [20, 103, 140]. However, the narrow-band emission cross-section [19], in addition to the gain narrowing limits their pulse duration to several picoseconds at joule and hundreds of femtoseconds at μJ energy.

These unique properties, in combination with the reliability of industrial diode pumps, makes Yb:YAG lasers potential drivers for high-energy, high-average power light transients. In this chapter two approaches for generating high-energy light transients based on Yb:YAG amplifier are discussed: (I) parallel field synthesis; (II) cross-polarized field synthesis.

3.1 Parallel field synthesis

Concept Scaling the energy of light transients to multi-milijoules at multi-kilohertz repetition rates requires energy- and power-scalable schemes [21, 93]. These schemes are based on broadband OPCPAs at different spectral ranges and their subsequent coherent combination. OPCPA offers up to one octave amplification bandwidth at tunable central wavelength from visible to mid-infrared and scalable in term of energy and average power. Therefore, coherent combination of few-cycle pulses from two or more OPCPA channels is a promising route to generate light transients at high energy and average power.

Schematic of a parallel waveform synthesizer is shown in Fig. 3.2 [22, 143]. In this scheme, the broadband seed is split into different spectral regions, and feed to parallel OPCPA channels for amplification. The outputs of these OPCPA channels are individually compressed, and their subsequent coherent combination results in light transients. In parallel synthesis of OPCPAs [92, 93, 144], dispersion only needs to be managed within each channel until the combiner. Since the output waveform of the light transient depends on the relative phase, timing, and amplitude of each OPCPA channel, the relative phase and temporal jitter need to be compensated for a stable synthesis.

Based on a similar concept and by using a 20 mJ, 1 kHz, 150 fs Ti:Sa amplifier, light transient with 1 mJ of energy was generated [145, 146]. Nevertheless, simultaneous scale of the peak- and average-power in Ti:Sa amplifier is limited due to thermal effects and

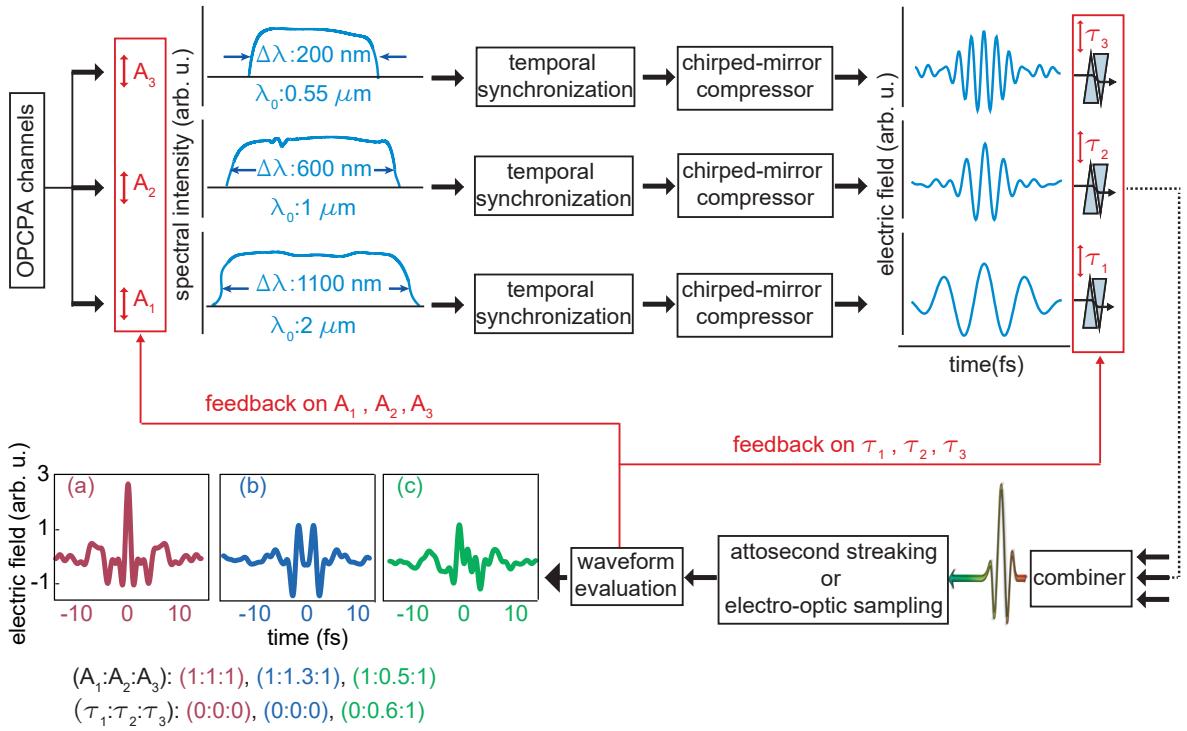

Figure 3.2: Scheme of a proposed waveform synthesizer for shaping the light transient. Three OPCPA channels centred at 550 nm, 1000 nm, and 2000 nm cover an ultra-broadband spectrum spanning from visible to mid-infrared. The temporal overlap among three channels are achieved by the delay line placed after amplification. Afterward, chirped-mirror compressors are used to compress each channel to its Fourier limit individually. The relative delay among different channels can be fine-tuned via a pair of glass wedges placed in each channel. After spatially combining the three channels using two broadband dichroic beam combiners, the resultant light transients can be characterized via attosecond streaking [141] or electro-optic sampling [142]. Various light transients can be generated by manipulating the relative spectral amplitude (A_1, A_2, A_3) and the relative phase (τ_1, τ_2, τ_3) of each channel. As an example, three possible synthesised light transients are given in panels (a), (b), and (c). Adapted with permission from [143].

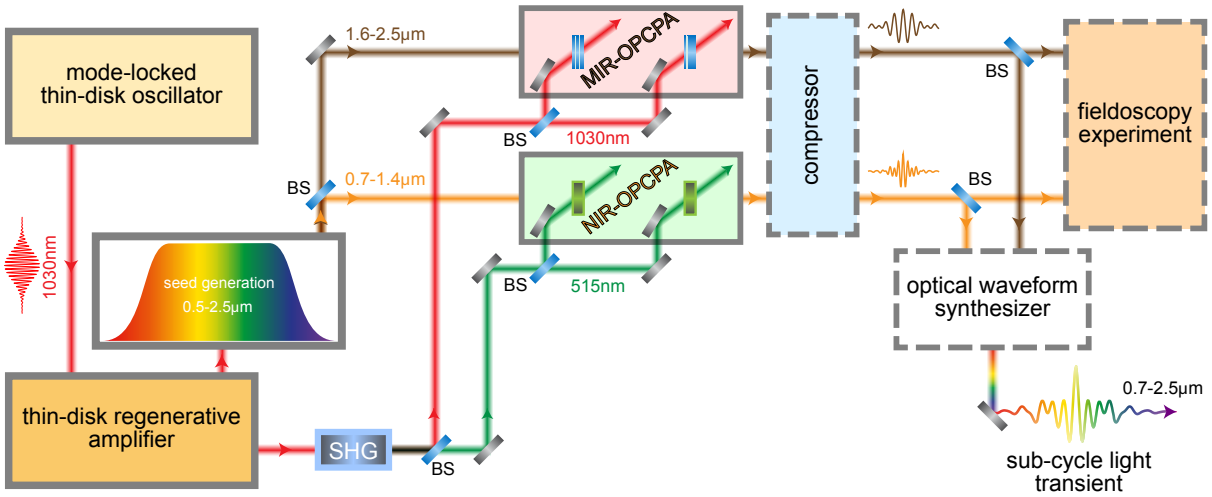

Figure 3.3: Prototype OPCPA-based field synthesizer pumped by Yb:YAG thin-disk laser. The system starts with a Yb:YAG thin-disk regenerative amplifier seeded by a Yb:YAG thin-disk oscillator, it delivers 20 mJ of pulse energy at 5 kHz repetition rate. With a small portion of the amplifer's energy to drive a CEP-stable supercontinuum module, an ultra-broadband CEP-stable supercontinuum seed spanning from visible to mid-infrared is generated. After splitting into two spectral regions centered at 1000 nm and 2000 nm wavelength, they seed OPCPA channels pumped by the fundamental and second harmonic of the amplifer's remaining energy. Afterward, the amplified pulses from OPCPA channels are compressed to their Fourier transform-limit, and coherently combined in an optical waveform synthesizer. BS: beam splitter, SHG: second-harmonic generation.

damage threshold [147]. However, to scale the energy and average power of light transients further, a different frontend is needed [148], which is the subject of this chapter.

The schematic of a prototype OPCPA-based parallel field synthesizer pumped by Yb:YAG thin-disk laser is shown in Fig. 3.3 [22, 143]. The Yb:YAG thin-disk regenerative amplifier serves as the pump laser. A fraction of the amplifier's output is used for generating a CEP-stable supercontinuum. Afterwards, the broadband spectrum is split by a dichroic mirror into two regions and sent to two OPCPA channels pumped by the remaining energy of the amplifier. After dispersion management, the output from both OPCPA channels are compressed to few-cycle pulses, and are characterised for coherent combination.

In the following sections I present the development of the pump laser (section 3.1.1), CEP-stable supercontinuum module (section 3.1.2), OPCPA channels for amplifying different spectral region (section 3.1.3), energy scaling in OPCPA channels (section 3.1.4), temporal characterisation of the synthesizer (section 3.1.5), and its first application for field-resolved NIR molecular spectroscopy (section 3.1.6). The experiments presented were performed by the author jointly with Ayman Alismail.

3.1.1 Yb:YAG thin-disk regenerative amplifier

[1] Figure 3.4 shows the layout of the pump laser. Based on CPA, the low energy seed pulses are temporally stretched, amplified to mJ-level and compressed to their Fourier transform limit (FTL). Previous studies show that the accumulated nonlinear phase in an amplifier can be decreased by increasing the energy of the seed pulses [150]. For this reason, a home-built Yb:YAG thin-disk KLM oscillator was developed to seed the regenerative amplifier.

Nowadays Yb:YAG thin-disk oscillators deliver the highest pulse energy among mode-locked oscillators [131, 151, 152]. SESAM soliton-modelocking or KLM are commonly used for pulse formation, where the nonlinearity and dispersion have to be balanced for each round trip [3, 64]. KLM oscillators deliver shorter pulses and they are robust against optical damages.

The oscillator cavity is shown in Fig. 3.4(a). The oscillator has a 10 m linear cavity with a 13% transmission wedged output-coupler (Layertec GmbH) on one end and a highly reflective plane mirror on the other end. A plane Yb:YAG thin-disk (TRUMPF Scientific Lasers GmbH) with a thickness of around 100 μm provided the gain inside the cavity and was pumped by a fiber-coupled laser diode (Dilas Diodenlaser GmbH, M1F8H12-940.5-500C-IS11.34) at 940 nm wavelength. With three high-dispersive mirrors in the cavity to provide a total GDD of -18000 fs^2, the nonlinearity and dispersion were balanced at each round trip. A 1 mm-thin sapphire plate was placed at the focus of the cavity as the Kerr medium. Together with a copper-made hard aperture and a soft aperture provided by the gain medium, they allowed for Kerr-lens mode-locking. The mode locking was triggered by perturbing a concave mirror mounted on a translation stage.

The oscillator has an output average power of 30 W at a repetition rate of 15 MHz, corresponding to 2 μJ pulse energy. A home-built second-harmonic frequency-resolved optical gating (SH-FROG) employing a 100-μm beta barium borate (BBO) crystal was used to characterize the oscillator's output. Fig. 3.5(a) shows the retrieved temporal profile together with the measured spectrum of oscillator's output. The transverse intensity profile is shown in the inset. Fig. 3.5(b) shows the measured and retrieved SH-FROG spectrograms. The output pulses has a FWHM transform-limited pulse duration of 350 fs. The pulse-to-pulse fluctuation is less than 1 % (root mean square (RMS)), and the beam pointing fluctuations are less than 0.6% (RMS) of the beam size during one-hour measurement. With thermal management of the oscillator's housing and inner components, a near turn-key operation ensures a reproducible day-to-day performance.

The output pulses were sent to a pulse picker (including a 25 mm-thick BBO crystal) to reduce the repetition rate to 5 kHz. The selected 5 kHz pulses were temporally stretched by a grating stretcher consisting of two gold-coated gratings, which provides a GDD of -500 ps/nm. After stretching, the seed pulses contained 1μJ of energy, 2.92 nm spectral

[1] This section is adapted from [149]

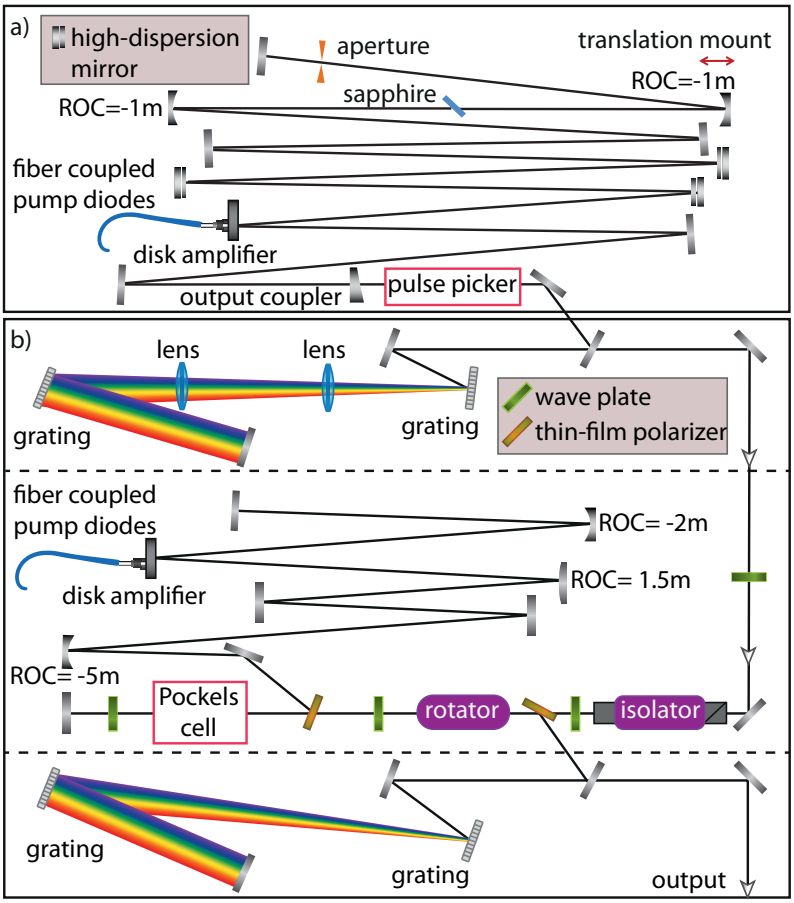

Figure 3.4: Schematic of the Yb:YAG thin-disk regenerative amplifier seeded by a Yb:YAG thin-disk KLM oscillator. (a) The fiber-coupled diode-pumped Yb:YAG thin-disk KLM oscillator delivers 2 μJ, 350 fs pulse at a repetition rate of 15 MHz. The repetition rate is reduced to 5 kHz using a pulse picker to seed the amplifier. (b) The 5 kHz seed pulses are then amplified in a Yb:YAG thin-disk regenerative amplifier with CPA configuration. The seed pulses are temporally stretched before coupling into the amplifier's cavity, which contains a fiber-coupled, diode-pumped, Yb:YAG thin-disk gain medium. The input seed pulses are temporally stretched before entering the regenerative amplifier. The amplifier cavity contains a fiber-coupled, diode-pumped, Yb:YAG thin-disk as gain medium. After coupling out of cavity using a Pockels cell, the amplified pulses are temporally compressed in a grating compressor consisting of two reflective dielectric gratings. ROC: radius of curvature. Adapted with permission from [149] © The Optical Society.

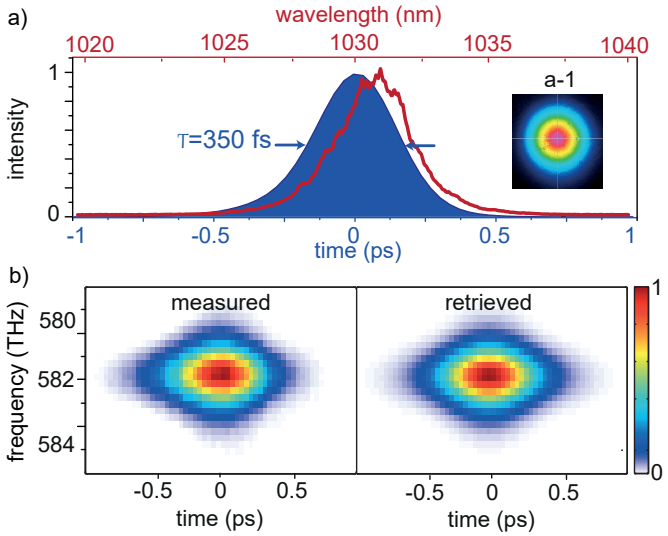

Figure 3.5: (a) The measured output spectrum of the Yb:YAG thin-disk KLM oscillator (red) and the retrieved temporal intensity (blue) from SH-FROG measurement. Inset: beam profile of the oscillator. (b) The measured and retrieved SH-FROG spectrogram of the oscillator (G_{error}: 6.8×10^{-3}). Adapted with permission from [149] © The Optical Society.

bandwidth (FWHM) and a pulse duration of 2 ns. The stretched pulses were then sent to the cavity of the regenerative amplifier for amplification. After passing through a Faraday rotator, which separates incoming and outgoing pulses, a Pockels cell with a 20-mm-thick BBO crystal and a clear aperture of $10\times10\,mm^2$ was used to switch the polarization of the incoming seed pulse and the amplified outgoing pulse, such that the pulses were confined in the cavity for certain round trips.

A 9-mm-diameter, 100-μm-thick Yb:YAG thin-disk (TRUMPF Scientific Lasers GmbH) was used as the gain medium in the cavity of the regenerative amplifier. The disk has a radius of curvature (ROC) of -2 m and a doping rate of about 7%. It was pumped by CW fiber-coupled diodes at 940 nm wavelength with a 3.5 mm diameter near-flat-top beam profile.

The regenerative amplifier was accommodated in an airtight housing and operated in room temperature. 125 W output average power was achieved at 280 W pump power and 106 round trips, corresponding to 25 mJ pulse energy, and 45% optical-to-optical efficiency. The amplifier was operated in saturation and the cooling system was carefully optimized, which resulted in a highly stabled output. The pulse-to-pulse energy fluctuation is less than 1 % (RMS) within a measurement window of 2 s. The long-term power stability over a 10-hour operation period is shown in Fig. 3.6(a). The amplified beam profile and the amplified spectrum are shown in Fig. 3.6 inset (a-2) and (b), respectively. The amplified

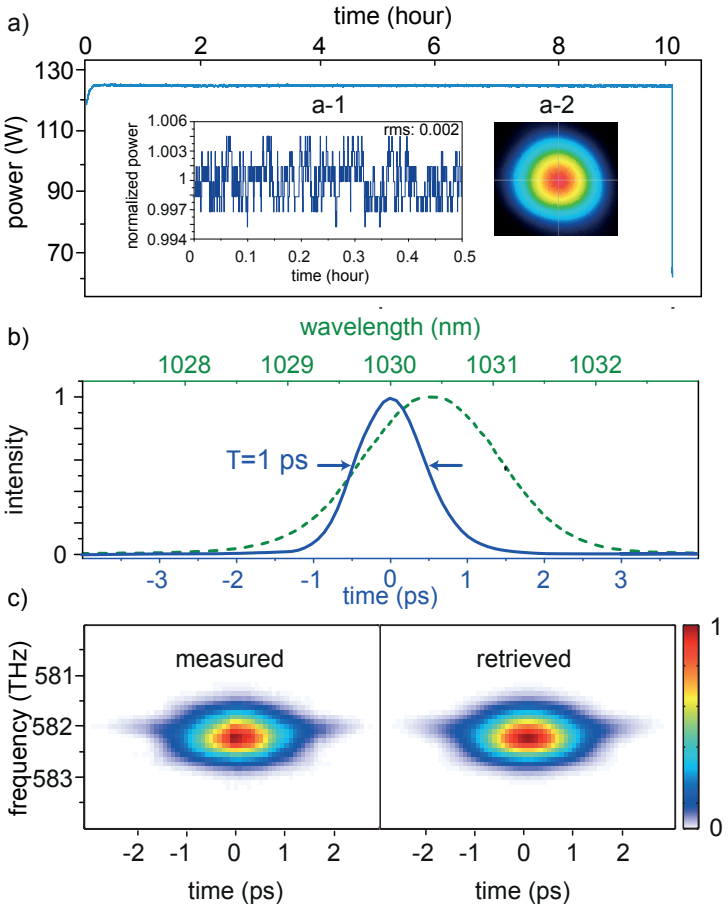

Figure 3.6: Characterization of the Yb:YAG thin-disk amplifier. (a) Average power stability of the Yb:YAG thin-disk amplifier over 10 hours continuous operation, measured by an OPHIR power sensor (L1500W-BB-50-V2). Inset: (a-1): average power fluctuation in half an hour time window, the average power is normalized to its mean value. (a-2): Beam profile of the amplified pulses. (b) The measured spectrum (green dashed) and the retrieved temporal profile (blue) from SH-FROG measurement of the 100 W amplified and temporally compressed pulses after the grating compressor. (c) The measured and retrieved SH-FROG spectrogram. Adapted with permission from [149] © The Optical Society.

beam possess an excellent beam quality with a M^2 value close to 1 (M_x^2=1.08 and M_y^2=1.07).

After amplification in the regenerative amplifier, the 25 mJ pulses were temporally compressed in a grating compressor consisting of two dielectric gratings (line density of 1740 l/mm). 80% throughput efficiency was achieved, corresponding to 20 mJ pulse energy. The retrieved temporal profile of SH-FROG measurement is shown in Figure 3.6(b), and the corresponding measured and retrieved spectrogram are shown in Figure 3.6(c). The compressed pulse has a FWHM pulse duration of 1 ps.

3.1.2 CEP-stable supercontinuum generation

[2]The ultra-broadband CEP-stable seed is of fundamental importance for generating light transients. Since the pump laser in our scheme does not provide CEP-stable pulses, direct generation of broadband CEP-stable seed pulses via spectral broadening of amplifier's output is not possible.

Alternatively, a low-energy CEP-stable broadband oscillator can seed the amplifier, while a fraction of the oscillator's output is used for seeding OPCPAs. However, in this approach the seed pulse has to be temporally synchronized with the pump pulse via active optical synchronization, due to the accumulated temporal jitter of pump pulse through the amplification stage, with up to hundreds of meters-long beam path [153, 154]. Moreover, the obtained seed pulse from the oscillator usually contains low pulse energy, which could cause undesirable superfluorescence and low conversion efficiency in OPCPA chains. Also, the carrier frequency of the available broadband oscillators [29, 155, 156] restricts the carrier frequency of the OPCPAs. These issues can be overcome by scaling the energy of oscillator's pulses in an additional amplifier [157] or by shifting the central frequency via nonlinear processes [72, 74, 158]. Nevertheless, additional laser systems and nonlinear stages together with temporal synchronization, add complexity and decrease the robustness of the system. After all, the CEP and energy stability of the OPCPA amplified pulses still face degradation caused by the residual temporal jitter between pump and seed pulses [159].

Direct generation of ultra-broadband CEP-stable seed pulses from the output of the Yb:YAG thin-disk regenerative amplifier that pumps OPCPAs could overcome such issues and reduces the complexity of the system, since here pump and seed pulses of the OPCPA are generated from the same laser and are intrinsically synchronized. However, direct generation of CEP-stable continuum from picosecond pulses has been found to be challenging, due to the difficulty of SC generation from narrow-band pulses in bulk material. The bulk materials used for filamentation are prone to damage as the required critical peak power by picosecond pulses approaches the damage threshold [160, 161]. In order to generate a stable SC from bulk material, an additional stage for compressing picosecond pulses down

[2]This section is adapted from [136]

to hundreds of femtosecond is required. With a subsequent DFG process, passive CEP-stable idler can be generated at a longer wavelength [50]. Using such CEP-stable pulses for SC generation in bulk result in an ultra-broadband CEP-stable SC spanning from visible to MIR.

In this section, generation of a CEP-stable supercontinuum spanning from 450 to 2500 nm for seeding OPCPAs of the synthesizer, is discussed. Further efforts for extending the spectral coverage towards MIR are demonstrated.

The setup for generating the multi-octave SC is illustrated in Fig. 3.7. Pulses with a total energy of 2.9 mJ are separated by two attenuators from the output of a Yb:YAG, thin-disk regenerative amplifier, to generate CEP-stable pulses for seeding the OPCPA chains.

As the first step, the 1-ps pulses from the thin-disk amplifier need to be spectrally broadened and temporally compressed to a shorter pulse duration for generating a stable and reproducible SC. However, SPM based spectral broadening of ps-pulses in hollow-core-fiber is shown to be unstable [157], and limited to 1 μJ pulse energy in kagome type hollow-core-fibers [162] or large-mode-area waveguides [163]. These systems are usually relatively complex and sensitive to misalignment. The broadened pulses out of large-mode-area waveguides even have a degraded polarization. Therefore, a simple energy-scalable approach for direct shortening of ps-pulses down to hundreds of fs is desired. In this regards, XPW was chosen (block 1 in Fig. 3.7) to compress 1 ps pulses to 670 fs (FWHM)(Fig. 3.8).

XPW [59] is a degenerate four-wave mixing process. The interaction of an intense, linearly polarized pulse with a nonlinear medium generates a new pulse with orthogonal polarization relative to the input pulse polarization. The nonlinear medium has to have an anisotropic third-order nonlinearity and typically an isotropic linear index. The nonlinear intensity gating inherent in XPW process improves the contrast of the generated pulses both temporally and spatially. Moreover, unlike SPM-based broadening, the XPW pulse has a shorter pulse duration than the input pulse by a factor of 0.65, if the process is not saturated [60]. For input pulses in the range of several-hundreds of fs- or ps, material dispersion does not play a critical role compared to few-fs input pulses. Therefore, thicker crystals can be used to increase the conversion efficiency, limited by damage threshold.

In the setup shown in block 1 in Fig. 3.7, 500-μJ energy was separated from amplifier's output by an attenuator consisting of a half waveplate and a thin-film polarizer (TFP). A nanoparticle linear film polarizer (Thorlabs LPNIR100) was used to enhance the polarization contrast of the input pulses. Afterwards, the pulses were focused into a 2-mm-thick, holographic-cut, barium fluoride (BaF_2) crystal by an anti-reflective (AR)-coated convex lens with a focal length of f= 200 mm. The crystal was placed slightly behind the focus, in order to balance the beam divergence and self-focusing [60]. Another AR-coated convex lens (f=200 mm) was used to collimate the beam, and then the XPW pulses containing 5 μJ of energy were separated from the fundamental beam by a TFP. Fig. 3.8 shows the

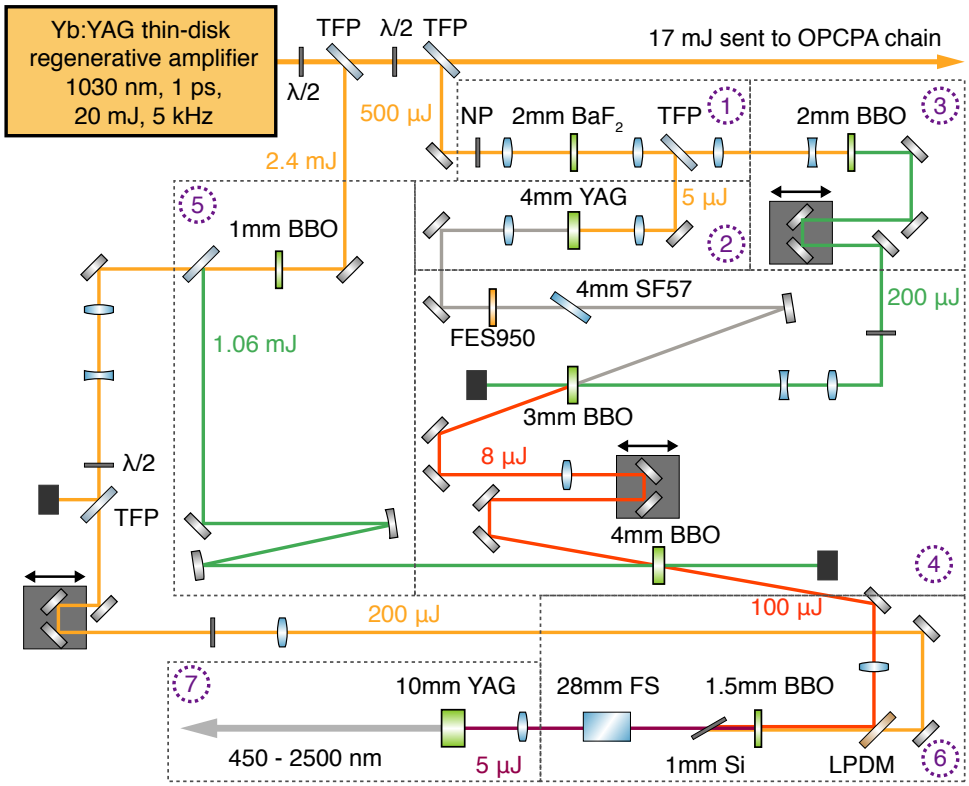

Figure 3.7: Schematic of the supercontinuum generation setup. 2.9 mJ out of the 20 mJ output of a 1-ps, Yb:YAG thin-disk amplifier was used to directly generate the CEP-stable multi-octave supercontinuum from the amplifier. A small portion of the 1 ps pulses with 500 μJ energy was firstly shortened to 670 fs in a XPW (block 1). Afterwards the shortened cross-polarized pulses were separated by a TFP and focused into a 4 mm-YAG crystal to generate a supercontinuum (block 2). The remaining energy in fundamental polarization after XPW was frequency doubled in a BBO crystal (block 3) and used to amplify a small portion of the supercontinuum in the first OPCPA stage (block 4). Another portion of the amplifier pulses with 2.4 mJ energy was split and frequency doubled in a BBO crystal (block 5) and then used to pump the second OPCPA stage (block 4). Later on the amplified pulses were mixed with residual energy (at 1030 nm) of the second harmonic generation stage (block 5) in a BBO crystal for difference frequency generation (block 6). The generated pulses were compressed to 44 fs using 28 mm fused silica plate and later on were focused into a YAG crystal for generation of a CEP-stable, multi-octave spectrum. $\lambda/2$: half wave plate; TFP: thin film polarizer; NP: nanoparticle polarizer; FES950: 950 nm shortpass filter; Si:silicon; FS: fused silica; LPDM: longpass dichroic mirror.

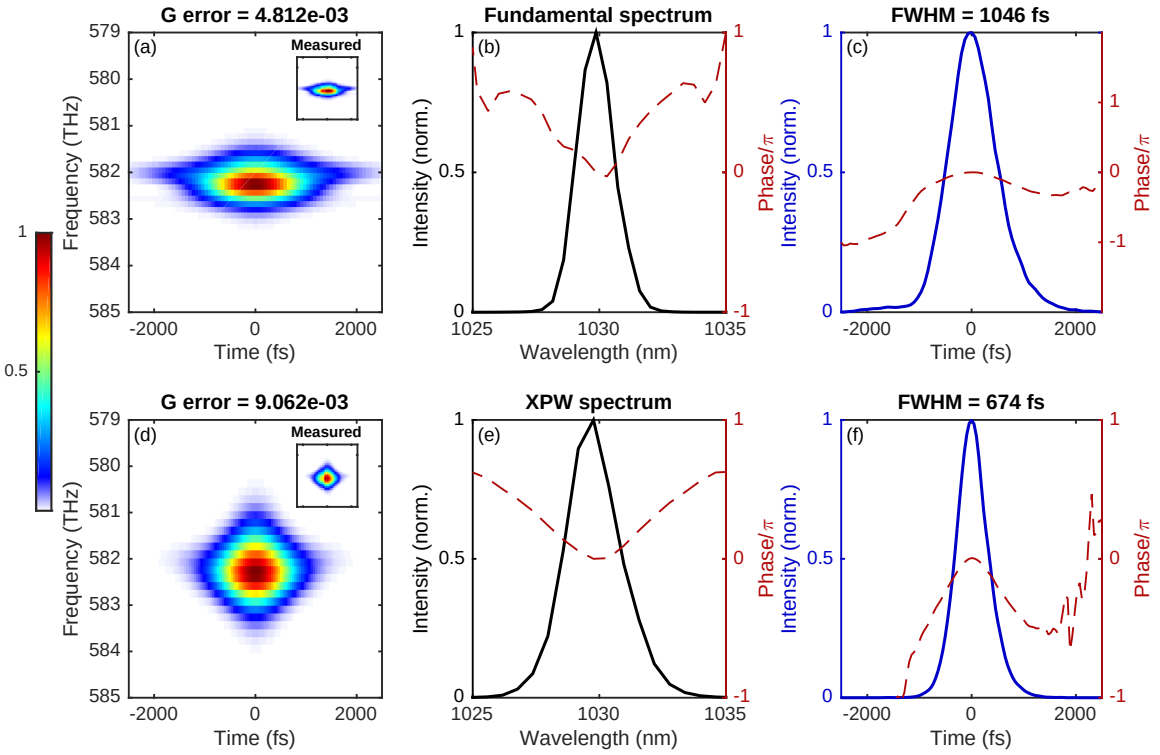

Figure 3.8: FROG measurements of input pulse (first row) and XPW pulse (second row). (a) Retrieved FROG spectrogram of input pulse. Inset: measured FROG spectrogram. (b) Retrieved spectrum (black) and spectral phase (red dashed) of input pulse. (c) Retrieved time envelope (blue) and temporal phase (red dashed) of input pulse. (d) Retrieved FROG spectrogram of XPW pulse. Inset: measured FROG spectrogram. (e) Retrieved spectrum (black) and spectral phase (red dashed) of XPW pulse. (f) Retrieved time envelope (blue) and temporal phase (red dashed) of XPW pulse.

SH-FROG measurements of the fundamental pulse at the input and the XPW pulse at the output. The spectrograms show spectral broadening and temporal shortening. The retrieved pulse duration is 1046 fs at FWHM for input pulse, and 674 fs at FWHM for XPW pulse. Fig. 3.9(a) shows the fundamental (black) and XPW (blue) spectra measured by a grating spectrometer.

The 674 fs pulses were then used to generate a stable and reproducible SC. Undoped sapphire (Al_2O_3) and yttrium aluminum garnet (YAG) are excellent nonlinear media for generating SC, because of their high nonlinearity, good crystalline quality and high optical damage threshold. These parameters make them suitable for SC generation driven by long laser pulses at hundreds of femtoseconds to several picoseconds duration. YAG was chosen as a nonlinear medium for SC generation [164], due to the above mentioned properties and its cubic structure.

The 674 fs pulse containing 5μJ energy was focused into a 4-mm-long YAG crystal by a convex lens (f = 150 mm) and a stable filament with a spectrum spanning from 550 to 1400 nm was generated (block 2 in Fig. 3.7). After collimating the SC by a convex lens (f = 75 mm), two grating spectrometers with silicon (USB2000+, Ocean Optics) and InGaAs detectors (NIRQuest512-1.6, Ocean Optics) were used to characterize the spectrum of the generated filament. The measured spectra are shown in Fig. 3.9(b). A filter was used to remove the strong spectral component at 1030 nm. Both spectra are normalized to one. The generated single filament, stable SC was resistant to optical damage or permanent modification of the YAG crystal in long term operation (months).

CEP-stable pulses at 2 μm can be generated by DFG between 675 nm and 1030 nm spectral components. In order to boost the energy of the generated spectrum to 100 μJ at around 675 nm, two OPCPA stages containing a 3-mm-thick BBO crystal and a 4-mm-thick BBO (both cut at phase matching angle $\theta = 24.5°$, internal noncollinear angle $\alpha = 1.8°$) were used. The spectral components below 950 nm were selected by using a short pass filter (FES950, Thorlabs) and temporally stretched in a 4 mm SF57 glass plate before being sent to OPCPA stages (block 4 in Fig. 3.7). The pump of the first OPCPA stage was generated by frequency doubling of the 490 μJ unconverted energy of the XPW stage in a 2-mm-thick BBO crystal (type I, $\theta = 23°$), resulting in 200 μJ pulses at 515 nm (block 3 in Fig. 3.7). 1.06 mJ, 515 nm pump pulses of the second OPCPA stage were generated by frequency doubling of 2.4 mJ energy from thin-disk amplifier in a 1-mm-thick BBO crystal (type I, $\theta = 23°$) (block 5 in Fig. 3.7). The beam sizes of the pump beams were adjusted to reach 100 GW/cm^2 peak intensity on the crystals, and the seed beam sizes were adjusted accordingly. The amplified spectrum spanned from 625 to 725 nm. Fig. 3.9 (c) shows the measured amplified spectra after each OPCPA stage.

200 μJ of the unconverted energy of the second SHG stage (block 5 in Fig. 3.7) was reused and mixed with the amplified pulses from the second OPCPA in a DFG stage, containing a 1.5-mm-thick BBO crystal ($\theta = 20.1^o$) with type I phase matching in a collinear

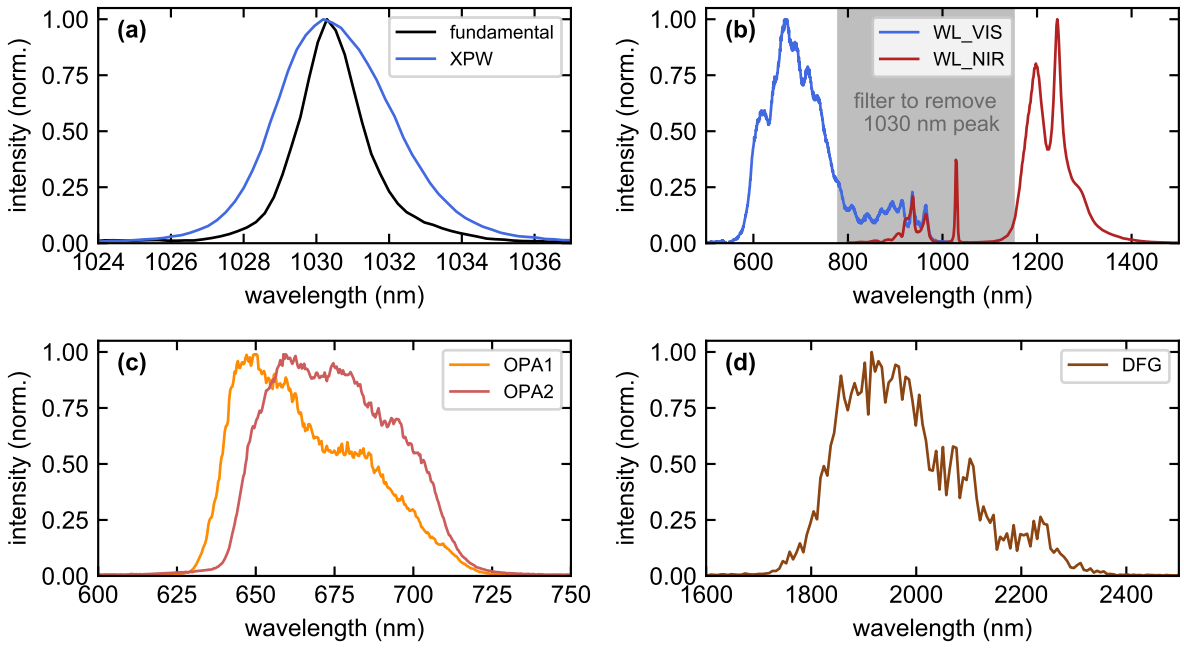

Figure 3.9: (a) Measured fundamental spectrum at the input of XPW stage (black), and the broadened XPW spectrum (blue) after BaF_2 crystal which separated by thin film polarizer. (b) Measured spectrum of the supercontinuum generated in a 4 mm YAG crystal by XPW pulses, a filter was used to remove the strong 1030 nm peak, the visible spectrum (blue) and the near-infrared spectrum (red) are normalized individually. (c) Measured amplified spectrum after the first OPCPA stage (orange) and second OPCPA stage (red). (d) The difference frequency generation between the regenerative amplifier and the OPCPA pulses in a 1.5-mm-thick BBO crystal results in a broadband spectrum centered at 2 μm (brown). The generated pulses are intrinsically CEP-stable.

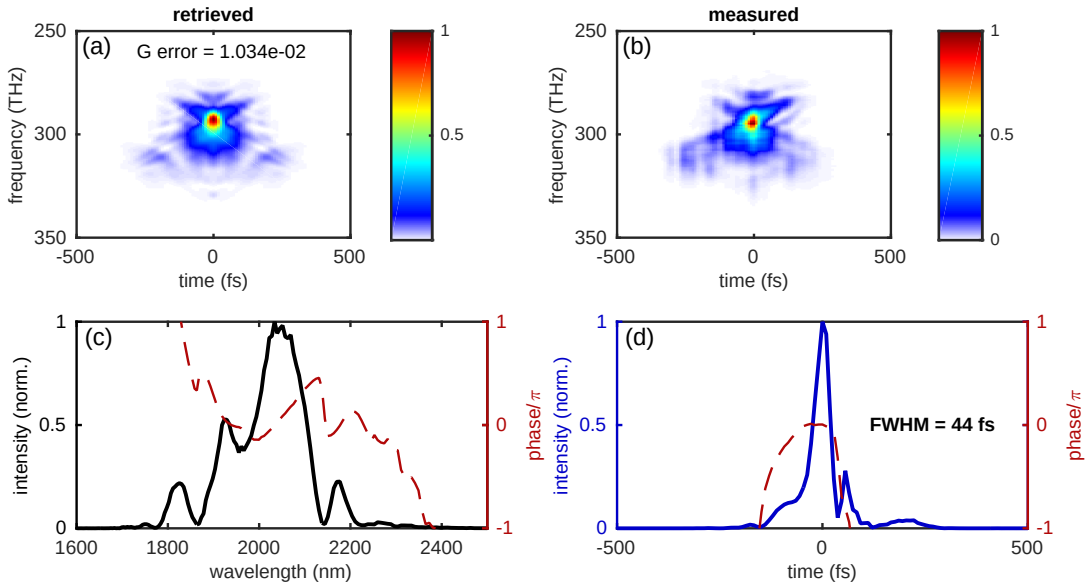

Figure 3.10: FROG measurement of the DFG pulse compressed by 28 mm fused silica plate. (a) Retrieved FROG spectrogram. (b) Measured FROG spectrogram. (c) Retrieved spectrum (black) and spectral phase (red dashed). (d) Retrieved time envelope (blue) and temporal phase (red dashed).

geometry (block 6 in Fig. 3.7). Collinear geometry is necessary to avoid angular chirp of the generated pulses. The spectrum of the generated 5-μJ, intrinsically CEP-stable pulses is shown in Fig. 3.9(d), which spans from 1700 to 2400 nm. The difference frequency pulses have a stable CEP due to the identical phase fluctuations of both the seed and pump pulses [165].

The generated pulses were separated from the driving pulses by using a 1.5 mm silicon plate, and partially compressed by material dispersion. The resultant 44-fs (FWHM) pulses after propagating through a 28-mm-thick uncoated fused silica glass plate were characterized by using a SH-FROG containing a 200-μm-thick BBO crystal. Figure 3.10 shows the measured SH-FROG trace, its retrieved counterpart and the temporal profile of the compressed pulses. The evaluated spectral phase is well behaved and permits for the compression to its bandwidth limit by employing tailored chirped mirrors.

CEP-stable, 44-fs pulses were then focused into a 10-mm-thick uncoated YAG crystal by using an AR-coated Calcium fluoride (CaF_2) lens (f=150 mm) for SC generation (block 7 in Fig. 3.7). The SC generation preserves the CEP-stability of the driving pulse. Therefore, the multi-octave SC after YAG is also CEP stable. Two grating spectrometers with silicon (USB2000+, Ocean Optics) and InGaAs detectors (NIRQuest256-2.5, Ocean Optics) were used to characterize the spectrum of the generated SC. The measured spectrum is shown

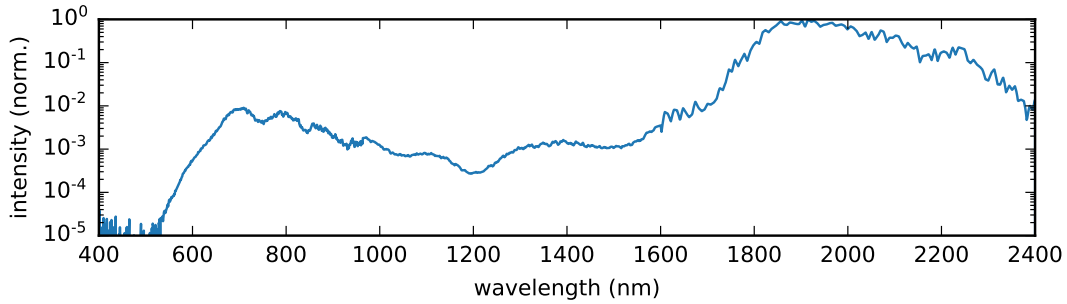

Figure 3.11: Measured spectrum of the supercontinuum generated in a 10 mm YAG crystal driven by 44 fs compressed DFG pulses. It is measured by three different grating spectrometers, calibrated and merged together.

in Fig. 3.11. Its short-wavelength side extends to 500 nm. The detection of wavelengths beyond 2400 nm was not possible with the available spectrometers and calibration source.

The spectral coverage of the presented setup can be extended towards MIR, which is described with detail in the section 3.1.2.

Reducing the footprint and complexity In the described setup, the unconverted energy of the XPW stage (block 1 in Fig. 3.7) was recycled for SHG and to pump the first OPCPA stage to increase the total efficiency. However, this limited the amplified energy of the first OPCPA stage. Adding a second OPCPA stage made the setup more complex. The footprint of the described setup can be reduced with a few modifications.

The modified setup is illustrated in Fig. 3.12. Pulses with 1.6 mJ energy were split off from the output of the amplifier. Afterwards, 140-μJ energy was separated and focused into a 4-mm-thick, holographic-cut, BaF_2 crystal. 5 μJ XPW pulses were separated by a TFP. Here a lower input energy was used for XPW generation, due to the tighter focusing in combination with a thicker crystal. Fig. 3.13 shows the FROG measurements of the fundamental pulse and the XPW pulse. The shortened pulses were used for SC in a 4-mm-thick YAG, and spectral range between 600 - 950 was filtered by a customized dichroic filter and seeded the first OPCPA stage (block 4 in Fig. 3.12). A 4 mm SF57 glass plate was used to temporally stretch the seed pulses, so that to match the pump. 1-mm-thick BBO crystal was used to convert 1.4 mJ pulse at 1030 nm to 860 μJ pulses at 515 nm (block 3 in Fig. 3.12). The nonlinear crystal used in OPCPA was a 4-mm-thick BBO crystal at phase matching angle $\theta = 25.7^o$ and noncollinear angle $\alpha = 2.1^o$. Fig. 3.14 (a) shows the phase matching calculated by phase mismatch factor $\mathrm{sinc}^2(\Delta kL/2)$ for a 4-mm-thick BBO crystal at the above mentioned angels, and the measured amplified spectrum containing 120 μJ energy.

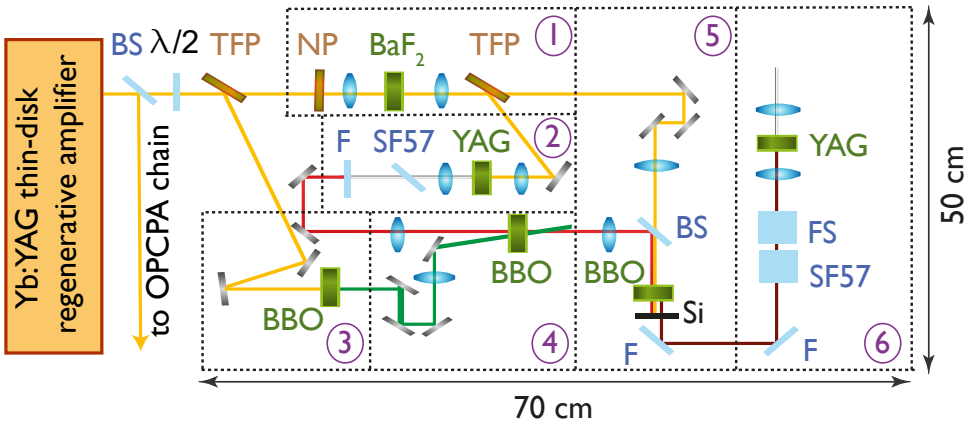

Figure 3.12: Schematic of the compact seed generation setup. 1.6 mJ out of the 20 mJ output of a 1-ps, Yb:YAG thin-disk amplifier was used to directly generate the CEP-stable multi-octave supercontinuum from the amplifier. A small portion of the 1 ps pulses was firstly shortened to 670 fs using XPW (block 1). Afterward, the shortened cross-polarized pulses were separated by a TFP and focused into a 4 mm-YAG crystal to generate a supercontinuum (block 2). The rest portion of the 1 ps pulses with 1.4 mJ energy was frequency doubled in a BBO crystal (block 3) and then used to amplify a selected spectral region of the supercontinuum in an OPCPA stage (block 4). Thereafter the amplified pulses were mixed with the unconverted energy from the XPW stage for difference frequency generation using a BBO crystal (block 5). After a silicon plate to block the driving pulses and several fused silica plates for compression, the generated pulses centered at 2 μm wavelength were compressed to 40 fs. Focusing such pulses into a YAG crystal leads to the generation of a CEP-stable, multi-octave supercontinuum. The setup has a compact size of 70×50 cm^2. BS: beam splitter; TFP: thin film polarizer; NP: nanoparticle polarizer; F: filter; Si:silicon; FS: fused silica. Adapted with permission from [136] © The Optical Society.

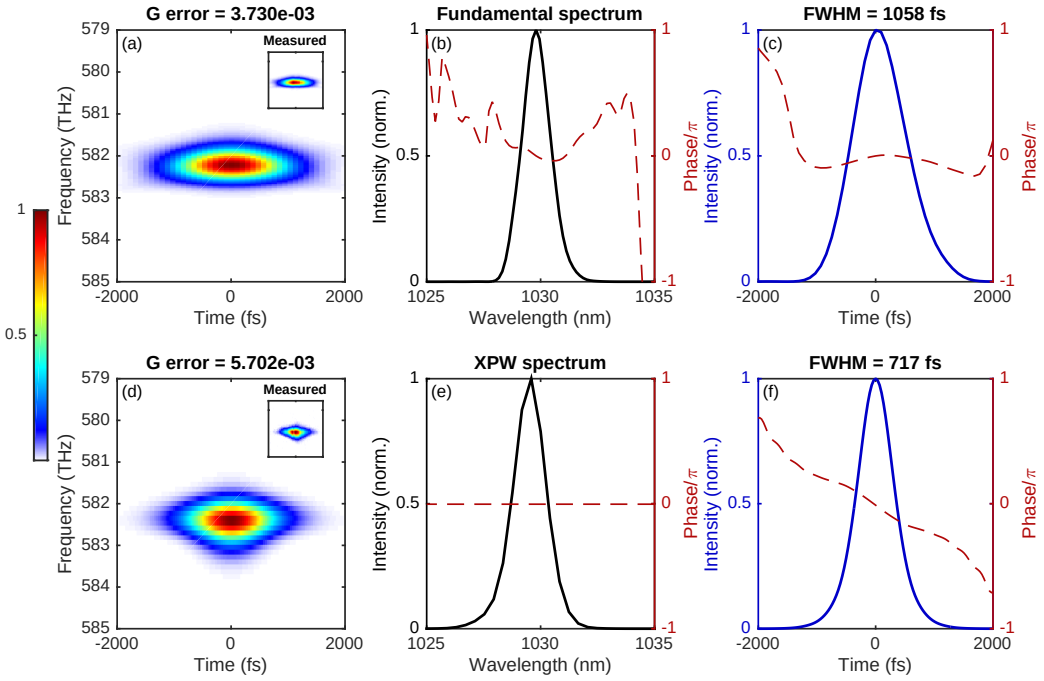

Figure 3.13: FROG measurements of input pulse (first row) and XPW pulse (second row) in the compact seed generation setup. (a) Retrieved FROG spectrogram of input pulse. Inset: measured FROG spectrogram. (b) Retrieved spectrum (black) and spectral phase (red dashed) of input pulse. (c) Retrieved time envelope (blue) and temporal phase (red dashed) of input pulse. (d) Retrieved FROG spectrogram of XPW pulse. Inset: measured FROG spectrogram. (e) Retrieved spectrum (black) and spectral phase (red dashed) of XPW pulse. (f) Retrieved time envelope (blue) and temporal phase (red dashed) of XPW pulse.

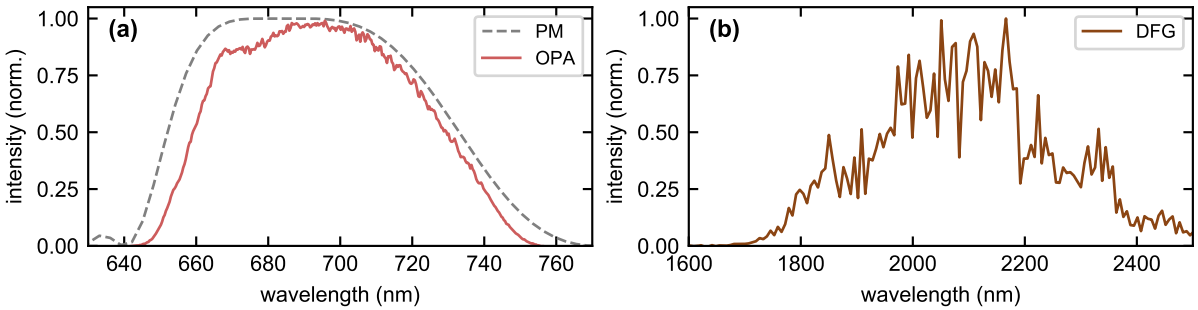

Figure 3.14: (a) The phase matching calculated by the phase mismatch factor $\mathrm{sinc}^2(\Delta kL/2)$ for a 4-mm-thick BBO crystal at $\theta = 25.7^o$ and noncollinear angle $\alpha = 2.1^o$ (grey dashed), and the measured amplified spectrum (red). (b) DFG spectrum in 2 mm BBO (brown).

The residual 120 μJ unconverted pulses of the XPW stage, along with the amplified pulses were sent to a 1.5-mm-thick BBO (type I, θ= 20^o) for DFG, resulting in CEP-stable pulses with 4-μJ energy (block 5 in Fig. 3.12 and Fig. 3.14(b)).

By using material dispersion of 29-mm-thick uncoated infrared-grade fused silica plate, the DFG pulses were compressed to 40 fs. Figure 3.15 shows the retrieved and measured SH-FROG spectrograms, the retrieved spectrum, the retrieved temporal profile, and the corresponding phases.

The compressed 40-fs pulses were then focused into a 10-mm-thick uncoated YAG crystal by using a coated CaF_2 lens (f=75 mm) for SC generation (block 6 in Fig. 3.12). The measured spectrum is shown in Fig. 3.16, extending to 450 nm.

An f-2f interferometry measurement was performed in order to verify the CEP stability of the generated multi-octave spectrum. Figure 3.17(a) presents the layout of the f-2f interferometer. A customized beam splitter was used to split the SC spectrum into two channels at 1700 nm. The reflected beam containing spectral components above 1700 nm, was then frequency doubled in a 2 mm lithium niobate ($LiNbO_3$) crystal. The transmitted beam with spectral components below 1700 nm was delayed and then interferometrically combined with the frequency doubled beam. Figure 3.17(b) shows the spectrogram measured for the CEP fluctuations over 10 minutes operation. The reconstructed CEP, as shown in Fig. 3.17(c), presents a drift of 144 mrad (4 ms integration time). The 100-min measurement shown in Fig. 3.17(d) presents a drift of 90 mrad (30 ms integration time).

In order to evaluate the spectral reproducibility of the SC, the low frequency edge of the SC spectrum was measured over 120 s. The measured spectra (detector integration time: 1 ms) showed less than 0.7 % (RMS) deviation of the Fourier transform limit, and possessed an excellent reproducibility.

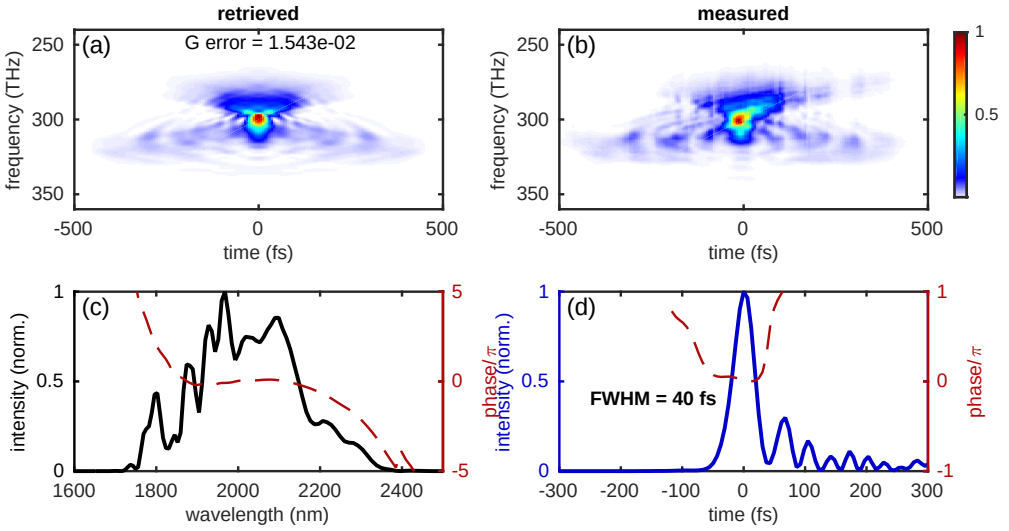

Figure 3.15: SH-FROG measurement of the DFG pulse compressed by 29 mm fused silica plate. (a) Retrieved FROG spectrogram. (b) Measured FROG spectrogram. (c) Retrieved spectrum (black) and spectral phase (red dashed). (d) Retrieved time envelope (blue) and temporal phase (red dashed).

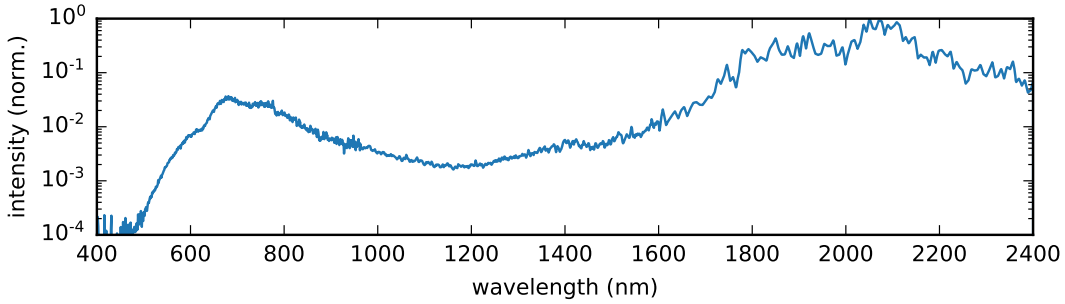

Figure 3.16: Measured spectrum of the supercontinuum generated in a 10 mm YAG crystal driven by 40 fs compressed DFG pulses. It is measured by three different grating spectrometers, calibrated and merged together.

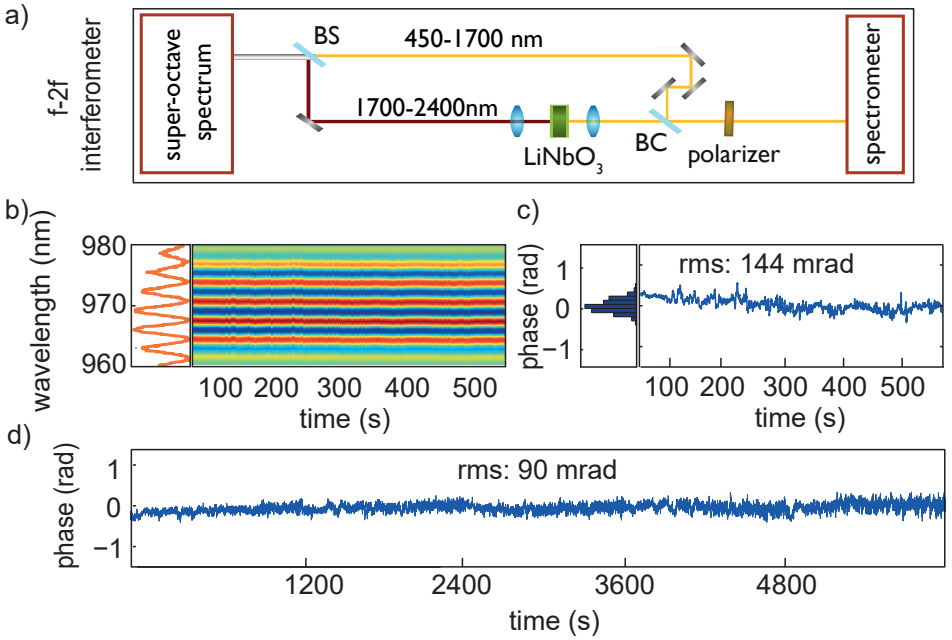

Figure 3.17: (a) Schematic layout of the f-2f interferometer for checking the intensity and phase stability of the supercontinuum. The visible to near-infrared part of the fundamental in one arm, and the second harmonic of the fundamental with orthogonal polarization generated from a $LiNbO_3$ crystal in another arm are interferometrically overlapped by a beamsplitter cube, and are projected onto the same polarization state using a polarizer. (b) The resolved interference fringes from the f-2f interferometer (left) and variation of the interference pattern over 600 s (right). (c) Histogram (left) and reconstructed CEP fluctuations obtained from the f-2f measurement. The retrieved fluctuations yield a 144 mrad CEP jitter over 600 s measurement time (detector's integration time: 4 ms). (d) Reconstructed CEP fluctuations over 6000 s yielding 90 mrad jitter (detector's integration time: 30 ms). BC: beam combiner; BS: beam splitter. Adapted with permission from [136] © The Optical Society.

Extension towards mid-infrared CEP-stable, few-cycle MIR laser sources are essential for various applications [166–168], such as fundamental science [169] and molecular fingerprint spectroscopy [170–172]. Due to the lack of suitable laser media, optical parametric processes such as DFG and optical rectification in nonlinear crystals, filaments, or plasmas, are usually used to generate broadband coherent MIR sources [170, 173]. The following part discusses the capability of the above described setup for generating μJ-level MIR pulses in 4 - 11 μm spectral range.

3.9 - 5.4 μm MIR generation in $LiNbO_3$ The demonstrated OPCPA in block 4 of Fig. 3.7 can be tuned to amplify different spectra range. In the subsequent DFG stage, the generated difference frequency signal is defined by the frequency difference between the two input pulses via energy conservation relation $\omega_i = \omega_p - \omega_s$. For example, 3.9 - 5.4 μm MIR pulses can be generated by DFG between 1030 nm pulses and 815 - 865 nm pulses.

To this end, a 2 mm-thick 5 mol % MgO doped $LiNbO_3$ crystal was used to replace the 1.5 mm-thick BBO at the DFG stage, as BBO absorbs spectral components beyond 3 μm. An additional 4 mm SF57 glass plate was added (in total 8 mm SF57) to further stretch the SC before the first OPCPA stage, so that the amplified energy was concentrated in a narrower bandwidth, but still fully supported the DFG phase matching bandwidth in a 2 mm-thick $LiNbO_3$. The phase matching angle of the BBO crystals in OPCPA stages were slightly tuned to amplify the spectral range between 800 and 880 nm at around $\theta = 25.6°$, with the internal noncollinear angle of $\alpha = 1.8°$. Fig. 3.18(a) shows the amplified spectra measured by a grating spectrometer (USB2000+, Ocean Optics). The amplified spectrum and narrowband pulses at 1030 nm were sent to the 2 mm $LiNbO_3$ for DFG. By tuning the phase matching angle θ between 44.3° and 47°, the generated difference frequency can be tuned from 4000 nm to 5300 nm. Fig. 3.18 (c) shows the obtained spectra measure by a Fourier transform infrared (FTIR) spectrometer (L-FTS, LASNIX). Fig. 3.18 (b) shows the obtained average power at different central wavelength. The maximum power of 4 mW was measured at 5300 nm central wavelength, corresponding to 0.8 μJ pulse energy.

5 - 11 μm MIR generation in LGS The generated difference frequency in $LiNbO_3$ is limited to 5.5 μm due to the absorption, similar to most of the oxide materials. By employing non-oxide materials, such as LGS which has a much broader transparency range (0.32 - 11.6μm), the generated spectrum could reach beyond 5.5 μm. Besides, LGS's large band gap at 4eV leads to very weak two-photon absorption when irradiated at 1030 nm. This is beneficial for DFG pumped by power-scalable 1030 nm sources.

0.5 mm-thick LGS crystal was used to extend the spectrum. To this end, the phase matching angle of the BBO crystals in OPCPA stages were tuned to $\theta = 24.6°$, while the internal noncollinear angle α was decreased to 1.3°, resulting in amplified spectral range of 1080 nm to 1250 nm. The red curve in Fig. 3.19(a) shows the amplified spectra measured by

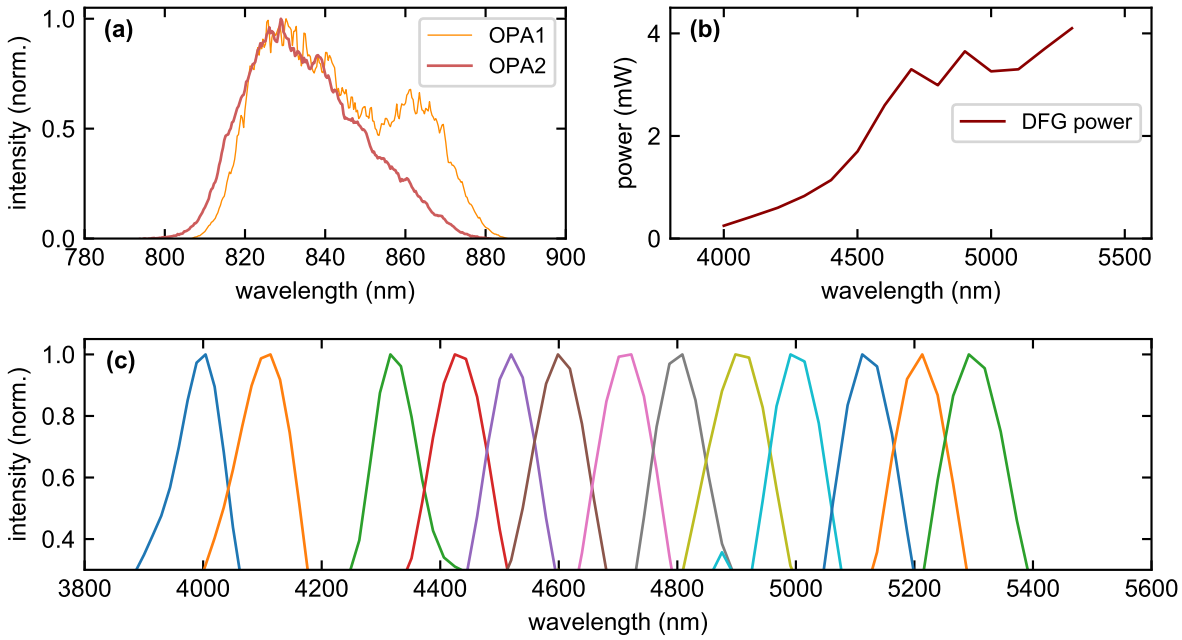

Figure 3.18: (a) By further stretching the supercontinuum with 8 mm SF57 glass plate as seed, and changing the delay between seed and pump pulses in OPCPA stages, the measured amplified spectrum after the first OPCPA stage (orange) and second OPCPA stage (red) are shifted to around 800 - 880 nm. (b) Generated DFG power versus central wavelength in a 2 mm-thick lithium niobate ($LiNbO_3$) crystal. (c) Measured DFG spectrum by changing the phase matching angle of the $LiNbO_3$ crystal.

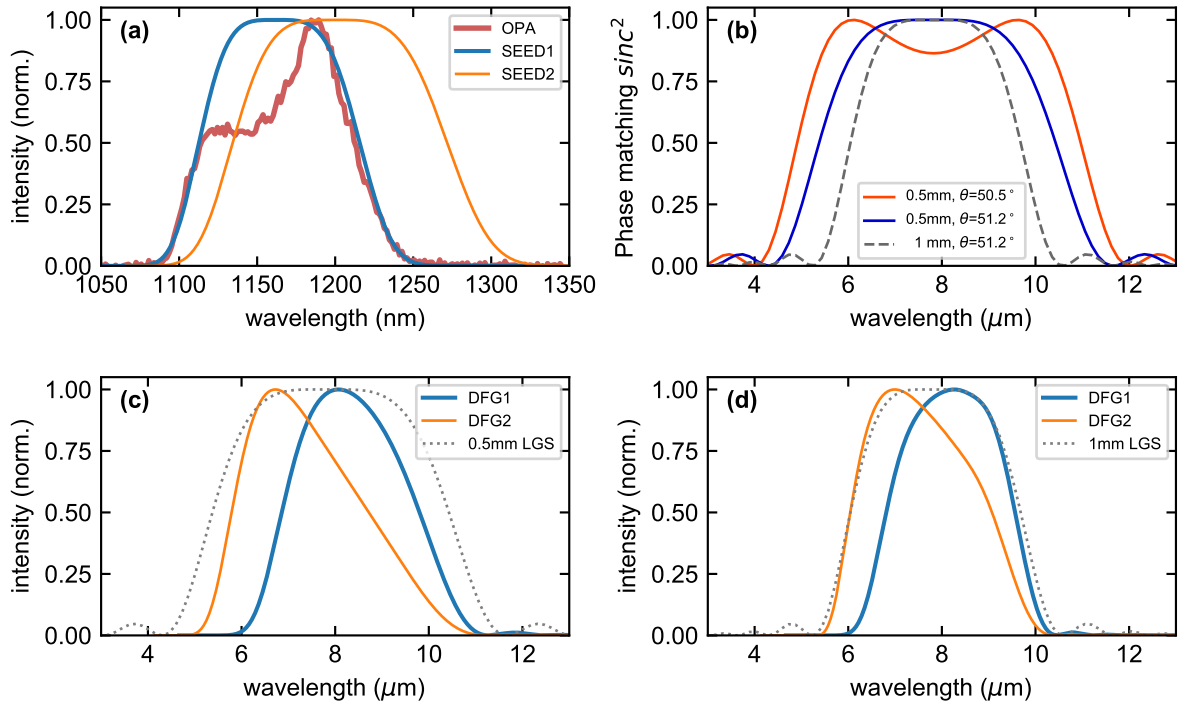

Figure 3.19: Simulations of 5 - 11 μm mid-infrared generation in LGS crystal. (a) The measured amplified spectrum (red) in OPCPA stages, which was shifted to around 1080 - 1250 nm. An input seed spectrum (blue) with a similar bandwidth of the amplified spectrum was used in the DFG simulation case 1. Seediing the DFG with a slightly broader and red shifted seed spectrum could fully utilize the phase-matching bandwidth in LGS crystal. For this reason, a broader red-shifted input seed spectrum (orange) was used in the DFG simulation case 2. (b) The phase matching calculated by the phase mismatch factor $\mathrm{sinc}^2(\Delta kL/2)$ at perfect phase matching for a 0.5 mm (black) and 1 mm (grey dashed) LGS crystal. Tune the phase matching angle slightly can further optimize the bandwidth (red). (c) The simulated output DFG spectrum of case 1 (blue), and case 2 (orange) in a 0.5 mm LGS crystal with the phase mismatch factor in dotted grey line. (d) The simulated output DFG spectrum of case 1 (blue), the phase matching and case 2 (orange) in a 1 mm LGS crystal with the phase mismatch factor in dotted grey line.

a grating spectrometer (NIRQuest512-1.6, Ocean Optics). In comparison to the previous cases, amplifying spectral components above 1030 nm in OPCPA stage is beneficial for boosting the DFG pulses, since 1030 nm pulses act as a pump in the DFG process, and are available at high energy.

The phase mismatch and absorption in the LGS crystal for spectral components beyond 11 μm limit the bandwidth at the DFG stage. Fig. 3.19 (b) shows the phase mismatch $\mathrm{sinc}^2(\Delta \mathrm{kL}/2)$ for the perfect phase matching in a 0.5 mm LGS crystal (blue curve) and 1 mm LGS crystal(dashed grey), when pumped by pulses at 1030 nm. Tuning the θ by 0.7° could increase the bandwidth (red curve).

Due to the lack of diagnostics for this wavelength range at kHz repetition rate, the DFG stage was numerically studied. The Simulation System for Optical Science (SISYFOS) code [174, 175] was used to perform the three-dimensional simulation. The blue curve in Fig. 3.19 (a) shows the simulated seed spectrum with a similar bandwidth as obtained from experiment (red), while the orange curve shows a slightly broader and red-shifted spectrum to fully utilize the phase-matching bandwidth in LGS. Fig. 3.19 (c)(d) show the simulated DFG spectra with different input seed spectra shown in Fig. 3.19 (a). In all simulations a type-I LGS crystal was used, where the phase matching angle θ between the optical axis and the (collinear) pump and signal beams was set to 51.2 °. The seed 1 (Fig. 3.19 (a), blue) and seed 2 (Fig. 3.19 (a), orange) were taken to have a Gaussian beam profile and a 4th-order super-Gaussian spectrum, ranging from 1080 to 1250 nm and 1100 to 1325 nm respectively. Both pulses were linearly chirped to 1 ps. The pump was taken to have Gaussian spatial temporal profile, centered at 1030 nm and 1 ps duration at FWHM. The d_{eff} of the LGS crystal was taken to be 4.6 pm/V and the Sellmeier coefficients are taken from [176]. The pump energy was fixed at 1.3 mJ, the maximum available unconverted energy of the second SHG stage (block 5 in Fig. 3.7). The width of the pump beam was adjusted to have 100 GW/cm^2 on-axis peak intensity on the crystal. The same width was applied for the seed beam, and the simulation was repeated for different crystal thicknesses and seed spectra. Table 3.1 summarizes the input parameters used in the simulation. Table 3.2 shows the spectral bandwidth and the corresponding energy for different cases.

With 0.5 mm LGS crystal, seeded by 1080 - 1250 nm (SEED1, Fig 3.19(a)), 9.8 μJ idler pulse covering 6 - 11 μm range could be generated (DFG1, Fig 3.19(c)). The LGS phase matching bandwidth could be further utilized, if the seed spectrum was slightly shifted to 1100 - 1325 nm (SEED2, Fig 3.19(a)). In this case the idler energy would be increased to 15.7 μJ with a bandwidth of 5 - 10.8 μm (DFG2, Fig 3.19(c)), supporting a 34.2 fs FTL pulse duration (Fig 3.20(a)).

Using 1-mm LGS increases the conversion efficiency at the cost of the spectral bandwidth. Up to 59.7 μJ (298.5 mW) energy at 5.4 - 10.2 μm range (DFG2, Fig 3.19(d)) could be generated when seeded by 1100 - 1325 nm (SEED2, Fig 3.19(a)). In this case the FTL

Table 3.1: Input parameters for simulating the DFG stage reported in Fig. 3.19. L_c: crystal length, d_{eff}: effective nonlinearity, α: noncollinear internal seed-pump angle, E_{pump}: pump pulse energy, E_{seed}: seed pulse energy, ϕ_{pump}: pump beam diameter (FWHM), ϕ_{seed}: seed beam diameter (FWHM).

Crystal	L_c (mm)	θ (degree)	ϕ (degree)	d_{eff} (pm/V)
LGS	0.5 / 1	51.2	0	4.6
α (degree)	E_{pump} (mJ)	E_{seed} (mJ)	ϕ_{pump} (mm)	ϕ_{seed} (mm)
0 (collinear)	1.3	0.1	1.0	1.0

Table 3.2: Simulation output parameters of the DFG stage reported in Fig. 3.19. L_c: crystal length, E_{idler}: idler pulse energy, FTL: Fourier transform limit.

Case	L_c (mm)	idler bandwidth (μm)	FTL (fs)	E_{idler} (μJ)
Fig. 3.19 (c)-DFG1	0.5	6 - 11	45.4	9.8
Fig. 3.19 (c)-DFG2	0.5	5 - 10.8	34.2	15.7
Fig. 3.19 (d)-DFG1	1	6 - 10.3	50.2	46.4
Fig. 3.19 (d)-DFG2	1	5.4 - 10.2	39.9	59.7

pulse duration becomes slightly longer at 39.9 fs (Fig 3.20(b)). Using longer LGS crystal to further increase the conversion efficiency will face phase modulation and beam profile distortion, due to the saturation.

Conclusion In conclusion, the direct generation of CEP-stable SC from a 1-ps, Yb:YAG thin-disk amplifier was demonstrated. The generated SC contains 4 μJ energy with a spectrum spanning from 450 nm to beyond 2500 nm. The demonstrated concept is scalable to higher average- and peak-power by replacing the final broadening stage with a gas-filled hollow waveguide to avoid optical breakdown [177]. With the help of customized broadband dielectric beamsplitters [178], the generated SC can be divided into several spectral regions to seed multi-channel field synthesizers, without the need for any additional temporal synchronization at OPCPA stages [93, 153, 154]. Moreover, a higher seed energy in this scheme decreases the amplification of superfluorescence [179]. It is shown that the same setup is capable of delivering μJ-level pulses at 4 - 11 μm spectral reange. Simulation predicts a maximum pulse energy of 59.7 μJ over 5.4 to 10.2 μm bandwidth, supporting few-cycle pulses with FTL of 39.9 fs by using availlable pump energy. Further scaling of

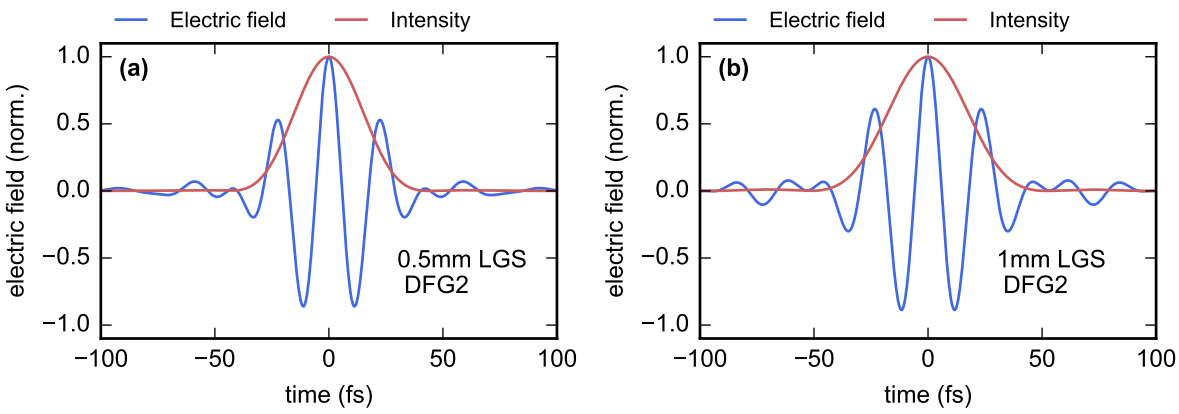

Figure 3.20: (a) Calculated mid-infrared pulse shape based on the simulated spectrum shown in Fig 3.19(c)-DFG2, with a FTL limit of 34.2 fs. (b) Calculated mid-infrared pulse shape based on the simulated spectrum shown in Fig 3.19(d)-DFG2, with a FTL limit of 39.9 fs.

the pulse energy is possible, however, limited by the available LGS crystal size. The generated multi-microjoul-energy, CEP-stable multi-octave pulses are also directly applicable to femtosecond time-resolved spectroscopy.

3.1.3 OPCPA channels

The CEP-stable SC shown in section 3.1.2 fulfills the requirements to seed the synthesizer presented in section 3.1. This section discuses the amplification of the SC in two OPCPA channels centered at 2μm and 1μm. A broadband dielectric beam splitter [178] was used to divide the SC into two spectral regions, and to feed to the OPCPA channels for energy scaling.

2μm OPCPA channel The seed pulses has to be temporally chirped, in order to overlap with the temporal gain window set by the pump pulse duration. For 1 ps pump pulses the dispersion can be managed simply by using material dispersion. However, higher order dispersion become more critical when dealing with a broad bandwidth. Especially when material has a zero dispersion wavelength (ZDW) in the desired spectrum, higher order dispersion become dominant, resulting in a nonlinear chirp. Among typical infrared materials, silicon and ZnSe are suitable for dispersion control at 2μm, due to the absence of ZDW at 2μm. Since ZnSe has a lower GDD and its nonvanishing $\chi^{(2)}$ leads to second harmonic generation, silicon is used for the dispersion control. In order to use the positive GDD of silicon for pulse compression, pulses have to be negatively chirped at OPCPA

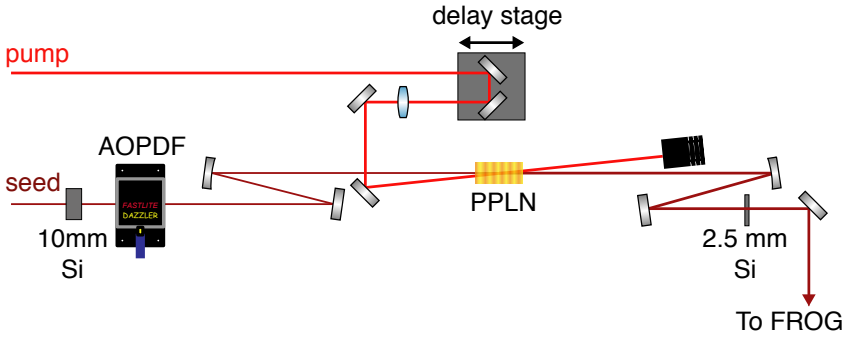

Figure 3.21: Schematic layout of the 2μm OPCPA setup. Si: silicon; AOPDF: acousto-optic programmable dispersive filter; PPLN: periodically poled lithium niobate; FROG: frequency-resolved optical gating.

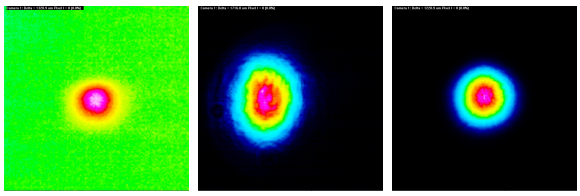

(a) (b) (c)

Figure 3.22: Beam profiles in the 2μm OPCPA. (a) Seed beam profile at crystal. (b) Pump beam profile at crystal. (c) Amplified seed beam profile. All taken by a CMOS camera (DataRay, BladeCam-HR). For 2 μm beam, two photon absorption effect in the silicon sensor was utilized.

stages. An acousto-optic programmable dispersive filter (AOPDF) (Fastlite, HR45-1450-3000 Dazzler system) is used to introduce negative chirp on the seed pulses. The device allows for phase and amplitude shaping with a maximum GD of 10 ps. AOPDF's crystal (TeO_2) has a large n_2 and low damage threshold. Therefore, it's used before the OPCPA stage. A 10-mm-thick silicon plate was introduced in front of the AOPDF to increase the diffraction efficiency.

After propagating through the 10-mm-thick silicon plate and AOPDF, the MIR seed pulses are focused into a 2-mm-thick MgO doped periodically poled lithium niobate (PPLN) crystal with a poling period of 30.64 μm for amplification. The spatial profile of the focused seed beam is shown in the Fig. 3.22(a), measured by a CMOS camera (DataRay, BladeCam-HR). The CMOS camera is able to measure the beam profile of the 2 μm seed beam due to the two photon absorption in the silicon sensor. Fig. 3.23(a) shows the seed spectrum before AOPDF and after propagating through AOPDF and PPLN crystal.

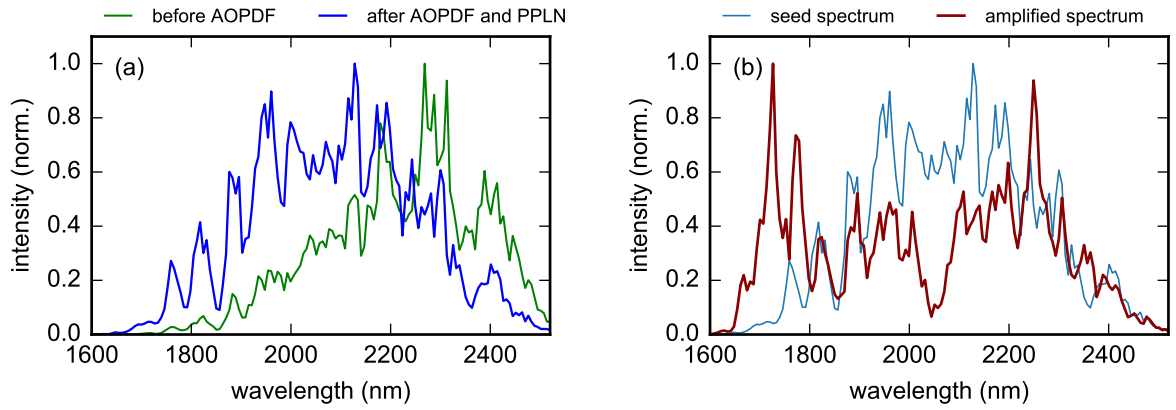

Figure 3.23: (a) The seed spectrum of 2μm OPCPA measured before AOPDF (green), after AOPDF and PPLN with pump pulse blocked (blue). (b) The measured amplified spectrum (red) in comparison with the seed spectrum when pump pulses were blocked (blue).

180 μJ pulses at 1030 nm with the peak intensity of 30 GW/cm^2 were used to pump the OPCPA stage. The spatial profile of the pump is shown in the Fig. 3.22(b). 1° external angle between the seed and pump beams was introduced to facilitate the separation of the amplified seed beam. Fig. 3.23(b) shows the spectrum of the amplified MIR pulses with 5 μJ energy, in comparison to the seed spectrum. Fig. 3.22(c) shows the spatial profile of the amplified beam.

After the parametric amplification, the residual of the pump was filtered by a long-pass filter with a cut-on wavelength of 1500 nm (Thorlabs GmbH, FELH1500). The amplified pulses were compressed using a 2.5-mm-thick silicon. The residual phase was measured by a SH-FROG and feed back to the AOPDF for the final compensation, which resulted in 18 fs pulses. Fig. 3.24 shows the measured and retrieved spectrograms, the retrieved spectral and temporal intensity profile and the corresponding phase of the MIR pulse. This measurement was done by a SH-FROG containing a 100-μm-thick BBO crystal.

1 μm OPCPA channel In NIR channel, the NIR portion of the seed was temporally and spatially overlapped with the 0.8 mJ, 515 nm pump in a single-stage NOPA. A 4-mm-thick lithium triborate (LBO) crystal (type I, phase-matching angle $\phi = 15^o$, internal non-collinear angle $\alpha = 1.05^o$) was used for amplification. The LBO crystal was placed slightly after the focus of the pump to reduce the influence of self-focusing, where the pump has a size of 850 μm (FWHM), corresponding to 130 GW/cm^2 peak intensity. The seed beam was focused to 650 μm (FWHM) spot size, approximately 80 % of the pump beam. After parametric amplification in the crystal, the amplified signal beam was collimated

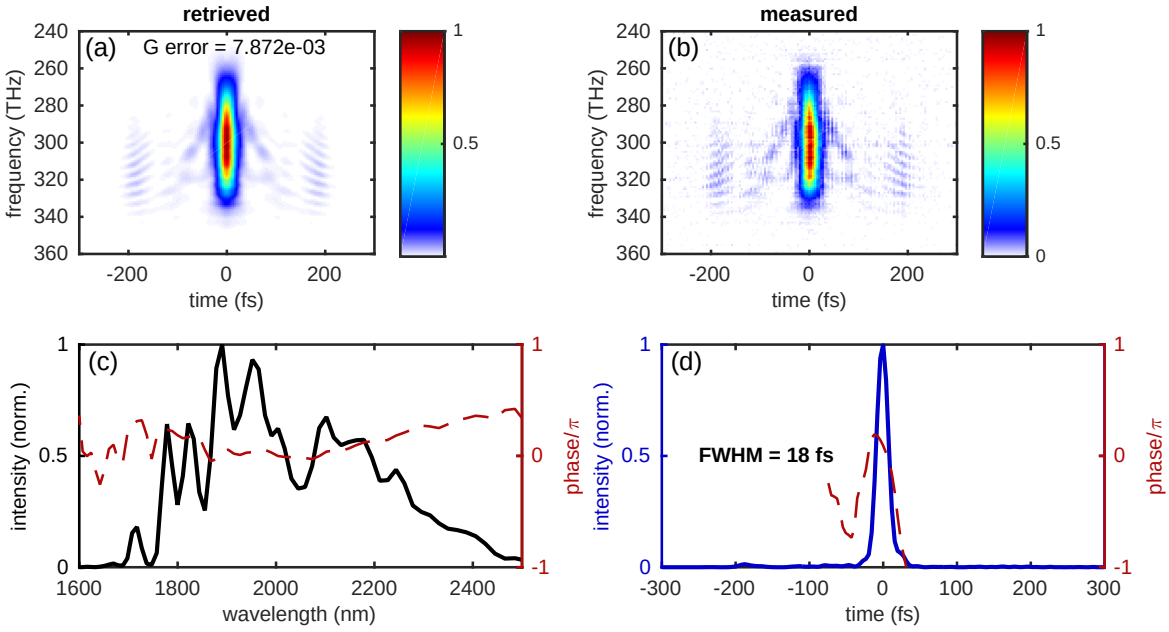

Figure 3.24: SH-FROG measurement of the 2μm pulse compressed by feedback phase in AOPDF. (a) Retrieved FROG spectrogram. (b) Measured FROG spectrogram. (c) Retrieved spectrum (black) and spectral phase (red dashed). (d) Retrieved time envelope (blue) and temporal phase (red dashed).

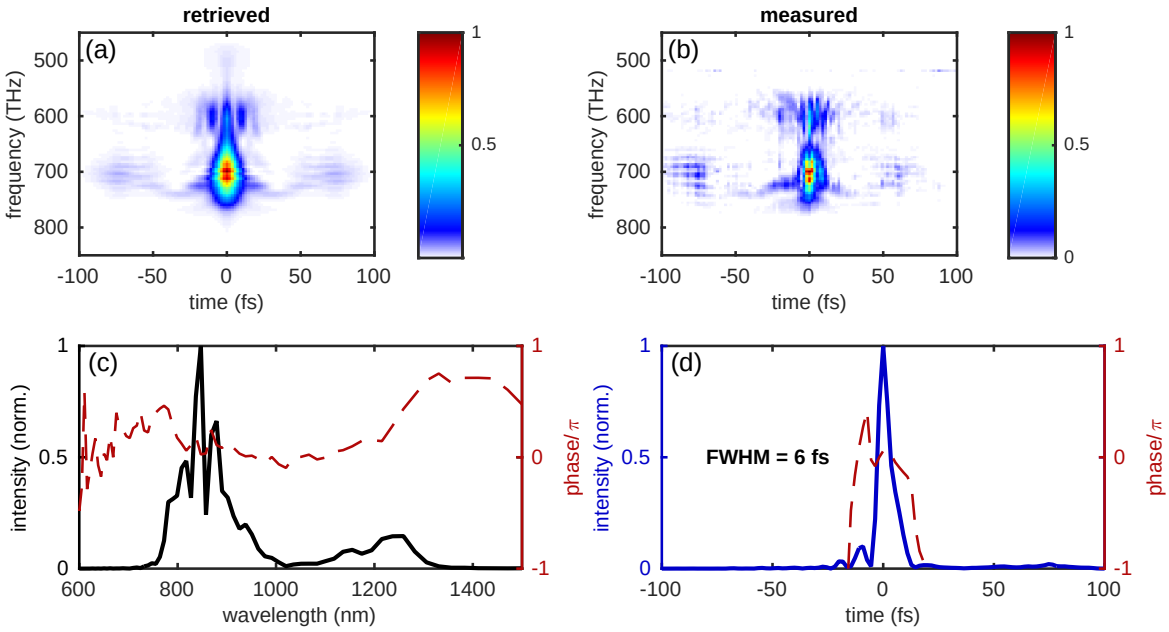

Figure 3.25: SH-FROG measurement of the 1μm pulse compressed by chirped mirrors. (a) Retrieved FROG spectrogram. (b) Measured FROG spectrogram. (c) Retrieved spectrum (black) and spectral phase (red dashed). (d) Retrieved time envelope (blue) and temporal phase (red dashed) ($G_{error} = 0.0262$). Adapted from [53].

and sent to a custom-designed chirped mirrors compressor. The residual pump was filtered from the amplified signal by a long-pass filter with a cut-off wavelength of 700 nm (Thorlabs GmbH, FEL0700). Afterward, the signal pulses containing 20 μJ of energy were compressed to 6 fs (FWHM) via 16 bounces in the chirped mirrors compressor. The residual dispersion was fine tuned by using a pair of thin fused-silica wedges. Figure 3.25 (a) and (b) show the measured and retrieved spectrograms of the compressed pulses. The retrieved temporal and spectral intensity of the compressed pulses are shown in Fig. 3.25 (c) and (d). This measurement was done by a SH-FROG containing a 10-μm-thick BBO crystal. After compression, no more transmissive optics was used in the optical path, to avoid introducing additional dispersion.

The amplified spectra of both OPCPA channels together with the seed spectrum are shown in Fig. 3.26. A bandwidth of 310 THz is covered by the amplified spectrum containing 25 μJ of total energy.

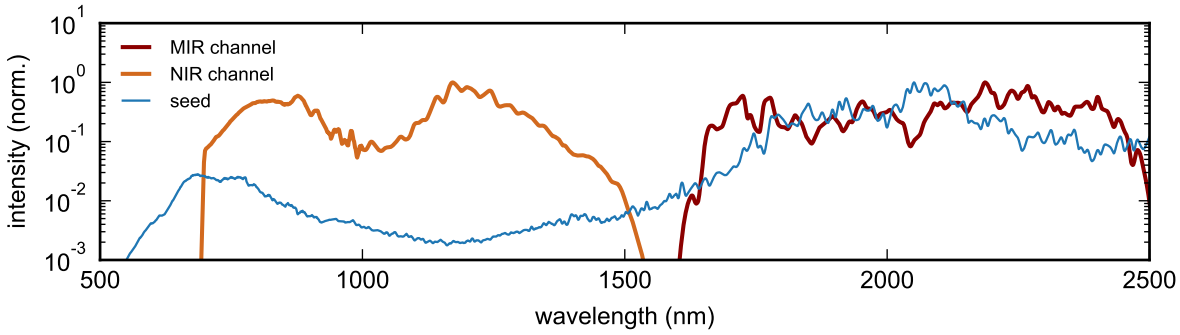

Figure 3.26: Amplified spectra in the OPCPA channels. CEP-stable, multi-octave spectrum of seed pulses (blue). Amplified spectra of 1μm near-infrared (orange) and 2μm mid-infrared (brown) OPCPA channels. Adapted from [53].

3.1.4 Energy scaling in OPCPA channels

This section presents the calculated energy for two more additional OPCPA stages in both OPCPA channels, using the remaining pump energy of the amplifier. Three-dimensional numerical simulations were performed with the SISYFOS code [174, 175]. Thermal effects, third-order nonlinear processes, and two-photon absorption were neglected in the simulation.

In the NIR spectral region, broadband amplification can be obtained in LBO crystal at a noncollinear internal angle of 1.05^o with a phase-matching angle of $\phi = 15^o$, as was used in the first OPCPA stage (section 3.1.3). The input parameters for numerical simulation of the NIR amplification stage are summarized in table 3.3. The Sellmeier coefficients for LBO crystals was obtained from Ref. [180]. The 8.3 mJ remaining energy of 515 nm pulses from the second-harmonic (SH) module was used to pump the second amplification stage. The pump beam size was adjusted to have a peak intensity of 100 GW/cm^2 at the crystal. The residual pump energy was then reused to pump the third amplification stage, with its size adjusted to have a peak intensity back to 100 GW/cm^2. The d_{eff} was taken to be 0.82,pm/V. An amplified pulse energy of 1.8 mJ was obtained. The corresponding spectrum is shown in Fig. 3.27 (a).

Commercially available PPLN crystals have limited aperture. Therefore, other crystals were studied for amplification in the MIR spectral channel. BBO, bismuth borate (BiBO) and $LiNbO_3$ are common crystals for amplification in this spectral region, and can be grown to large aperture ($>$ 20 mm diameter). BBO and BiBO have high damage threshold and support similar gain bandwidth, while BiBO offers a larger effective nonlinearity and is mechanically more robust and inert to moisture. $LiNbO_3$ supports a broader gain bandwidth and has the largest effective nonlinearity. However, the beam profile deterio-

Table 3.3: Input parameters used in the simulation of the near-infrared channel. L: crystal thickness, E_p: input pump energy, E_s: amplified signal energy, ω_p: pump beam radius (FWHM), ω_s: signal beam radius (FWHM). Adapted from [53].

stage	L (mm)	E_p (mJ)	E_s (mJ)	ω_p (mm)	ω_s (mm)	efficiency (%)
2^{nd}	2.5	8.3	1.3	1.46	1.16	15.1
3^{rd}	1.0	6.0	1.8	1.28	1.02	9.8

Table 3.4: Input parameters used in the simulation of the mid-infrared channel. L: crystal thickness, E_p: input pump energy, E_s: amplified signal energy, ω_p: pump beam radius (FWHM), ω_s: signal beam radius (FWHM). Adapted from [53].

stage	L (mm)	E_p (mJ)	E_s (mJ)	ω_p (mm)	ω_s (mm)	efficiency (%)
2^{nd}	2.0	8.9	1.3	1.63	1.50	14.9
3^{rd}	1.0	6.2	2.2	1.42	1.34	13.9

ration caused by photorefractive effect limits the pump intensity that can be applied. In the following simulation, $LiNbO_3$ was chosen to be the amplification gain medium because of its large effective nonlinearity and broader gain bandwidth. Broadband amplification of seed pulses centered at 2 μm can be phase matched at $\theta = 42.9^o$. The input parameters for numerical simulation of the MIR amplification stage are summarized in table 3.4. The 8.9 mJ remaining energy of 1030 nm pulses from the SH module was used to pump the second amplification stage. Its beam size was adjusted to have a peak intensity of 65 GW/cm^2 at the crystal. The residual pump energy was again reused to pump the third amplification stage with its size adjusted to have a peak intensity back to 65 GW/cm^2. $d_{eff} = 3.96$ pm/V is assumed. Amplified pulse with 2.2 mJ energy was obtained and the corresponding spectrum is shown in Fig. 3.27 (b).

3.1.5 Temporal jitter analysis

Coherent superposition of the amplified MIR and NIR few-cycle pulses using a broadband dielectric beam combiner results in the generation of light transients. Different relative temporal overlaps between the few-cycle pulses can lead to various light transients [23]. Therefore, the stability of the generated light transients rely on the relative phase and timing stability between the two OPCPA channels of the synthesizer [79]. Since OPCPA preserves the CEP stability of the seed, the stability of the absolute phase from both OPCPA channel is ensured. Besides, the direct multi-octave SC generation from the pump amplifier guarantees an intrinsic temporal synchronization of pump and seed pulses in

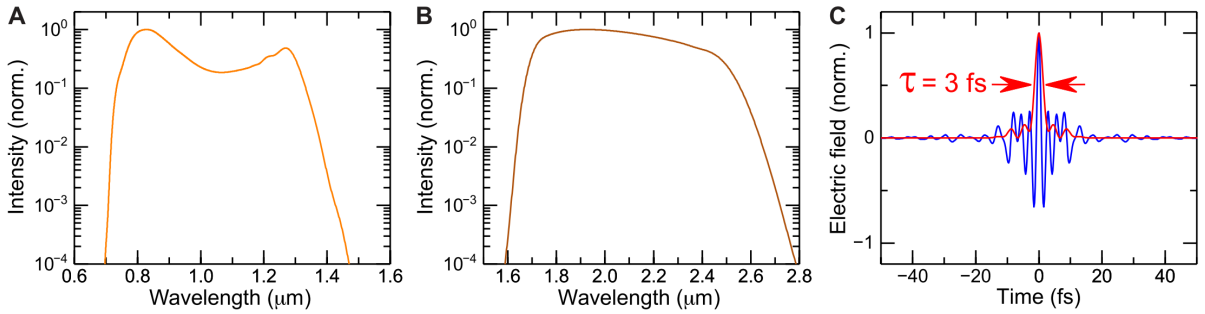

Figure 3.27: The simulated amplified spectra in (a) near-infrared and (b) mid-infrared channels with 1.8 mJ and 2.2 mJ of energy, respectively. (c) The calculated synthesized waveform. Adapted from [53].

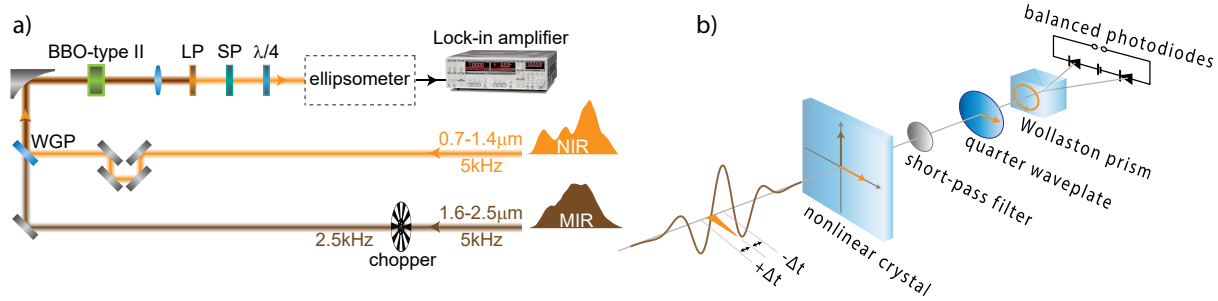

Figure 3.28: (a) Schematic of the EOS setup. WGP: wire grid polarizer, LP: long-pass filter, SP: short-pass filter, $\lambda/4$: quarter-wave plate. (b) Concept of EOS. The MIR pulses chopped at 2.5 kHz and the near-infrared (NIR) probe pulses are collinearly combined and focused into a 50 μm-thick BBO crystal for detection. The sum-frequency of the two pulses overlaps and interferes with the high-frequency components of the probe pulse. The EOS signal can be enhanced using proper spectral filtering. Afterward, an ellipsometer consisting of a quarter-wave plate and a Wollaston prism is used to detect the polarization rotation as a function of time delay. Adapted from [53].

OPCPA stages. Moreover, the seed pulse duration is kept shorter than the pump pulse duration in OPCPA stages, such to avoid any temporal instability caused by the temporal fluctuations in the arrival time of pump pulses. The temporal jitter is therefore only restricted to long-term drifts originated from the optical path of the synthesizer.

To confirm the temporal stability between the two OPCPA channels, an EOS measurement was performed [142]. In this measurement, the electric field of the MIR pulses is resolved by 6-fs NIR probe pulses. In order to resolve the fast oscillating electric field of the MIR pulses, the probe pulses are required to have a temporal jitter less than half-cycle duration of the MIR pulses over the whole scanning range.

The setup of the EOS is illustrated in Fig. 3.28 (a). The amplified pulses centered at 2 μm (brown color) from section 3.1.3 were mechanically chopped (Thorlabs GmbH, MC2000B-EC) with a frequency of 2.5 kHz for lock-in detection, while the amplified pulses centered at 1 μm (orange color) from section 3.1.3 sent through a mechanical delay stage (Physik Instrumente Ltd., V-528.1AA) to be used as a gate pulse. Pulses from two arms were orthogonally polarized and overlapped by an ultra-broadband wire grid polarizer (Thorlabs GmbH, WP25L-UB) and then focused colinearly into a 50 μm-thick BBO crystal (CASTECH Inc., type-II, cut at $\theta = 25°$) by an off-axis parabolic mirror with 2 inch focal length. A detailed illustration of the nonlinear crystal and ellipsometer in the EOS setup is shown in Fig. 3.28 (b). The orthogonally polarized NIR and MIR pulses are aligned along the ordinary (o) and extraordinary (e) axes of the nonlinear crystal, respectively. When the two pulses were temporally overlapped in the crystal, a sum-frequency signal at 670 nm with a polarization perpendicular to the NIR gate pulse was generated. Interference of the converted sum-frequency pulse and the gate pulse results in a modified polarization in the overlapped spectral region.

The resulted polarization rotation was analyzed by an ellipsometer consisting of a quarter-wave plate (Thorlabs GmbH, AQWP05M-600) and a Wollaston prism (Thorlabs GmbH, WP10). The ellipsometer splits the NIR gate power equally to two identical photodiodes of a home-built balanced detector in the absence of 2 μm MIR field. In the presence of 2 μm MIR pulses, polarization rotation will cause an imbalance and photocurrent is recorded in the balanced detector. Using a lock-in amplifier to record the photocurrent of balanced detector as a function of the temporal delay between the NIR and MIR pulses results in a signal that is directly proportional to the MIR electric field.

For enhancing the detection sensitivity, the spectral components between 650 and 750 nm was selected, using a long-pass filter with a cut-on wavelength of 650 nm (Thorlabs GmbH, FEL0650) in combination with a short-pass filter with a cut-off wavelength of 750 nm (Edmund Optics Ltd., 64-324) [181].

To improve the precision of the delay scan, a 1.55 μm CW laser from a delay tracking device (SmarAct GmbH, PicoScale) was sent through both MIR and NIR beam paths and then recombined and sent back to the delay tracking device. Such Mach-Zehnder-type

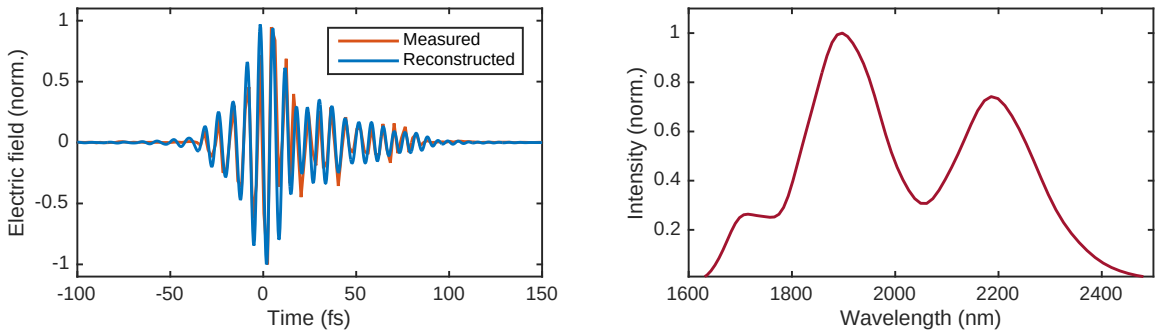

Figure 3.29: Electro-optic sampling of the 2 μm pulses. (a) Measured and reconstructed electric field of the compressed few-cycle 2 μm pulse versus delay. (b) Fourier transform spectrum of the measured waveform shown in (a).

interferometric delay tracking provides a precise temporal delay reference [182].

In the EOS measurement of the MIR pulses, the delay stage was scanned for 300 μm with a speed of 1.7 μm/s. This scanning speed with a lock-in modulation at 2.5 kHz corresponds to only one pulse to be detected at each delay position. The measured and reconstructed electric field of the MIR pulses is shown in Fig. 3.29 (a). The corresponding spectrum obtained by Fourier transform of the measured temporal waveform is plotted in Fig. 3.29 (b). Resolving the electric field of the MIR pulses with sub-cycle precision without active stabilization demonstrates a good short-term spatial and temporal stability of the synthesizer.

In order to check the temporal jitter in a longer time scale of picosecond, an experiment is designed. When broadband ultrashort pulses interact with molecules, photons at resonance frequencies are slowed down as a result of an increased group refractive index, and appear at the tail of the excitation pulse. This delayed reaction of the sample is known as FID [183], which carries information about molecular composition and concentration. Such delayed reaction can last for several picoseconds in liquid-phase and up to hundreds of picoseconds in gas-phase. Therefore, we chose to detect this signal, in order to verify the stability of the system for longer time scale (ps).

Water was chosen due to its strong v_2+v_3 combination band near 1930 nm (5180 cm^{-1}), which falls within the spectral range of the few-cycle pulses centered at 2 μm.

The setup for characterising the temporal stability of the synthesizer at longer time scale is illustrated in Fig. 3.30 (a). Based on the EOS setup in Fig. 3.28 and with some modifications, the 18 fs few-cycle pulses centered at 2 μm (described in Sec. 3.1.3) were first used to excite water molecules placed in between two off-axis parabolic mirrors with a focal length of 4 inch. Afterward, the transmitted 2 μm pulses with molecular response information in the FID, were overlapped and sampled by few-cycle pulses centered at 1 μm

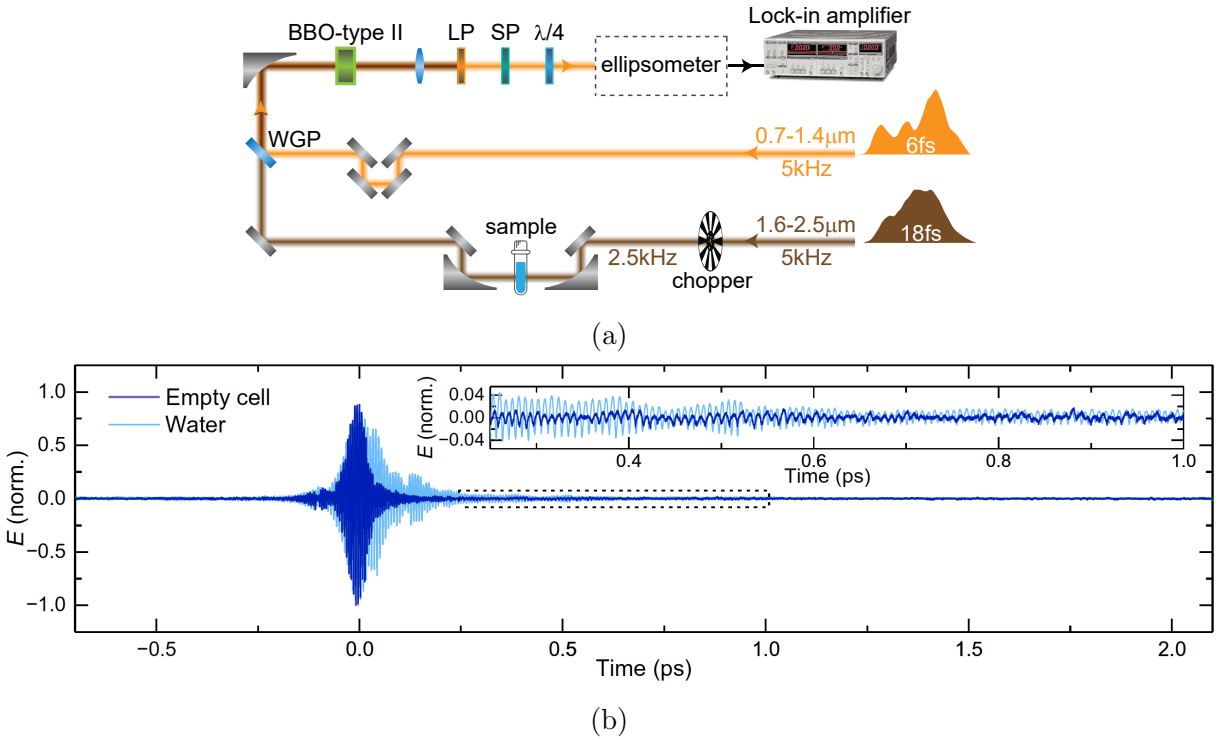

Figure 3.30: (a) Direct electric field detection of the free-induction decay of water molecules. WGP: wire grid polarizer, LP: long-pass filter, SP: short-pass filter, $\lambda/4$: quarter-wave plate. (b) Measured electric field of the MIR pulses in the absence (dark blue curve) and presence of water (light blue curve). Adapted from [53].

in the EOS setup.

Figure 3.30 (b) shows the measured electric field of the MIR pulses in the absence (dark blue curve) and presence (light blue curve) of water. To probe the MIR pulses, the delay stage was scanned for 450 μm with a speed of 1.7 μm/s. As shown in Figure 3.30 (b), in the absence of water, the amplitude of the excitation pulses goes to zero at temporal delays above 200 fs. After the injection of water, the transmitted excitation pulse is temporally chirped and the molecular FID is formed.

Resolving the electric field of the MIR pulses with sub-cycle precision over a 3-ps time window and in the absence of active stabilization demonstrates the spatial and temporal stability of the synthesizer. The residual long-term drifts caused by thermal effect which degrades the stability of synthesizer can be compensated by active optical synchronization techniques, such as balanced optical cross-correlation (BOC) [79].

3.1.6 Field-resolved near-infrared spectroscopy

The described experiment in section 3.1.5 pave the way for field-resolved near-infrared spectroscopy [184]. Using ultrashort pulse for molecular excitation allows the detection of molecular information stored in the FID free of background, since the much longer FID become temporally separated from the excitation pulse. By employing broadband excitation pulses in combination with EOS, the entire molecular vibrations in the fingerprint region can be simultaneously excited and detected. The detection sensitivity of our setup is comparable to the conventional spectroscopy techniques and limited to the stability of the interferometer and the repetition rate of the laser [184]. Employing a frontend at megahertz repetition rates can enhance the detection sensitivity.

Moreover, combining the concept of field-resolved near-infrared spectroscopy with exciting nonlinear techniques such as two dimensional spectroscopy, holds promise to increase our understanding of molecular dynamics, for example in water. Water in liquid phase, consists of a molecular network with molecular dynamics at various time scales, from several picoseconds to tens of femtoseconds. Femtosecond field-resolved near-infrared spectroscopy is capable of detecting the complex electric field of the water response at above-mentioned time scales with high sensitivity, and may allow for resolving many unknown aspects of water's molecular dynamic.

3.2 Cross-polarized pulse synthesis

[3]The multi-channel few-cycle OPCPA-based field synthesizer described in section 3.1 provides a conceptual route for scaling the energy of light transients to the multi-terawatt

[3]This section is adapted from [22, 185].

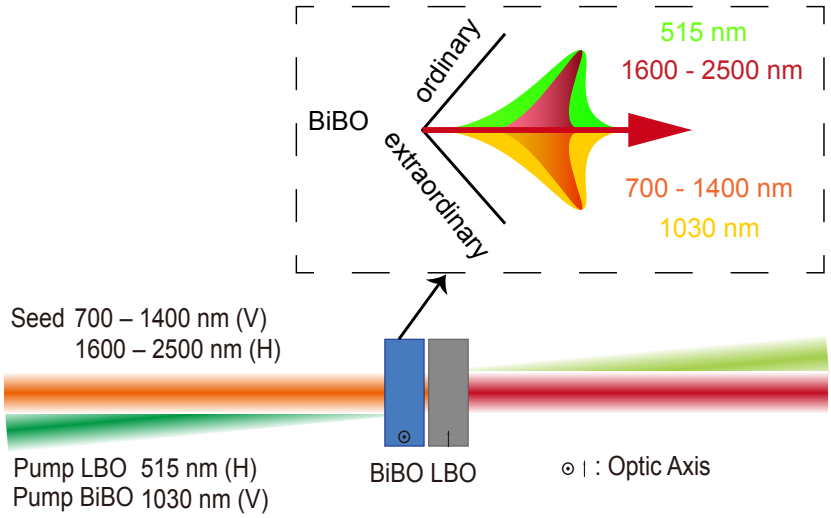

Figure 3.31: Concept of the cross-polarized OPCPA. The pump beam contains the fundamental beam at 1030 nm with a polarization in vertical (V) direction, and the second harmonic beam at 515 nm with a crossed polarization in horizontal (H) direction. The cross-polarized seed beam consists of two polarizations states: 700-1400 nm region in vertical direction (V) and 1600-2500 nm region in horizontal (H). BiBO crystal is used to amplify the long wavelength part of the seed spectrum, while LBO crystal is used for the amplification of short wavelength part. Inset illustrates how different pump and seed spectral components are distributed in different axes of the BiBO crystal. Adapted from [22] © [2019] IEEE.

regime. However, after employing additional OPCPA stages, due to the large footprint of the system, control of the temporal jitter with sub-cycle resolution becomes cumbersome. Here I propose a new scheme "cross-polarized field synthesis" to overcome these limitations, by reducing the complexity, cost, and the requirement for active synchronization.

In cross-polarized field synthesis, different OPCPA channels share the same optical beam path before the coherent synthesis. Unlike the field synthesizer described in section 3.1, here the amplification module contains nonlinear crystals for the entire bandwidth of the seed pulse. Different spectral regions of the ultra-broadband seed spectrum are distinguished by different polarization state. After amplification and temporal compression, generation of the mJ-light transients could be performed in a concept similar to [99].

Fig. 3.31 illustrates the amplification module containing two different crystals for cross-polarized field synthesis. Ultra-broadband seed pulses with an orthogonally polarized low- and high-frequency regions (see Fig. 3.35) could be amplified in such a hybrid amplification module. The amplification module contains different nonlinear crystals suitable for each frequency range and is pumped by two high-energy pulses at different frequencies with a crossed polarization. Here, the OPCPA crystals are placed within the Rayleigh length of

all the interacting beams, for efficient energy transfer from the pump to the seed pulses. In what follows, the conceptual design of such a synthesizer pumped by Yb:YAG thin-disk amplifier (3.1.1) is discussed numerically.

3.2.1 Pump module

2 mJ energy of the Yb:YAG thin-disk laser described in section 3.1.1 is separated and used for generating, CEP-stable seed generation, while the remaining 18 mJ is used for pumping the two OPCPA channels. As is shown in Fig. 3.32, the cross-polarized pump pulses are generated in a second harmonic module containing a 0.5 mm-thick type-I BBO crystal operating at 50% conversion efficiency. Due to the second order nonlinearity, the spatial profile of the generated SH beam is smaller by a factor of $\sqrt{2}$. Therefore, the two collinearly propagating pump beams are separated and recombined before entering the amplification module, to enable a full control on temporal delay and the pump intensities in the amplification module.

3.2.2 Cross-polarized supercontinuum generation

Super-octave spectrum is generated due to the interplay between dispersion, nonlinearity and propagation effects, when intense ultrashort pulses interect with matter. It has been shown, filament-free super-octave pulses with cross-polarization can be generated by harvesting cascaded quadratic nonlinearity at ZDW in material [185]. Here, lower peak intensity is required to trigger the process and the generated super-octave spectrum is ideal to seed cross-polarized synthesizer.

In the following, quadratic cascaded SC generation in a $LiNbO_3$ crystal pumped at its ZDW is discussed theoretically and demonstrated experimentally. This case is compared to quadratic cascaded SC generation in BBO crystal [186, 187], and Kerr-nonlinearity driven SC in YAG plate in anomalous dispersion regime.

Cascaded quadratic nonlinearity In a nonlinear medium with second order nonlinerarities and at large phase mismatch and ΔkL, a small portion of the fundamental wave (FW) is converted to the SH waves in one coherence length and then converted back to the FW in another coherence length. The phase shift between the unconverted and back converted FW induces a Kerr-like nonlinearity, known as cascaded quadratic nonlinearity. Changing the magnitude and sign of the nonlinearity can give rise to self-focusing or self-defocusing [188–190]. The cascaded quadratic nonlinearity could increase the effective nonlinear refractive index, which in turn reduces the peak intensity threshold of SC generation to below the critical power [191].

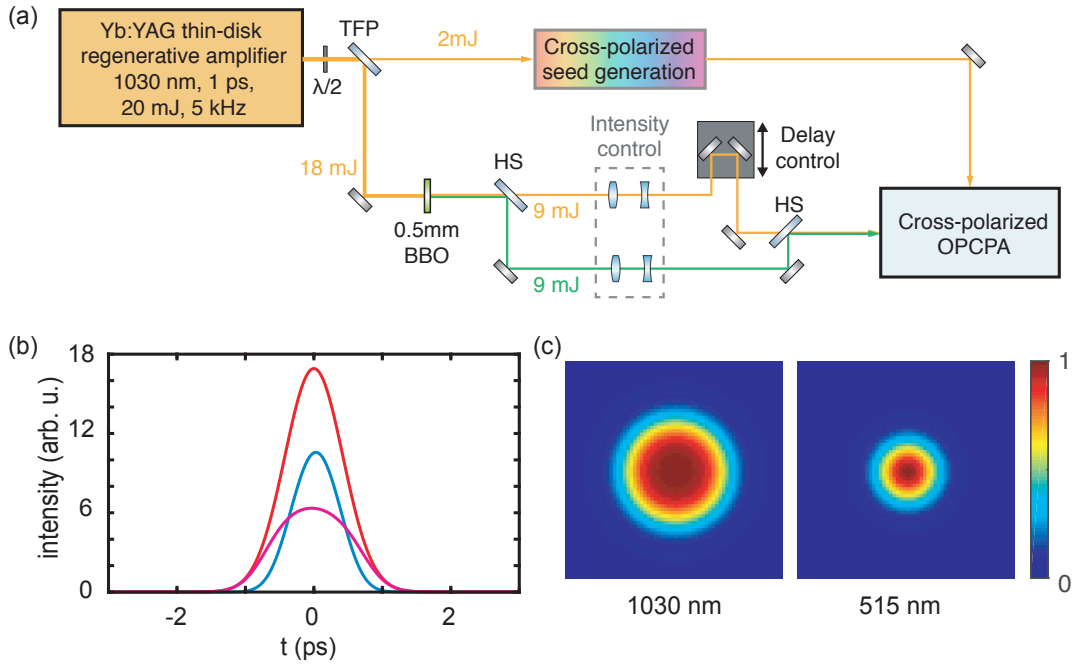

Figure 3.32: (a) Schematic setup of the cross-polarized pump module. TFP: thin film polarizer; HS: harmonic separator. (b) The simulated temporal profile of: (i) the input pulse before the second harmonic module at 1030 nm with the pulse duration of τ_{FWHM}=1 ps (red curve), (ii) the residual of the input pulse after the second harmonic generation at 1030 nm and τ_{FWHM}=1.4 ps (magenta curve), and (iii) the generated second harmonic pulse at 515 nm and τ_{FWHM}=0.83 ps (blue curve). (c) The simulated spatial profile of the residual of the input beam after the second harmonic generation at 1030 nm (left) and the generated second harmonic beam at 515 nm (right). Adapted from [22] © [2019] IEEE.

BBO and $LiNbO_3$ crystals were chosen for this study, as they have similar structure (Trigonal, R3c) but different ZDW (1.4 μm for BBO and 2 μm for $LiNbO_3$). The FW is considered to be ordinary polarized few-cycle pulses centered at 2.1 μm in quadratic, type I interaction ($o + o \rightarrow e$). In the strongly phase mismatched regime, apart from the Kerr nonlinear refractive index (n_2^{Kerr}), there is a cascaded nonlinear refractive index (n_2^{casc}) induced to the FW, which can be calculated from:

$$n_2^{casc} = -\frac{4\pi d_{eff}^2}{\Delta k n_o(2\omega) n_o(\omega)^2 \lambda_0 \epsilon_0 c} \tag{3.1}$$

where $\Delta k = k(\lambda_0/2) - 2k(\lambda_0)$, $k = \frac{2\pi n}{\lambda_0}$, and λ_0, ϵ_0, n_o represent the central wavelength, vacuum permittivity and ordinary refractive index of the nonlinear medium. The sum of the n_2^{casc} and the n_2^{Kerr} leads to an effective nonlinear index n_2^{eff}. The input parameters for the following estimations are summarized in table 3.5.

Table 3.5: Parameters used for the calculation of the effective nonlinear indices of different crystals. Adapted from [185].

Crystal	λ (μm)	nonlinear coefficients (pm/V)	$n_2^{Kerr} \times 10^{-16}$(cm^2/W)
YAG	2.1	isotropic	6.9
BBO	2.1	d_{22}= 2.2 / d_{31} = 0.04	o-axis = 5.61, e-axis = 2.34 [192]
$LiNbO_3$	2.1	d_{22}= 2.6 / d_{31} = 4.6	o-axis = 20.7, e-axis = 16.5 [193]

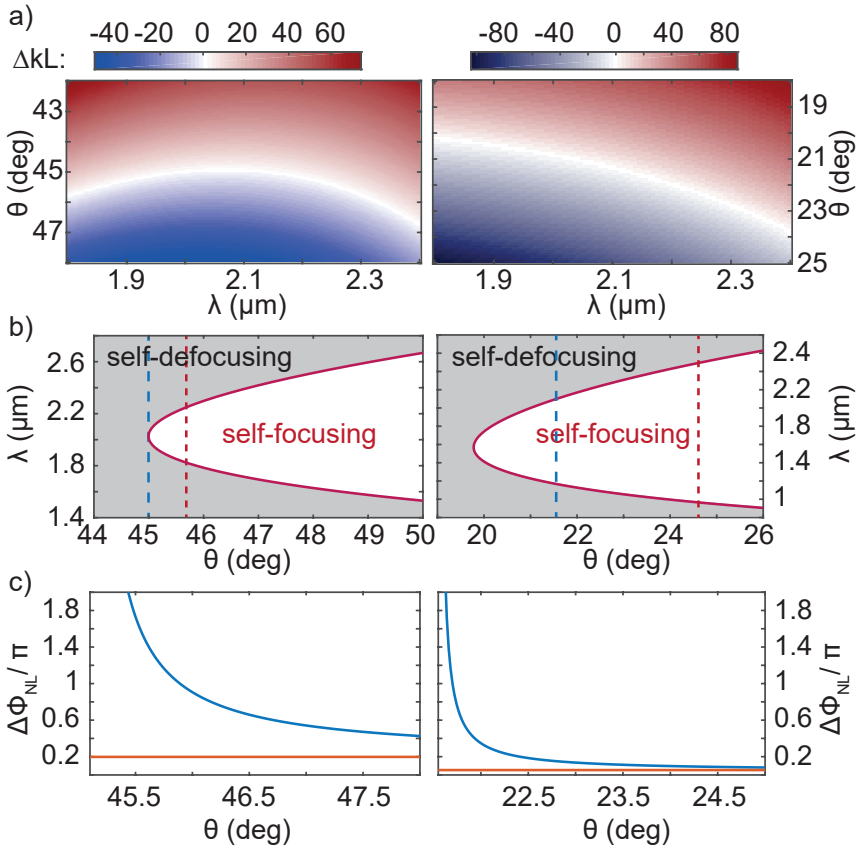

Figure 3.33: (a) Calculated ΔkL versus wavelength and phase matching angle for a 2-mm-thick $LiNbO_3$ crystal (left) and a 2-mm-thick BBO crystal (right). (b) Type-I phase matching curves in $LiNbO_3$ (left) and BBO (right). The blue dashed line indicates the phase matching angle for second harmonic generation and the red dashed line indicates the angle of operation for SC generation. The gray-shaded area indicates where n_2^{casc} is negative. (c) The calculated nonlinear phase-shift for a 2-mm-thick $LiNbO_3$ (left) and 2-mm-thick BBO (right) crystal. The red line indicates the phase-shift induced by the Kerr nonlinearity. Adapted with permission from [185] © The Optical Society.

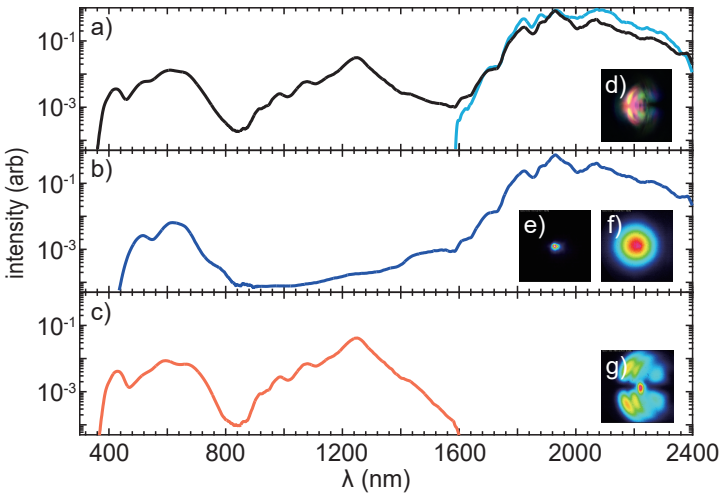

Figure 3.34: (a) Measured spectrum of the fundamental (blue curve) and the generated SC (black curve) in a 2-mm-thick BBO crystal. (b) The ordinary polarization part of the spectrum measured after an ultra-broadband wire grid polarizer. (c) The measured extraordinary polarization part of the spectrum. Insets: The picture of generated SC (d). Beam profile of the spectral components below 1 μm of the shown spectrum in the far-field (e) and the near-field (f) and (g). Adapted with permission from [185] © The Optical Society.

The dispersion and the induced nonlinear phase shift of both crystals with 2 mm thickness are compared in Fig. 3.33. For 2.1 μm pulses, the phase mismatch becomes zero at $\theta = 45.05^o$ for $LiNbO_3$ and at $\theta = 21.5^o$ for BBO, as shown in Fig. 3.33 (a). When the phase matching angle of BBO is tuned to $\theta = 24.7^o$, the group velocity dispersion (GVD) is -157.0298 fs^2/m and the phase mismatch is -58.44, resulting in a positive effective cascaded nonlinearity. The induced cascaded quadratic nonlinearity at this angle (n_2^{casc}= 8.92 $\times 10^{-16}$ cm^2/W) is in self-focusing regime, and larger than the cubic nonlinearity of the crystal (n_2^{Kerr}= 5.61 $\times 10^{-16}$ cm^2/W). This regime enables solitary wave dynamics where the pulse experiences a strong compression as a result of high-order cubic soliton excitation and generation of linear dispersive waves at high frequencies [194]. However, for $LiNbO_3$ tuned at $\theta = 45.85^o$, the GVD is -74.8813 fs^2/m and phase mismatch is -12.28. Here, the cascaded nonlinearity (n_2^{casc}= 90.3$\times 10^{-16}$ cm^2/W) and the cubic nonlinearity values (n_2^{Kerr}= 20.7$\times 10^{-16}$ cm^2/W) are much bigger than BBO, due to a larger d_{eff} of $LiNbO_3$. Moreover, a lower GVD in $LiNbO_3$ allows for longer propagation of few-cycle pulses in the crystal with an insignificant reduction of the peak intensity.

Experiment The two regimes of quadratic SC generation described in Fig. 3.33 were experimentally studied using few-cycle, CEP-stable pulses at 2.1 μm (Fig. 3.15 and described in section 3.1.2). This wavelength corresponds to the anomalous dispersion region

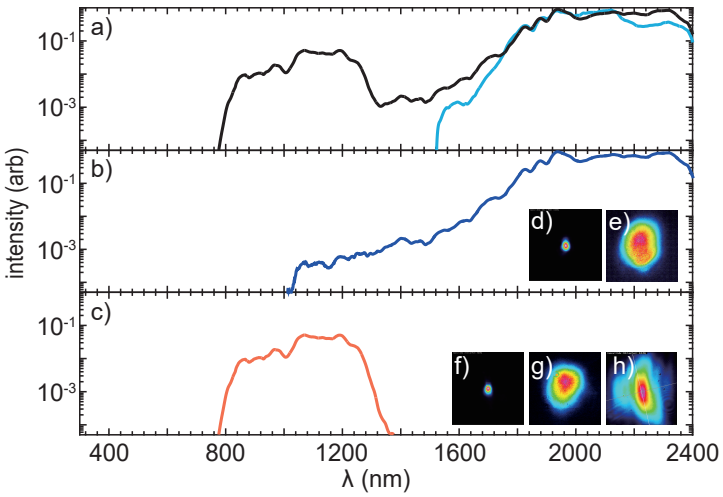

Figure 3.35: (a) Measured spectrum of the fundamental (blue curve) and the generated SC (black curve) in a 2-mm-thick $LiNbO_3$ crystal. (b) The ordinary polarization part of the spectrum measured after an ultra-broadband wire grid polarizer. (c) The measured extraordinary polarization part of the spectrum. Insets: The beam profile of the spectral components above 1 μm of the shown spectrum in the far-field (d) and the near-field (e), and below 1 μm in focusing regime in the far-field (f) and the near-field (g) and defocusing regimes in the near-field (h). Adapted with permission from [185] © The Optical Society.

and ZDW region for the BBO and $LiNbO_3$ crystals, respectively. The two crystals were mounted in a rotational mount for tuning the phase matching angle. The peak intensity was changed by scanning the crystal position towards the focus of the beam.

First the SC generation in anomalous dispersion region was studied, 2 μJ, 2.1 μm pulses were focused to a 2-mm-thick, type-I BBO crystal using a f=75 mm CaF_2 convex lens. The input polarization was set to be parallel to the ordinary axis of the crystal. The phase matching angle of the crystal was scanned and the SC with broadest spectral bandwidth and best spatial profile was selected.

The broadest generated spectrum generated at $\theta = 24.7^o$ and its corresponding spatial intensity profile is shown in Fig. 3.34 (a). An ultra-broadband wire grid polarizer (Thorlabs GmbH, WP25L-UB) was used to divide the generated SC into ordinary and extraordinary polarization components, as shown in Fig. 3.34 (b) and (c). Because of the negative ΔkL induced at $\theta = 24.7^o$, the effective nonlinear index was enhanced, which resulted in a reduced threshold power for generating a SC at a level below the critical power for self-focusing.

The spatial intensity profile in both polarizations of the generated SC was measured with a charge-coupled device (CCD) camera (Dataray Wincam) (Fig. 3.34-insets). The ordinary polarization part of the SC has a Gaussian spatial profile (Fig. 3.34 (e) (f)), which follows the properties of SC generation based on cubic nonlinearity. However, the spatial

profile of the portion with an extraordinary polarization has a complex structure (Fig. 3.34 (g)) [195]. The generated spectrum in the extraordinary polarization is related to the SH generation of the components on the ordinary polarization [191]. Two resonances at 2.4 μm and at 1 μm are indicated by the red dashed line in Fig. 3.33 (b). The SHG of the two resonances resulted in two peaks around 1.2 μm and 500 nm on the extraordinary polarization.

To investigate the SC generation at ZDW, the same driving pulses were focused into a 2-mm-thick, type-I $LiNbO_3$ crystal. The broadest spectrum spanning from 800 nm to beyond 2400 nm was generated at θ=45.85^o with a good spatial profile (Fig. 3.35 (a)). Portion of the generated SC with ordinary and extraordinary polarization and the corresponding spatial intensity profile are shown in Fig. 3.35 (b) and (c). Here the the newly generated frequencies in both polarizations possess a similar spatial profile to the FW, unlike the case for BBO.

The portion of the spectrum with ordinary polarization was extended to beyond 2.4 μm. Two resonance wavelengths at 1.8 μm and 2.2 μm (the crossing of the red dashed line and the red solid line in Fig. 3.33 (b)) define the bandwidth of the generated SH in extraordinary polarization, covering 900 nm to 1.1 μm. At θ=45.05^o and 16 GW/cm^2 peak intensity, SHG had an efficiency of 6%. By tuning to θ=45.85^o, the efficiency of SHG with similar spectral bandwidth was dropped to 0.2%. Increasing the peak intensity results in spectral broadening of FW and SH waves, due to four-wave mixing. Since the coherence length of the SH pulses is $2/\Delta k$= 325.7 μm, the Kerr-based broadening at extraordinary polarization only happened at the last half millimeter of the crystal.

We observed similar spectral broadening in self-defocusing region, when θ was tuned to 44.25^o. However, a higher peak intensity was required to generate the SC, and the spatial profile of the portion with extraordinary polarization was degraded (Fig. 3.35 (f)).

A SH-FROG containing a 100-μm-thick BBO crystal was used to characterize the temporal profile and spectral phase of the generated SC in $LiNbO_3$. The ordinary polarization part of the SC contained enough energy, it was directly sent to SH-FROG for characterization. The retrieved spectrum of the SC in MIR range (green) and the spectrum of the FW (blue), together with induced phase due to SC generation (black dotted line), are shown in the Fig. 3.36 (a). The induced phase was calculated by subtracting the retrieved spectral phase of the FW after SC generation from the retrieved spectral phase of the input pulses. To characterize the portion of the spectrum with extraordinary polarization, additional OPCPA was used to amplify the energy before frequency-resolved optical gating (FROG) measurement. The SH-FROG contained a 10-μm-thick BBO crystal. The retrieved spectral intensity and the corresponding spectral phase are shown in Fig. 3.36 (b).

In conclusion, SC with crossed polarization can be generated by utilizing the cascaded quadratic nonlinearity of birefringent nonlinear crystal at ZDW. The polarization rotation is initiated by SHG. At high peak intensities the induced nonlinear-phase mismatch, and

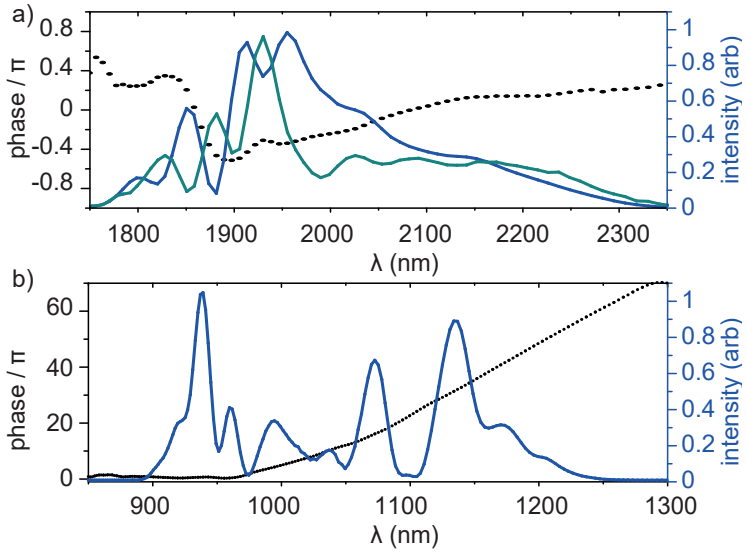

Figure 3.36: (a) Retrieved spectrum of the fundamental (blue) and the generated SC in mid-infrared spectral range after a 2-mm-thick $LiNbO_3$ crystal (cyan) measured by SH-FROG. The black dotted curve indicates the spectral phase induced by SC generation on the fundamental waves. (b) Retrieved spectral intensity (blue) and spectral phase (black dotted) of the generated SC in near-infrared spectral range after amplification. Adapted with permission from [185] © The Optical Society.

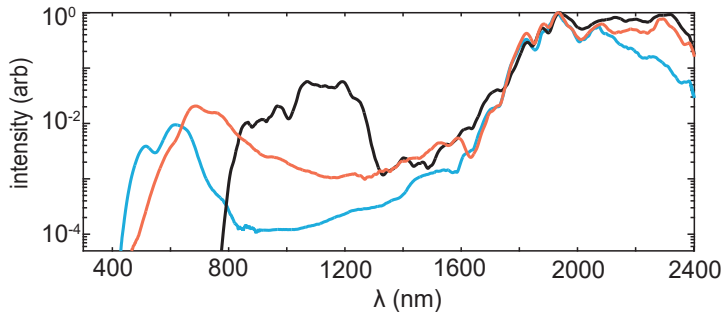

Figure 3.37: (a) Comparison of the generated SC in 2-mm-thick YAG (red), $LiNbO_3$ (black), and the ordinary polarization part of the SC in BBO (blue). Each SC spectrum is normalized to one. Adapted with permission from [185] © The Optical Society.

the self- and cross-action of the interacting FW and SH pulses lead to spectral broadening [194]. A higher SC cutoff in BBO was observed, due to its larger band gap and different dynamics in the anomalous dispersion region [196]. However, the portion of the spectrum with extraordinary polarization in BBO has a complex spatial profile.

The temporal characterizations of the generated SC in $LiNbO_3$ showed well-behaved spectral phase for both portions with ordinary and extraordinary polarization.

Fig. 3.37 compares the generated SC in $LiNbO_3$, BBO and a 2-mm-thick YAG plate under same conditions, except for the beam size on the nolinear medium. As can be noted, the newly generated frequencies in $LiNbO_3$ has an enhanced power spectral density. Moreover, the required critical power for SC generation in $LiNbO_3$ at self-focusing regime was lower by more than one order of magnitude in comparison to BBO and YAG. Different processes below and above the ZDW, for example cascaded-induced self-focusing, self-steepening, soliton and dispersive wave formation contributed to the generation of SC at ZDW.

3.2.3 Cross-polarized OPCPA

As is shown, the required ultra-broadband seed pulses with orthogonal polarization can be generated via filamentation assisted cascaded-processes (Fig. 3.35) [185]. The generated SC in $LiNbO_3$ contains spectral components from 750 to 1400 nm in one polarization, while the rest of the spectral components have orthogonal polarization.

In the following, the feasibility of amplification of such seed pulses in a cross-polarized amplification module is investigated numerically. The three-dimensional simulations were performed by SISYFOS code [174, 175].

Mid-Infrared Amplification Module BiBO crystal was chosen to amplify the MIR portion of the spectrum. BiBO is a biaxial crystal and unlike $LiNbO_3$, it has no photo-refraction, and supports a broader amplification gain bandwidth compared to BBO. Type-I phase matching for broadband amplification centered at $2\,\mu$m can be achieved in x-z principal plane, at (i) $\phi = 0^o$, $\theta = 8.0^o$ or (ii) $\phi = 0^o$, $\theta = 36.3^o$, with a noncollinear internal angle of 1.05^o. The calculated phase mismatch of two type-I interactions in BiBO is shown in Fig. 3.38 (a). It can be seen that the relative phase mismatch at $\theta = 8.0^o$ is smaller compared to $\theta = 36.3^o$. For this reason, we selected type-I, BiBO crystal with $\theta = 8.0^o$ in the following simulations.

The polarization states of the input seed and pump pulses in BiBO crystal is depicted in Fig. 3.31. The pump pulses at 1030 nm are polarized parallel to the extraordinary axis of the crystal, and the 1600 nm to 2500 nm region of the seed spectrum is parallel to ordinary axis, to fulfill the type-I phase matching condition. While the 515 nm pump pulses and 700 nm to 1400 nm region of the seed spectrum has an orthogonal polarization compared

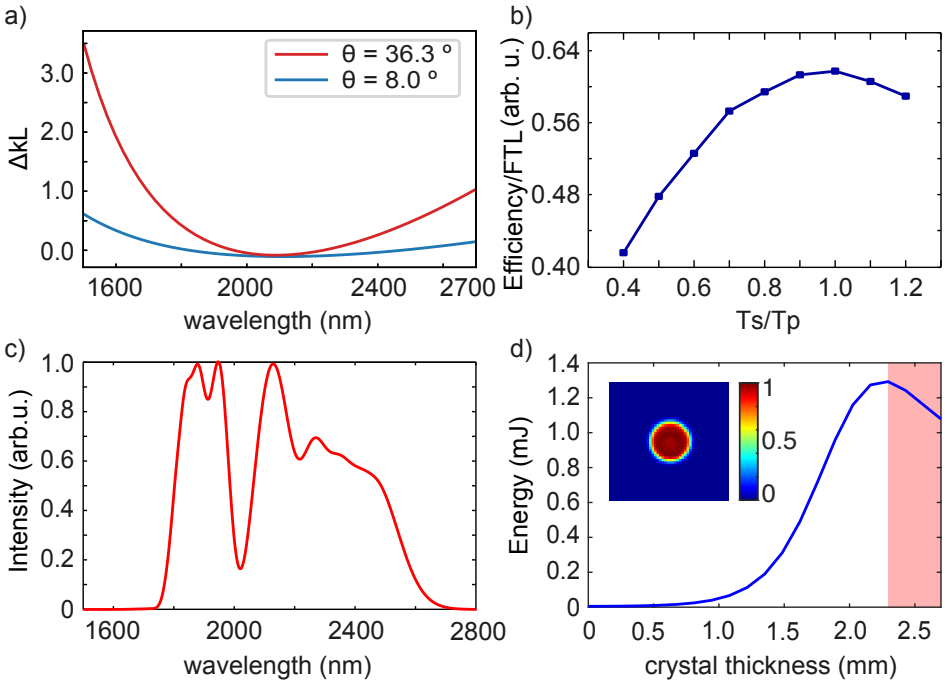

Figure 3.38: (a) Phase mismatch of type-I interaction in 3 mm BiBO pumped by 1030 nm at $\theta = 36.3^o$ (red) and $\theta = 8.0^o$ (blue). (b) The ratio between optical efficiency and FTL versus seed-to-pump temporal durations in a 2.4 mm BiBO crystal. A Gaussian temporal profile is assumed for pump pulses. (c) Simulated amplified spectrum in 2.3 mm BiBO crystal with a phase matching angle of $\theta = 8.0^o$. (d) Simulated amplified pulse energy versus crystal thickness in a 2.7 mm BiBO crystal. The quality of the amplified pulses degrade both spatially and temporally when amplification reaches the red shaded region, due to the saturation of the amplification and back conversion of the energy. Therefore, the amplification was chosen to be stopped at 2.3 mm crystal thickness. The amplified beam profile at this thickness is shown in the inset. Adapted from [22] © [2019] IEEE.

to their counterpart. Other competitive nonlinear processes which could occur besides the parametric amplification of broadband seed pulses summarized in Table 3.6. As the efficiency of these processes is very low, they were neglected in the simulation.

The relative temporal duration of pump and seed pulses and their relative timing have a vital role in the amplification process. Considering 1 ps pump pulses, the optimum relative seed-to-pump pulse durations was studied in a series of simulations. The seed pulse duration was varied between 400 fs and 1.2 ps in the MIR amplification module. For Gaussian pulses a seed-to-pump duration ratio of 1.0 results in the highest efficiency (Fig. 3.38 (b)). However, in the following simulations a seed-to-pump duration ratio of 0.65 was selected for the MIR channel, due to a slightly broader amplification bandwidth they support.

The amplified spectrum of MIR pulse in a 2.3-mm-thick BiBO is shown in Fig. 3.38

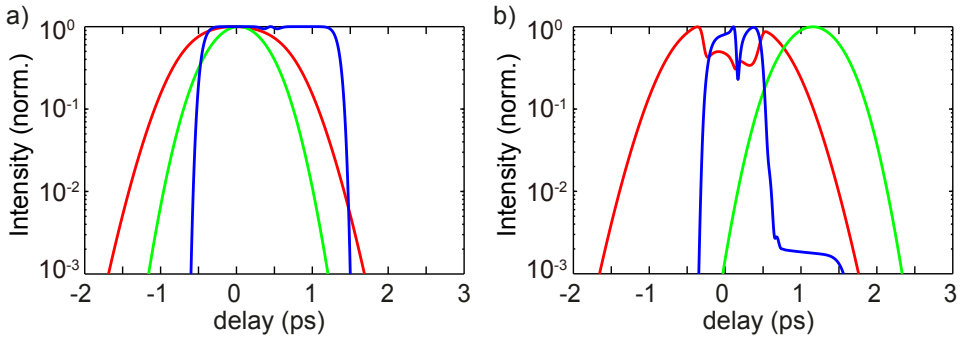

Figure 3.39: Temporal delay among the interacting pulses before and after amplification in BiBO crystal. (a) Normalized temporal profile of the 700-2500 nm seed (blue), 1030 nm (red) and 515 nm (green) pump pulses before the amplification in the simulation. (b) Normalized temporal profile of the amplified 700-2500 nm seed (blue), 1030 nm (red) and 515 nm (green) pump pulses after amplification in BiBO crystal. The energy of 1750 to 2500 nm portion of the seed is amplified, while the pump pulse at 515 nm is delayed and overlapped with the latter half of the seed. Adapted from [22] © [2019] IEEE.

Table 3.6: Possible nonlinear processes beside the parametric amplification in BiBO close to $\theta = 8.0^o$. Parameters in bold indicate the spectral components come from the input pulse. Adapted from [22] © [2019] IEEE.

θ (degree)	Interaction	Type	wavelength (nm)
10.6	DFG	I (oo-e)	**2500.0 (o)** + *972.2* (o) = **700.0 (e)**
9.8	DFG	I (oo-e)	**1600.0 (o)** + *1244.4* (o) = **700.0 (e)**
8.5	SFG	I (oo-e)	**2500.0 (o)** + **1600.0 (o)** = *975.6* (e)

(c). 1.3 mJ of amplified pulse energy with a conversion efficiency of 14.5% was obtained. To avoid excessive back-conversion from idler and signal to the pump, the amplification was stopped at 2.3 mm crystal thickness (Fig. 3.38 (d)). Table 3.7 summarizes the input parameters used for the numerical simulation. The beam size of the pump was adjusted to reach a peak intensity of 100 GW/cm^2 at the BiBO crystal.

After propagation in BiBO crystal, the pump pulses centered at 515 nm are delayed by 1.15 ps compared to their counterpart at 1030 nm, and are temporally overlapped with the NIR spectral region of the input seed pulses (Fig. 3.39).

Near-Infrared Amplification Module To amplify the NIR portion of the seed spectrum, LBO crystal offers a broad amplification gain at a phase-matching angle of $\phi = 15^o$ at noncollinear internal angle of 1.05^o. As the crystal at this angle is also phase matched for second harmonic generation at 1030 nm, we chose to place LBO crystal after the BiBO crystal. Table 3.8 summarizes the input parameters for numerical simulation of the NIR

Table 3.7: Input parameters used in the simulation of the MIR amplification stage. L_c: crystal length, d_{eff}: effective nonlinearity, α: noncollinear internal angle, E_p: pump pulse energy, E_s: seed pulse energy, ϕ_p: pump beam diameter (FWHM), ϕ_s: seed beam diameter (FWHM). Adapted from [22] © [2019] IEEE.

Crystal	L_c (mm)	θ (degree)	ϕ (degree)	d_{eff} (pm/V)
BiBO	2.3	8	0	2.04
α (degree)	E_p (mJ)	E_s (mJ)	ϕ_p (mm)	ϕ_s (mm)
1.05	9	0.005	2.29	2.4

Table 3.8: Input parameters used in the simulation of the NIR amplification stage. L_c: crystal length, d_{eff}: effective nonlinearity, α: noncollinear internal seed-pump angle, E_p: pump pulse energy, E_s: seed pulse energy, ϕ_p: pump beam diameter (FWHM), ϕ_s: seed beam diameter (FWHM). Adapted from [22] © [2019] IEEE.

Crystal	L_c (mm)	θ (degree)	ϕ (degree)	d_{eff} (pm/V)
LBO	3	90	15	0.819
α (degree)	E_p (mJ)	E_s (mJ)	ϕ_p (mm)	ϕ_s (mm)
1.05	9	0.005	3.05	2.4

amplification stage. The beam size of 515 nm pump was adapted to have a peak intensity of 100 GW/cm^2 at the crystal.

The spectrum and the amplified energy versus crystal length in a 3-mm-thick LBO crystal is shown in Fig. 3.40 (a) and (b), The amplified pulse energy of 1.1 mJ with a conversion efficiency of 12.3% was obtained. As the NIR spectral region becomes temporally separated from the 1030 nm pump pulses (Fig. 3.39 (b)), the only significant parasitic process is the SHG of the amplified seed pulses in the NIR amplification module, which was considered in the simulation.

After amplification module, the high energy signal pulses can be separated by their polarization state, compressed individually to the Fourier limit of each channel, and recombined with a dichroic mirror. The simulated total amplified spectrum after BiBO and LBO crystals is shown in Fig. 3.40 (c). The calculated mJ-level light transient obtained from this scheme is shown in Fig. 3.40 (d).

3.3 Conclusion

In this chapter two techniques for field synthesis and high energy light transients generation were presented. In the first approach, a prototype Yb:YAG-pumped OPCPA-based parallel field synthesizer was demonstrated. The system delivers 6 fs 20 μJ pulses at 1 μm and

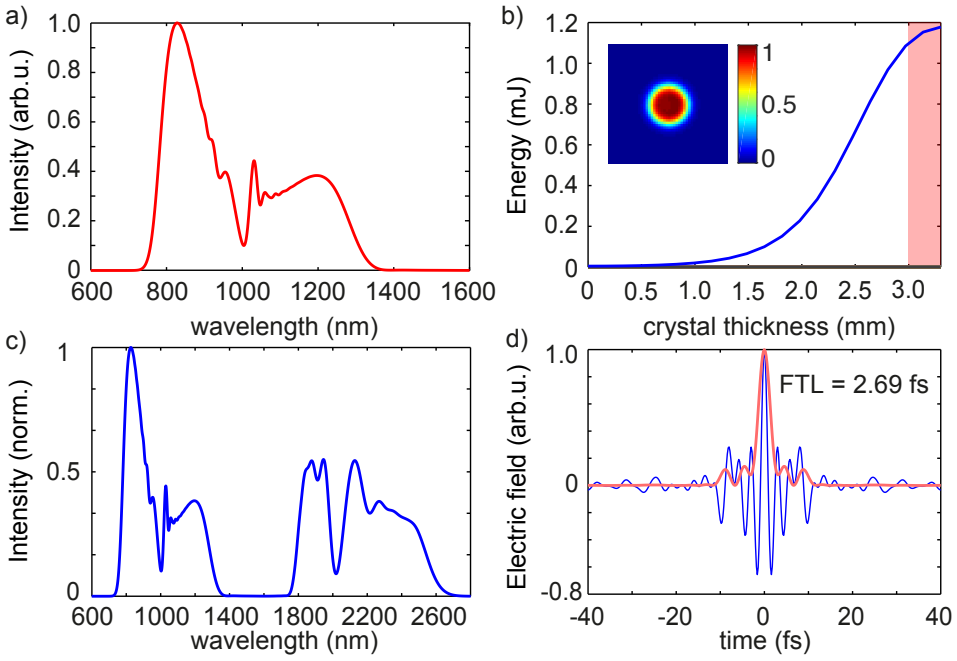

Figure 3.40: (a) Simulated amplified spectrum in 3 mm LBO crystal. (b) Simulated amplified pulse energy versus crystal thickness in a 3.3 mm LBO crystal. The quality of the amplified pulses degrade both spatially and temporally when amplification reaches the red shaded region, due to the saturation of the amplification and back conversion of the energy. Therefore, the amplification was stopped at 2.3 mm crystal thickness. The amplified beam profile at this thickness is shown in the inset. (c) Simulated total amplified spectrum after BiBO and LBO crystals. The shown spectrum are normalized to the relative amplified energy of each stage. (d) The temporal electric field (blue) and its temporal intensity (red) calculated from the total amplified spectrum shown in (c). The amplified spectrum shown in (c) has a Fourier transform limit of 2.69 fs. Adapted from [22] © [2019] IEEE.

18 fs 5 μJ pulses at 2 μm. By employing EOS the short-term temporal stability of the synthesizer at sub-cycle resolution was verified. However, due to the large footprint of such a system, additional control of the temporal jitter to reach long-term stability with sub-cycle resolution is required. Therefore, a second approach based on cross-polarized field synthesis was presented. Here different spectral regions are not spatially separated, rather distinguished by their state of polarization in different OPCPA crystals. SC seed with orthogonal polarization was generated by utilizing the cascaded quadratic nonlinearity of birefringent nonlinear crystal at ZDW. The design of a mJ-level serial multi-channel OPCPA chain was numerically studied. With a common beam path for both spectral regions, cross-polarized synthesizer holds promise to enhance the stability of the system and reduce the size, complexity, and temporal jitter of the system.

Chapter 4

High-Power, Multi-Octave Source

In the previous chapter, NIR field-resolved spectroscopy was introduced, which holds promise to mitigate the constrains of conventional spectroscopy techniques in frequency domain, such as low detection sensitivity and dynamic range. The proof of principle experiment discussed in section 3.1.6, was performed at kHz repetition rate, resulting in low signal-to-noise ratio (SNR) and long data acquisition time. NIR field-resolved spectroscopy would greatly benefit from the availability of a source with higher repetition rate. Therefore, novel, intense, broadband sources operating ideally at the MHz regime, is required to decrease the measurements acquisition time, and to enable resolving signals which stayed below the noise floor of previous experiment.

Moreover, coherent MIR and THz radiation have various applications in fundamental science, life science and also industrial processes. MIR spectral region between 2 μm and 20 μm covers fundamental modes of atomic vibrations in molecules (molecular fingerprint region). While a simultaneous coverage of this range allows for parallel detection of different molecular compositions. Due to the lack of broadband MIR laser gain media, coherent broadband MIR sources mostly utilize nonlinear downconversion of matured high-power ultrashort laser sources in visible or NIR spectral region.

This chapter describes the efforts on generation of broadband pulses from visible (VIS) to THz, driven by a high-power Kerr-lens mode-locked Yb:YAG thin-disk oscillator at multi-MHz repetition rate [26]. To extend the spectral bandwidth of the oscillator's output in NIR spectral range, three external nonlinear spectral broadening stages based on spectral broadening in bulk [40] and gas filled single-ring hollow-core photonic-crystal fiber (SR-PCF) were developed [40, 41]. Thereafter, the generated short pulses in NIR were employed to generate broadband pulses in MIR and THz spectral range via down conversion (Fig. 4.1).

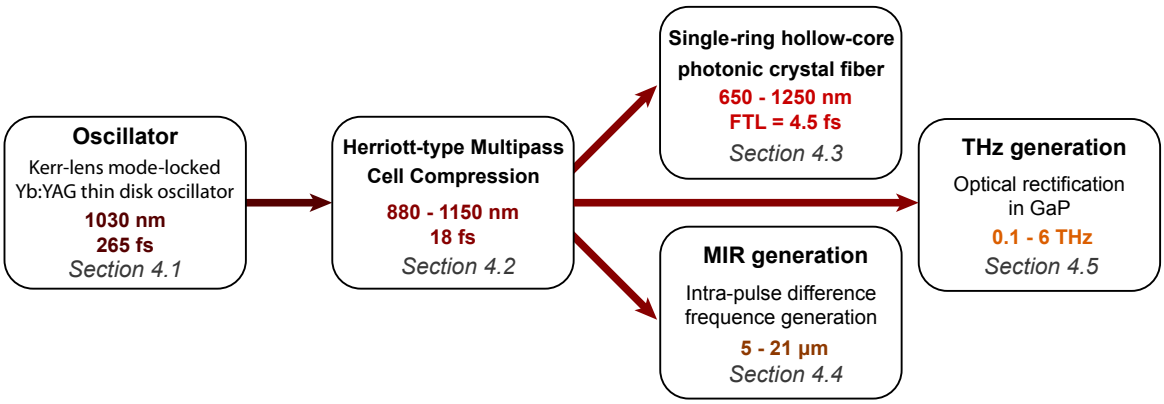

Figure 4.1: Schematic of the multi-MHz system based on a high-power Kerr-lens mode-locked Yb:YAG thin-disk oscillator. The frontend is a 16 MHz high-power Kerr-lens mode-locked Yb:YAG thin-disk oscillator delivering 265 fs (FTL = 140 fs) pulse at 1030 nm with 100 W average power (Section 4.1). The oscillator's output in NIR spectral range is compressed in two consecutive Herriott-type multipass cell to 18 fs (Section 4.2). External nonlinear spectral broadening based on gas filled single-ring hollow-core photonic crystal fiber (SR-PCF) extend the spectral bandwidth towards single cycle regime (Section 4.3). Using the 18 fs pulse obtained from the second Herriott-type multipass cell, extension towards MIR (Section 4.4) and THz (Section 4.5) range are investigated.

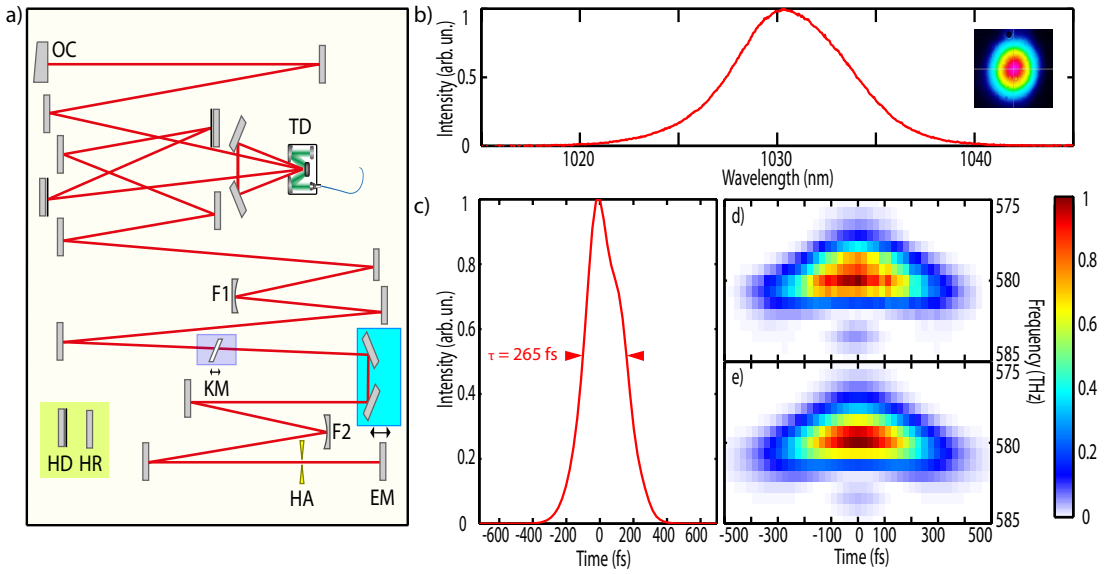

Figure 4.2: (a) Schematic of the KLM thin-disk oscillator cavity. OC: output coupler; TD: thin-disk with pump optics; F1 and F2: concave focusing mirror; KM: Kerr medium; HA: hard aperture; EM: end mirror; HD: highly dispersive mirror; HR: highly reflective mirror. (b) The measured output spectrum. Inset: output beam profile measured by a CCD beam profiler. (c) The retrieved pulse shape from FROG measurement. (d) The measured and (e) retrieved FROG traces [40].

4.1 Yb:YAG thin-disk oscillator

A Kerr-lens mode-locked Yb:YAG thin-disk (TD) oscillator served as the frontend of the system [26]. Kerr-lens mode-locking was enabled by a 6 mm-thick crystalline quartz plate placed at the focus of the cavity. The oscillator housing was evacuated to 160 mbar residual air pressure. The KLM TD oscillator delivers 1030 nm, 265 fs pulses with 100 W average power, corresponding to 6.2 μJ pulse energy at a repetition rate of 16 MHz. Fig. 4.2 shows the layout of the KLM thin-disk laser cavity, the spectrum, the retrieved pulse, and the measured and retrieved FROG spectrograms.

4.2 Multi-pass bulk compression

[1]Interaction between intense laser pulses and materials with cubic nonlinearity results in SPM and generation of new frequency components. However, the uneven spatial energy distribution of Gaussian beams leads to severe degradation of the optical efficiency and

[1]This section is adapted from [40, 54].

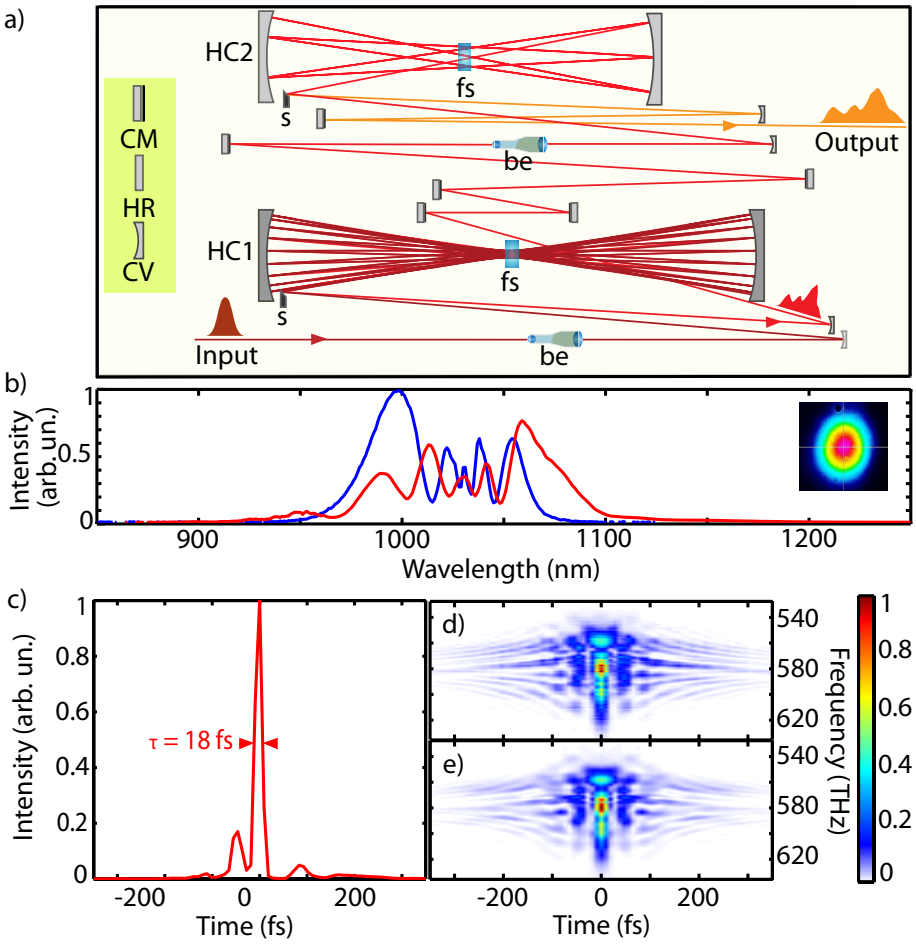

Figure 4.3: (a) Schematic of the cascaded nonlinear broadening setup (fs = fused silica, be = beam expander, HC = Herriott cell, s = scraper, CM = chirped mirror, HR = high reflective mirror, CV = curved mirror). (b) Output spectrum of the first (blue) and the second broadening stage (red). The spectra are normalized to their energy ratio. The inset shows the output beam profile after the second stage. (c) Retrieved temporal profile of the output compressed pulses, supporting 18 fs duration at full width at half maximum (FWHM) (d) The corresponding measured and (e) retrieved spectrograms [54].

the beam quality after SPM [69]. Nevertheless, by keeping the B-integral through the nonlinear medium much smaller than π, excellent compressibility over the whole beam can be achieved [36, 37, 39, 197]. In this scheme, the nonlinear medium is placed at the focal plane of a quasi-waveguide multi-pass geometry with resonator stability. The laser beam is imaged back to the medium after each pass, and the induced phase is compensated in each round trip by using dispersive mirrors.

Figure 4.3(a) shows the schematic of two consecutive Herriott-type imaging cell (HC)s. In the first stage, 265 fs pulses with 6.2 μJ energy from the oscillator were sent into a HC consisting of two tailored curved dispersive mirrors with a radius of curvature of 300 mm. The dispersive mirrors have a GDD of -160 fs^2 over 350 nm spectral bandwidth centered at 1030 nm. A 6.35-mm-thick, AR-coated fused silica (FS) plate was used as the nonlinear medium. The broadened spectrum after 38 passes through the nonlinear medium is shown in Fig. 4.3(b)(blue curve). A 11.3-fold spectral broadening with 82% optical efficiency was obtained. Due to the limited bandwidth of the dispersive mirrors used in the HC and the accumulated residual linear and nonlinear phase at each round trip, increasing the number of passes in the first HC did not lead to further broadening. 7 additional dispersive mirrors with a total GDD of -840 fs^2 at 1030 nm were used to compress the broadened pulse down to 46 fs externally. Afterwards, the 46 fs compressed pulses were sent to a second HC consisting of two tailored concave dispersive mirrors with a radius of curvature of 250 mm. A 6.35-mm-thick, AR-coated, FS plate was used as the nonlinear medium. The dispersive mirrors in this stage provide a GDD of -120 fs^2 over 600 nm spectral bandwidth. The broadened spectrum after 6 passes through the nonlinear medium is shown in Fig. 4.3(b)(red curve). At this stage, the accumulated residual linear and nonlinear phase was negligible, due to the small number of passes. 3 extra dispersive mirrors with a total GDD of -360 fs^2 around 1030 nm were used to compress the broadened pulse down to 18 fs. A home-built, SH-FROG containing a 10 μm BBO crystal was used for characterization (Fig. 4.3(c)(d)(e)).

After both broadening stages, 18 fs pulses with 3.8 μJ pulse energy, corresponding to 60% optical efficiency were delivered.

4.3 Gas-filled single-ring hollow-core photonic crystal fiber compression

[2]The main limiting factor for further pulse compression in multi-pass approach is the precise dispersion compensation in each round trip over a large spectral bandwidth.

This limitation calls for a different spectral broadening scheme [41]. Spectral broadening in gas filled PCF offers high efficiency and damage threshold. Moreover, here the group velocity dispersion and the nonlinearity can be engineered over a broad spectral range,

[2]This section is adapted from [40].

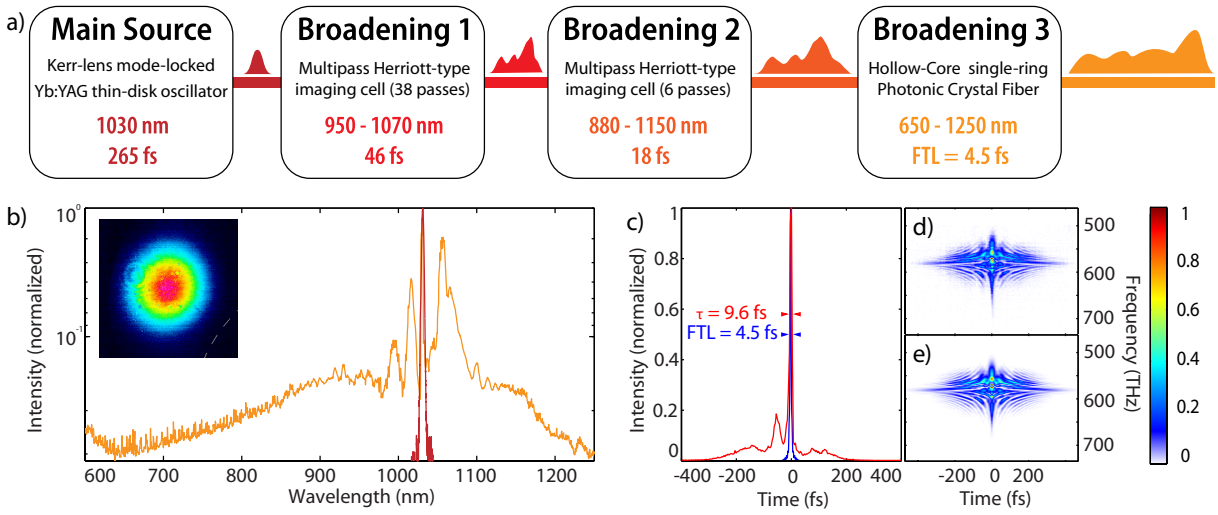

Figure 4.4: (a) Schematic of the external nonlinear spectral broadening system. (b) Input (red) and output (orange) spectra. Inset: spatial profile of the output pulses. (c) Retrieved temporal profile (red) of the output compressed pulses, supporting a FTL of 4.5 fs at FWHM (blue). (d) Measured and (e) retrieved spectrograms [40].

making PCFs a suitable approach for spectral broadening down to single-cycle regime [177, 198].

Figure 4.4(a) shows the setup for broadening in gas-filled SR-PCF. In the experiment, a 17-cm-long SR-PCF with seven thin-walled capillaries arranged around a hollow core was used. 75% of the delivered energy from the second HC broadening stage was focused into the 55 μm diameter core of a SR-PCF by using an achromatic lens with 100 mm focal length. Two additional dispersive mirrors with negative GDD were used to compensate the positive GDD introduced by incoupling optics including achromatic lens, input window of the high pressure gas chamber, and the air path. The SR-PCF was placed inside a miniaturized chamber consisting two cuboid chambers for fiber input and output facets connected by a rigid tube and filled with 10 bar of argon. A protective capillary was used to hold the SR-PCF inside the gas cell. At the input and output, a 3 mm AR-coated FS and a 1.5 mm uncoated Magnesium fluoride (MgF2) window was used, respectively.

The transmission efficiency was measured to be 91% after the output window. Considering the transmission of the output window to be 95%, the fiber itself has a throughput as high as 96%. An Al-enhanced off-axis parabolic mirror with a focal length of 203.2 mm (Edmund Optics) was used to collimate the output beam, before measuring spectrum (Ocean optics HR-4000 and NIR-Quest512-1.6). As shown in Figure 4.4(b), the broadened spectrum spans from 650 to 1250 nm, supporting a FTL pulse duration of 4.5 fs. The excellent output beam profile is shown in the inset of Figure 4.4(b). Preliminary temporal

compression of the pulses with an available chirped-mirror compressor resulted in 9.6 fs pulses (Fig. 4.4(c)-(e)). A home-built SH-FROG containing a 10 μm BBO crystal was used for temporal characterization.

Numerical simulations [41] suggest the pump wavelength of 1030 nm is above the ZDW of the SR-PCF and the fiber operates in the anomalous dispersion regime. By carefully tunning of the gas pressure, the ZDW can be shifted far away from the pump wavelength and a self compressed solitonic propagation can be achieved, resulting in 2.4 fs pulses at the fiber output inside the gas chamber. Considering the dispersion added by the output window of the gas cell and the air path, further compression would be required to achieve FTL pulse duration.

4.4 Extension to mid-infrared

Nonlinear downconversion is a common method to generate coherent broadband MIR pulses, which can be achieved via (i) phase matched DFG or (ii) RQPM in polycrystalline material.

In phase matched DFG, phase-matching is achieved by using birefringent crystals or periodically poled crystals. In downconversion, the nonlinear medium has to be transparent for both pump and the generated MIR pulses. Oxide materials are not transparent for wavelength longer than 5.5 μm. However, nonoxide crystals such as LGS offer excellent transmission up to 11.6 μm and a weak two-photon absorption at 1030 nm, making them suitable for MIR generation from high power Yb-based lasers.

IPDFG relies on a single broadband driving pulse, which provides pump and signal photons for the DFG process. Due to the same origin of both photons, the DFG pulses are intrinsically CEP-stabilized. Despite the lower conversion efficiency in IPDFG compared to DFG, it is less affected by the beam pointing fluctuations with a superior CEP-stability. Therefore, it is a preferred technique for generating required pulse for precision spectroscopy [25, 30].

Another possibility for MIR pulse generation is RQPM in polycrystalline material, which is aggregate of randomly oriented single-crystal grains with tens of micrometers size. Random change of crystal axis in polycrystalline material along the beam path results in a non-zero nonlinear susceptibility, which leads to a coherent growth of the generated MIR field [84]. Although the efficiency of RQPM is lower compared to phase-matched DFG, it offers a broader spectral bandwidth.

In what follows, MIR pulse generation from the Yb:YAG thin-disk oscillator via both approaches are demonstrated and compared.

4.4.1 Phase matched DFG

LGS is one of the most favorable crystals for MIR generation from 1 μm driving lasers, compared to other crystals like $AgGaS_2$ (AGS), $LiInS_2$ (LIS), $LiInSe_2$ (LISe), LGS, $LiGaSe_2$ (LGSe) and gallium selenide (GaSe). Despite its low effective nonlinearity of 4.6 pm/V in the XZ plane, the material has a high damage threshold of 1 TW/cm^2 [30], a wide transparency range, and a wide band gap (4.15 eV). The wide band gap, mitigating multiphoton absorption in the crystal for the pump wavelength at 1030 nm (1.2 eV), along with the high damage threshold, enables a high-power operation.

The setup for MIR generation is depicted in Fig. 4.5. The 18 fs pulses at 1030 nm (see section 4.2) were focused into a 0.5-mm-thick LGS crystal at a peak intensity of 300 GW/cm^2. The crystal was oriented so that the input p-polarized laser pulse was distributed evenly along the extraordinary and the ordinary axes of the crystal for type-I phase matching. The generated MIR radiation was separated by a tailored ZnSe beam splitter (UltraFast Innovations GmbH, F3-S161108, see Fig. 4.6) and then collimated by an off-axis parabolic mirror. After collimation, an average power of 15 mW was measured behind a 7 - 12 μm AR-coated Germanium (Ge) plate (WG91050-G, Thorlabs).

To characterize the generated MIR pulse, EOS similar to the section 3.1.5 was used with some modifications (see Fig. 4.5 Electro-Optic Sampling part). The 18 fs probe pulse at 1030 nm was separated before the LGS crystal by a beam splitter. This way no additional chirp is added to the probe pulse and its duration stays comparable to the half cycle of the carrier wave of the MIR pulse. The probe pulse was delayed by a motorized delay stage (Physik Instrumente Ltd., L-511) which was tracked by a Mach-Zehnder-type interferometric delay tracking (SmarAct GmbH, PicoScale). Subsequently, the probe pulse and the MIR pulse were combined by a 5 mm-thick Ge plate, such that the probe pulse was reflected and the MIR pulse was transmitted. The thickness of the Ge plate (5 mm) was chosen in order to compensate the large negative dispersion introduced by the ZnSe beam splitter (Figure. 4.6) in the MIR beam path. The beam splitter is highly reflective to the 1 μm pulse, and transmits MIR spectral components beyond 2 μm. For lock-in detection, the MIR beam was mechanically chopped at a frequency of 2 kHz. After Ge plate, the two spatially overlapped beams were focused into a 100-μm thick GaSe crystal. SFG of the two pulses results in an effective polarization rotation of the probe pulse, which is directly proportional to the MIR electric field. The thin detection crystal was used to ensure the phase matching across the MIR spectrum.

The measured EOS trace is shown in Fig.4.7(a). The corresponding spectrum is obtained by Fourier transforming of the EOS temporal waveform (Fig. 4.7(b)). The generated spectrum spans from 6.5 to 16.5 μm at 40 dB level. The FWHM pulse duration of the measured MIR pulse is 70 fs, which corresponds to less than two cycles of the MIR electric field with a central wavelength of 11.5 μm. The retrieved spectrum from EOS measurements

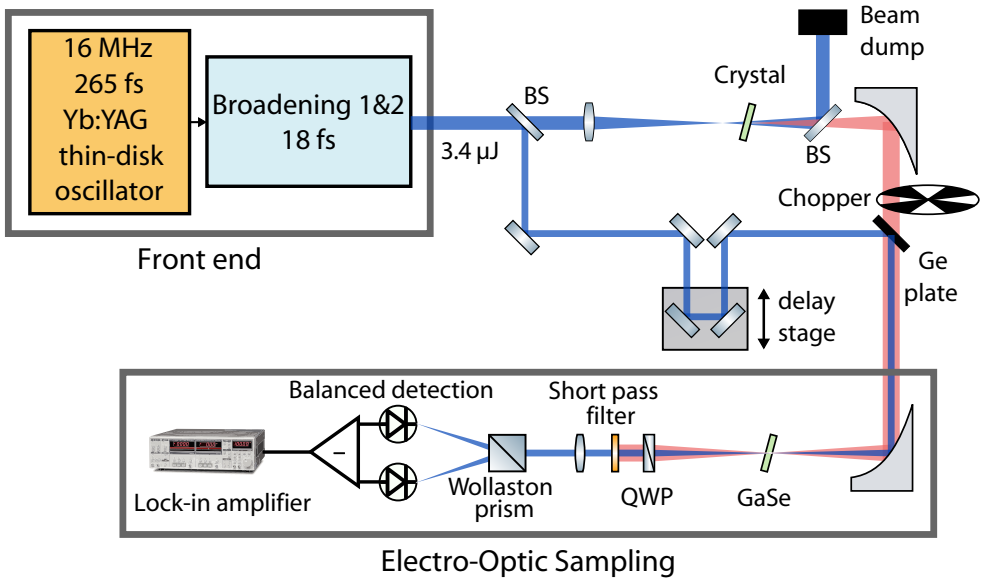

Figure 4.5: Schematic layout of MIR generation via IPDFG and the EOS detection set-up. The driving pulses were focused by a lens with 300 mm focal-length onto the MIR generation crystal. The generated MIR pulses were separated by a tailored beam splitter based on ZnSe substrate and then collimated by an 100 mm focal-length off-axis parabolic mirror. For EOS detection, a low-power copy of the NIR driving pulse was separated from the main NIR beam path by a beam splitter, and served as the probe pulse. The probe pulse was delayed by a motorized delay stage and then combined collinearly with the MIR pulse by a 5-mm-thick uncoated Ge plate, after that the two overlapped pulses were focused onto a 100-μm-thick GaSe crystal by a 50 mm focal-length off-axis parabolic mirror. SFG of the two pulses results in an effective polarization rotation of the probe pulse, which is directly proportional to the MIR electric field. As a function of the delay between the two pulses, the polarization rotation of the probe pulse was read out by a polarization-state detection scheme which consists of a quarter-wave plate (QWP), a short pass filter, a Wollaston prism and a balanced detector with two silicon photodiodes. To perform lock-in detection for the EOS, the MIR beam was mechanically chopped at a frequency of 2 kHz.

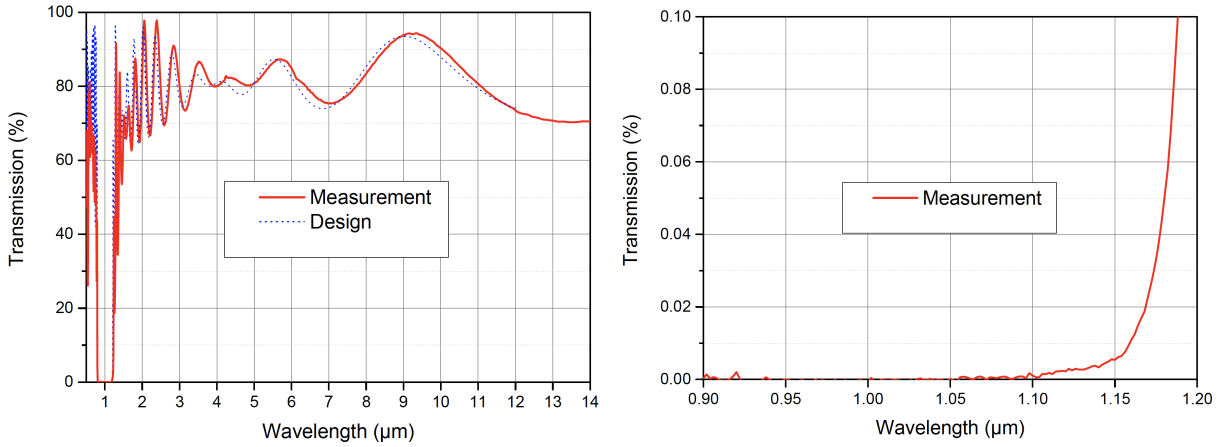

(a) (b)

Figure 4.6: Transmission of the tailored MIR beam splitter measured in 0.5 - 14 μm range (a), and zoomed into 0.9 - 1.2 μm range (b). The high transmission rate of MIR wavelength range and ultra-low transmission around 1 μm driving pulse allows a good separation between the generated MIR pulse and the high power NIR driving pulse.

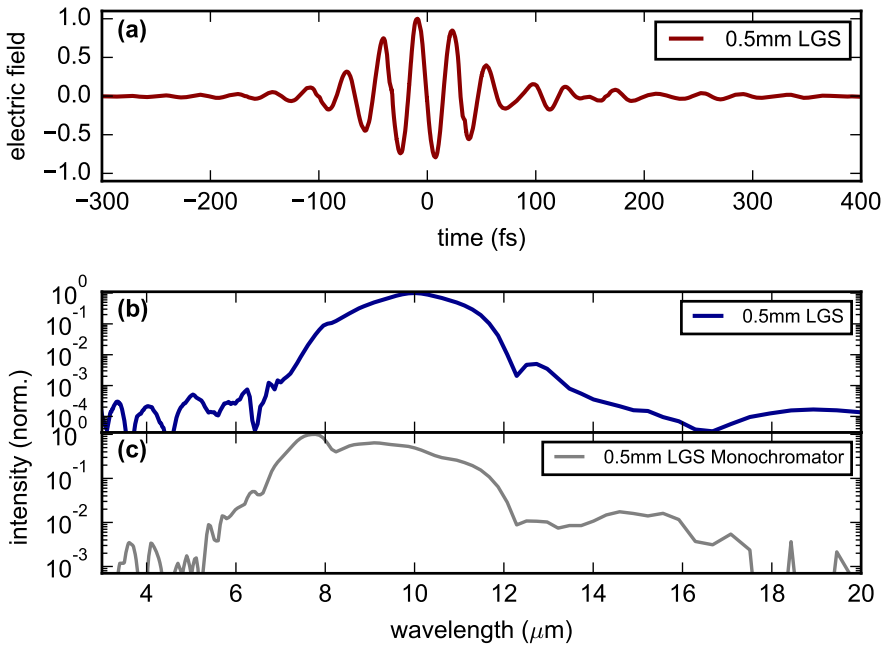

Figure 4.7: (a) Measured EOS trace of MIR transient generated by IPDFG in a 0.5 mm LGS. (b) Measured EOS spectrum (Fourier transform of the temporal waveform in (a)). (c) Spectrum measured by monochromator.

was compared to the measured spectrum using a monochromator (Newport Cornerstone 260)(Fig. 4.7 (b)(c)). It can be seen that the EOS spectrum differs on the short wavelength side of the spectrum. MIR pulse experienced a common path in both measurements, except an additional long-pass filter with a cut-on wavelength of 2.4 μm in front of the monochromator, and an uncoated 5-mm-thick Ge beam combiner in EOS measurement. Therefore, the different transmission efficiencies together with the uncalibrated detector of the monochromator, caused the different spectral response in both measurements.

The high-frequency cutoff of the generated MIR spectrum in LGS crystal is limited to the bandwidth of the NIR driving pulse, while the low-frequency cutoff is limited by the absorption in LGS crystal and the phase-matching. To overcome this limitation, RQPM can be used.

4.4.2 Random quasi-phase-matched DFG

Polycrystalline materials such as ZnSe and ZnS can be used for RQPM. They are aggregations of randomly oriented single-crystal grains with tens of micrometers size. The random distribution of the grain axis in polycrystalline material along the beam path results in phase randomization and a non-zero nonlinear susceptibility, which leads to a MIR signal much higher than the contribution of a single coherence length. This process does not require a specific crystal orientation or input beam polarization. In 2004, Baudrier-Raybaut et al. used two nanosecond lasers to generate a tunable MIR pulses in polycrystalline ZnSe [84]. They observed linear growth of the signal versus sample thickness. The maximum conversion efficiency was reached when the average grain size was close to the coherence length of the generated pulses. Ru et al. employed RQPM in polycrystalline ZnSe as the optical parametric oscillator (OPO) gain medium. They could successfully generate a broadband spectrum spanning from 3 to 7.5 μm with 20 mW average power, when pumped at 2.35 μm [199]. However, the doubly resonant OPO requires to adjust cavity length at interferometric precision, which increases the complexity. Zhang et al. could generate broadband MIR pulses (3 - 15 μm) by single pass IPDFG of 1.03 μm 16 fs pulses for the first time [85]. However the temporal evolution of the generated pulses in this approach has not been studied. In the following, the MIR pulses generated based on RQPM in polycrystalline ZnSe and ZnS pumped by high power 1.03 μm laser are characterized temporally.

MIR generation in ZnSe and ZnS Among the many disordered polycrystalline materials, ZnSe is one of the most favorable materials to generate MIR via IPDFG due to its broad transparency (0.55 - 20 μm), high nonlinearity ($d_{14} = 20$ pm/V), high optical damage threshold, good mechanical properties, and its availability. ZnS offers properties similar to ZnSe, apart from its narrower transparency window (0.55 - 15 μm). Both materials were

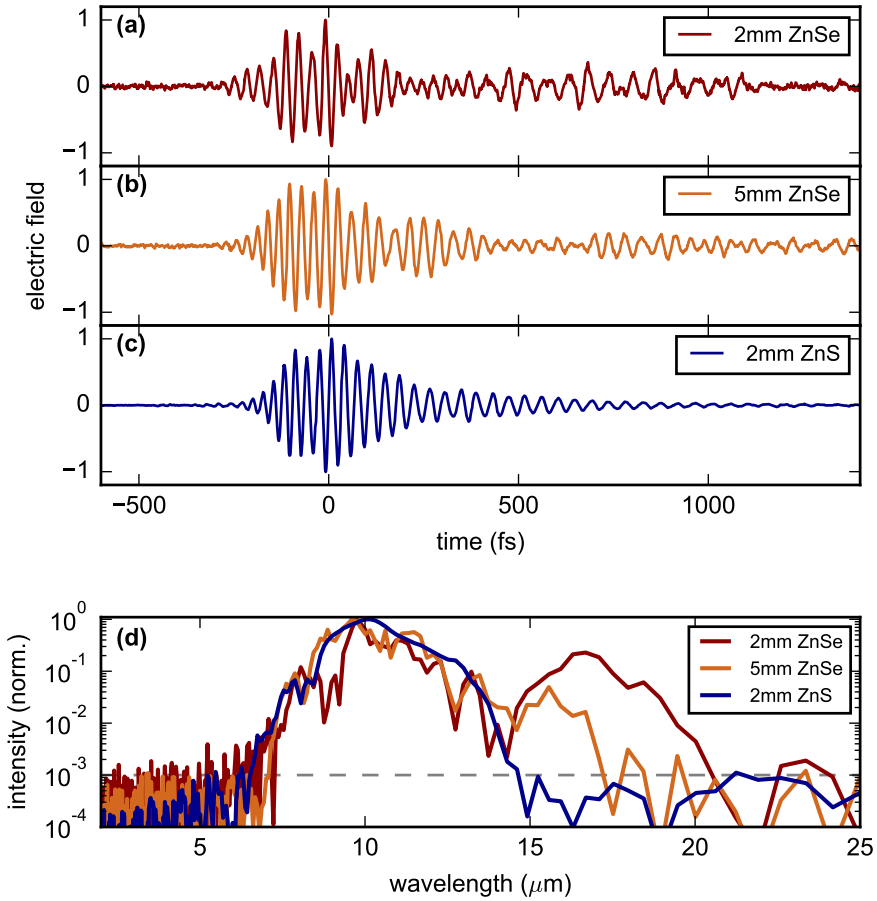

Figure 4.8: Measured EOS trace of MIR transient generated by IPDFG in (a) 2 mm ZnSe, (b) 5 mm ZnSe, (c) 2 mm ZnS. (d) Measured EOS spectrum (Fourier transform of the temporal waveform).

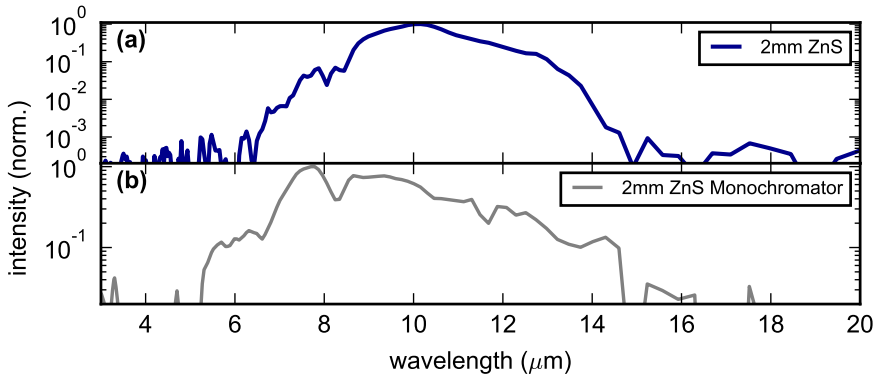

Figure 4.9: Comparison of the IPDFG spectrum in ZnS measured by (a) EOS and (b) monochromator.

studied for MIR generation.

The 18 fs pulses at 1030 nm with 55 W average power were focused into 2-mm-thick ZnSe crystal at the peak intensity of 90 GW/cm^2 (Fig. 4.5). The crystal has a grain size of 50 - 70 μm according to the supplier (Edmund Optics). An incident angle of 10° was introduced to avoid the back-reflection to the laser. The generated MIR pulse was separated from the driving beam by a tailored long-pass beam splitter and characterized by EOS setup.

The measured EOS trace is shown in Fig. 4.8 (a). The corresponding spectrum is shown in Fig. 4.8 (d) (red cueve) covering the spectral range from 6 to 21 μm (at –30 dB). An average power of 50 μW was measured behind a 7 - 12 μm AR-coated Ge window (WG91050-G, Thorlabs). The average power of the MIR pulses is estimated to be higher than this value, by taking into account the high loss of the AR-coated Ge window above 12 μm and the reflection loss on the uncoated ZnSe crystal surface.

The temporal waveform of the MIR pulse generated in a 2-mm-thick ZnS crystal is shown in Fig. 4.8 (c). A spectral coverage of 6 to 15 μm was obtained, as shown in Fig. 4.8 (d) (blue curve). An average power of 80 μW was measured behind a 7 - 12 μm AR-coated Ge window (WG91050-G, Thorlabs). The grain size for the ZnS crystal was estimated to be around 60 μm according to manufacturer (Korth Kristalle GmbH). The retrieved spectrum from EOS (Fig. 4.9 (a)) and the measured spectrum by monochromator (Fig. 4.9 (b)) show a good agreement up to 6.5 μm.

In order to increase the average power of the MIR pulses, a 5 mm ZnSe was used. The measured EOS waveform and its corresponding spectrum are shown in Fig 4.8 (b) and (d), respectively. However, no linear scaling of average power versus the thickness of the crystal was observed, due to high dispersion of ZnSe at 1 μm.

Fig. 4.10 shows the FROG measurement of the transmitted pulse from a 2 mm and 5 mm ZnSe. Due to the large amount of the introduced dispersion, the 18 fs driving pulse was temporally stretched to 567 fs after propagating through the 5 mm ZnSe (Fig. 4.10 (f)). Therefore, the peak intensity inside the crystal was decreased and the efficiency and bandwidth of IPDFG were limited. Fig. 4.8 (d) compares the narrowed generated spectra in a 2 mm and 5 mm ZnSe.

Effect of the spatial inhomogeneity Random orientation and size of the single-crystal grains in polycrystalline material results in inhomogeneous nonlinear properties. Fig. 4.11 (a) shows the effect of spatial variations of a ZnSe crystal on the SHG conversion efficiency [199]. The efficiency in 'hot' spot can be 2.5-3 times higher than the average. A similar behavior has been observed in EOS measurement. To this end, series of EOS measurements have been carried out at different positions on the crystal. The ZnSe crystal was mounted on a rotational mount. As shown in Fig. 4.11 (b), the laser beam spot on the crystal was placed slightly off center, such that by rotating the rotational mount, laser beam passes through different positions. Two additional EOS measurements were carried out

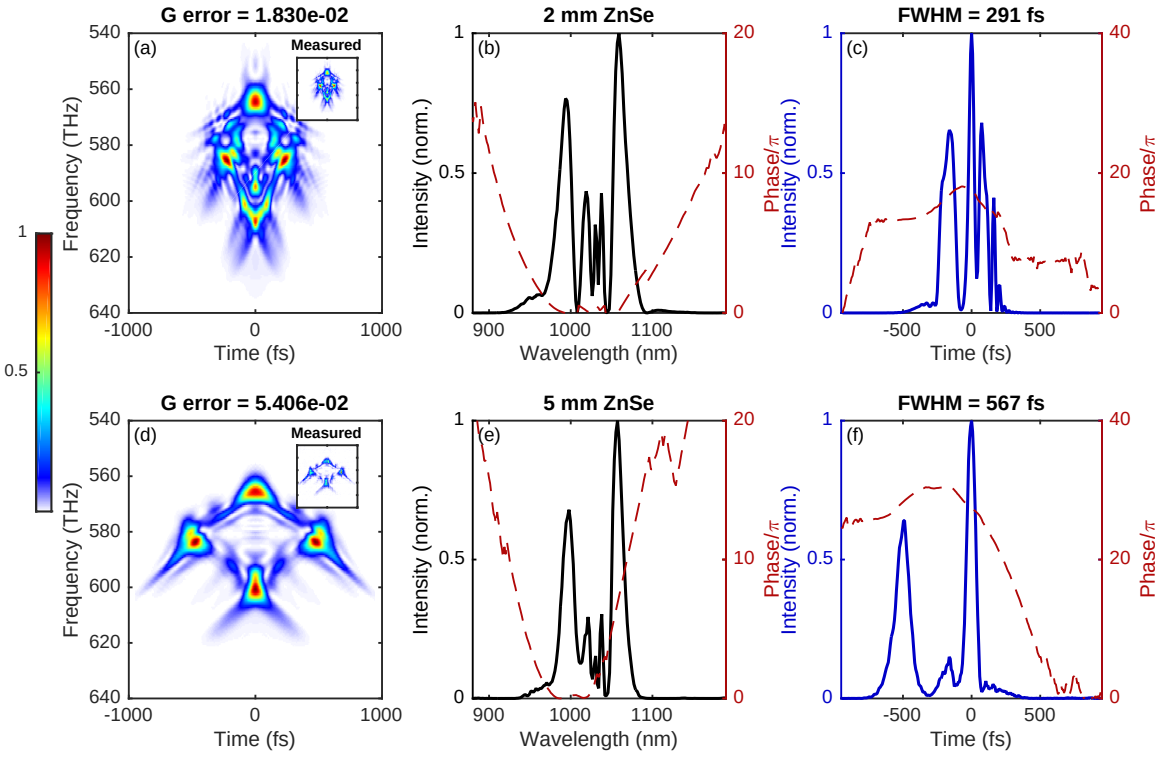

Figure 4.10: FROG measurements of the residual IPDFG driving pulse after 2 mm ZnSe (first row) and after 5 mm ZnSe (second row). (a) Retrieved FROG spectrogram of 2 mm ZnSe. Inset: measured FROG spectrogram. (b) Retrieved spectrum (black) and spectral phase(red dashed) of 2 mm ZnSe. (c) Retrieved time envelope (blue) and temporal phase (red dashed) of 2 mm ZnSe. (d) Retrieved FROG spectrogram of 5 mm ZnSe. Inset: measured FROG spectrogram. (e) Retrieved spectrum (black) and spectral phase (red dashed) of 5 mm ZnSe. (f) Retrieved time envelope (blue) and temporal phase (red dashed) of 5 mm ZnSe.

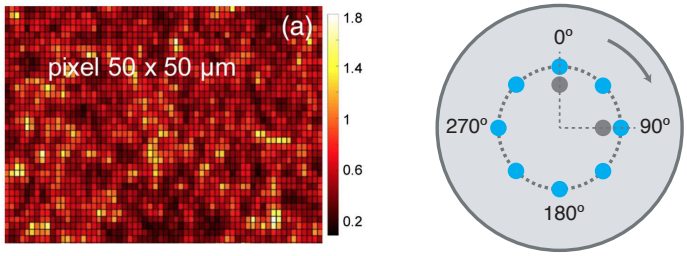

(a) (b)

Figure 4.11: (a) A typical result of SHG mapping in polycrystalline ZnSe. There are "hot" spots where the efficiency of SHG is 2.5-3 times higher than the average. Figure adapted with permission from [199] © The Optical Society. (b) Schematic illustration of corresponding different positions on the crystal for different orientation angles in EOS measurements of polycrystalline ZnSe and ZnS. The polycrystalline ZnSe and ZnS were mounted on rotational mounts. The laser beam spot on the crystal was placed slightly off center, such that by rotating the rotational mount, laser beam passes through different positions. The blue dots depict the different orientation angles with 45° interval. At 0° and 90° positions, additional EOS measurements were carried out by shifting the height of the rotational mount, correspond to a shift of blue dots to grey dots.

at 0° and 90° by shifting the height of the rotational mount (grey spot in Fig. 4.11 (b)). The difference between two measurements at the same angle proved that the observed variations are actually position dependent rather than orientation dependent.

The measured EOS traces with 45° interval are shown in Fig. 4.12 (a) - (h). The corresponding spectra at 3 different angles are shown in Fig. 4.12 (i). Different positions of the crystal not only affected the temporal chirp, but also changed the bandwidth of the MIR spectrum. The broadest spectrum covering 7 - 21 μm was observed for crystal position at 135 degree (Fig. 4.12 (i)). The difference between the three sampled spectra is more prone at longer longer wavelength. This is due to the different involved mechanisms for generating new spectral components. The short wavelength region of the spectrum is mainly generated in the first several micrometers of the crystal, as at longer crystal thickness the high dispersion in ZnSe temporally separates the two cutoffs of the spectrum.

Fig. 4.13 shows the position variance of EOS measurements in 5 mm ZnSe. As can be seen in Fig. 4.13 (i), the measured waveform has a strange tail in the time domain and broadest spectral bandwidth. The larger oscillation period at the tail of the waveform correspond to the generated component at longer wavelength.

Fig. 4.14 shows the position variance of EOS measurements in a 2 mm ZnS. Although the sampled EOS waveforms have different chirp, their spectral coverage is similar.

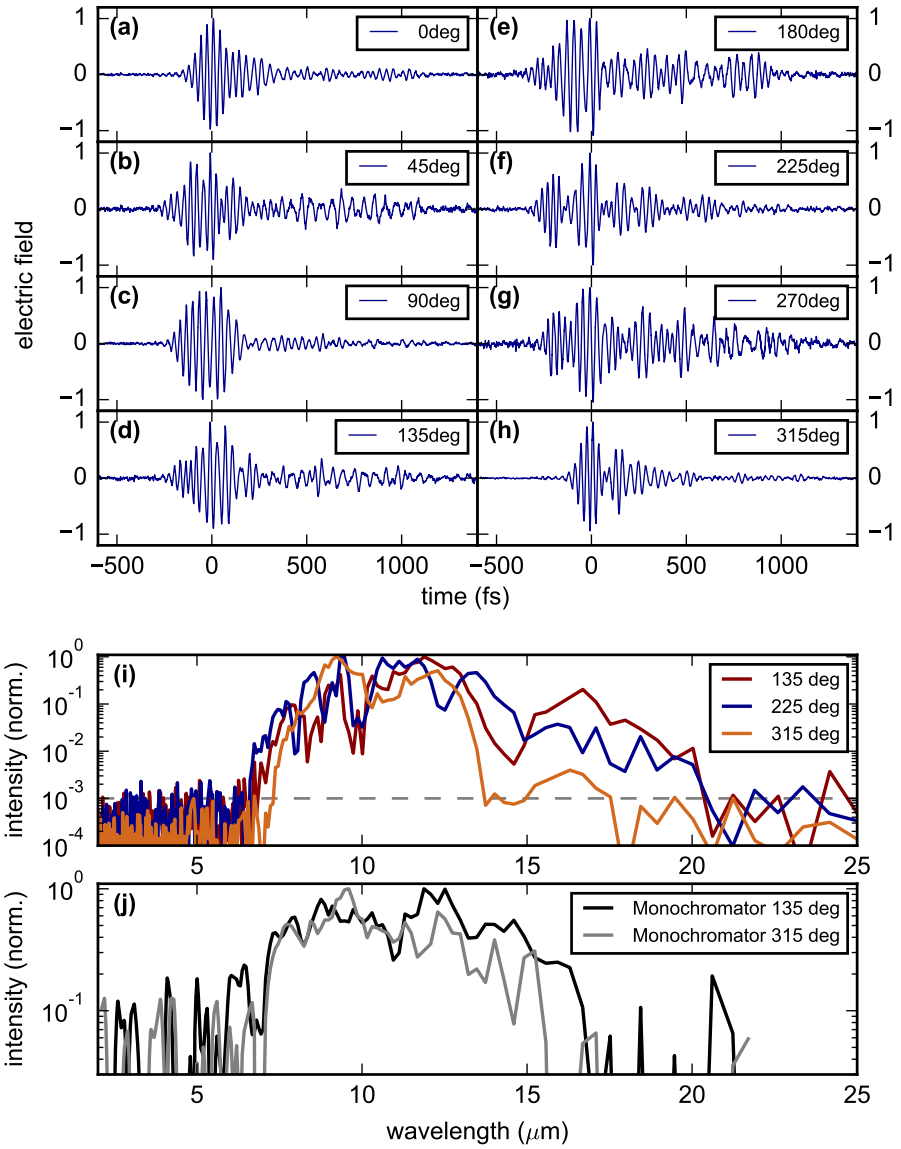

Figure 4.12: (a-h) Measured EOS trace of MIR transient generated by IPDFG in a 2 mm ZnSe at different orientation angles. (i) Measured EOS spectrum (Fourier transform of the temporal waveform) at three angles including the broadest and narrowest cases. (j) Spectra of the broadest and narrowest cases measured by monochromator.

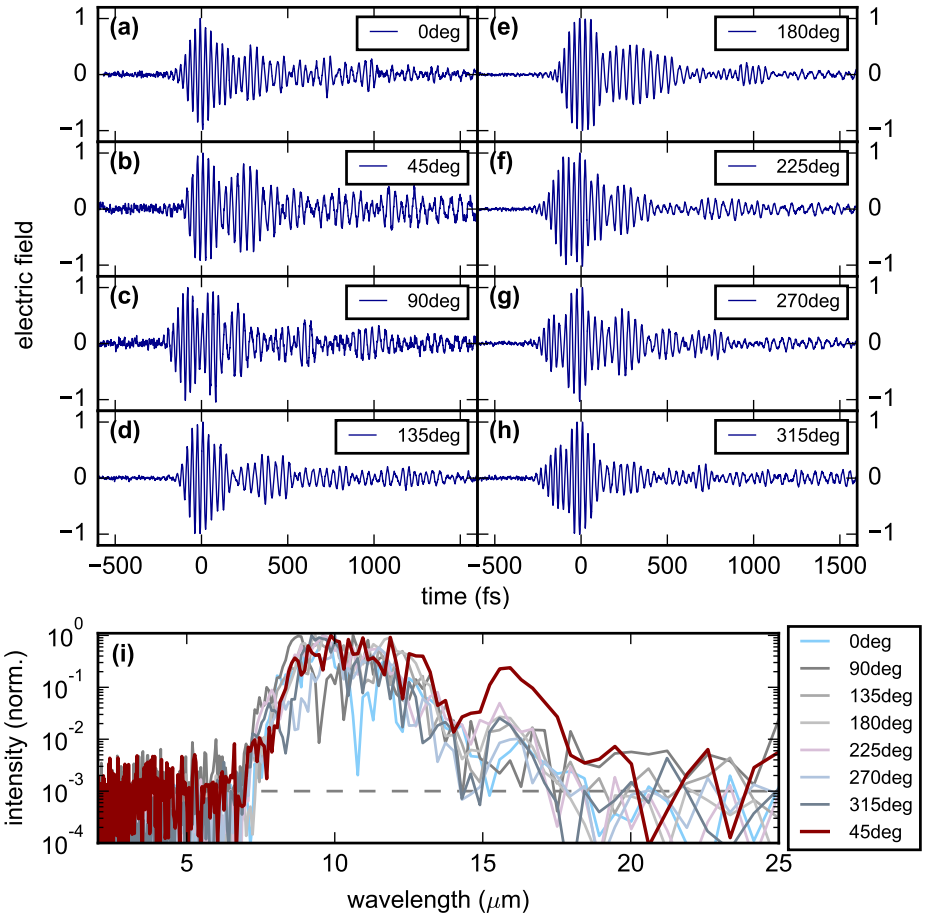

Figure 4.13: (a-h) Measured EOS trace of MIR transient generated by IPDFG in a 5 mm ZnSe at different orientation angles. (i) Measured EOS spectrum (Fourier transform of the temporal waveform) at different angles.

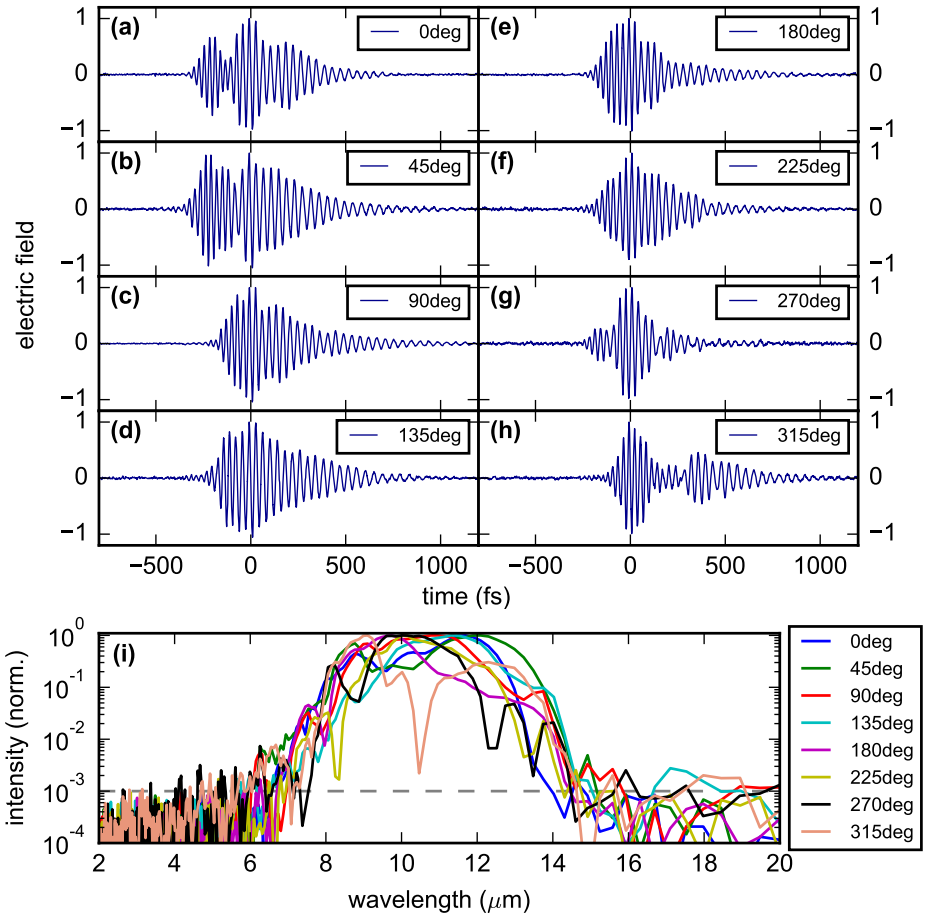

Figure 4.14: (a-h) Measured EOS trace of MIR transient generated by IPDFG in a 2 mm ZnS at different orientation angles. (i) Measured EOS spectrum (Fourier transform of the temporal waveform) at different angles.

4.4.3 Conclusion

In conclusion, broadband MIR generation driven by 1030 nm, 18 fs pulse was investigated in phase matched and RQPM regime. Phase matched IPDFG in LGS provides high efficiency with a sufficient bandwidth to support few cycle pulses. In comparison, RQPM offers a broader bandwidth, however, at lower efficiency. It was observed that for few-cycle driving pulses, the energy of the generated pulses did not scale with the thickness of the crystal, due to the high dispersion in ZnS and ZnSe. Moreover, the temporal structure and the bandwidth of the generated pulses were strongly dependent on the spatial inhomogeneity of the crystal. Based on our temporal analysis, the high-frequency components are generated at the entrance of the crystal before dispersion sets in, while the generation of lower frequencies is the interplay between dispersion, nonlineary and grain size.

4.5 Super-octave terahertz generation

[3]Until now, broadband tabletop THz sources have been mostly driven by Ti:Sa based amplifier systems with limited average power at kHz repetition rate. This combined with the low conversion efficiencies in THz generation results in a limited average power. Besides, the kHz repetition rate limits the measurement SNR and acquisition time. Increasing the average power and repetition rate of broadband THz sources would be of great interest to various THz applications. In this regard, this section demonstrates the experimental study of optical rectification in GaP driven by high power few-cycle pulses.

As shown in Fig. 4.15, the 3.8 μJ, 18 fs pulses obtained from section 4.3 were focused into a <110>-cut GaP crystal by a convex lens with 250mm focal length. The GaP crystal was placed before the focus where the laser beam had a $1/e^2$ beam diameter of 700 μm, corresponding to a peak intensity of 97 GW/cm^2. A 2-inch diameter, 101.6 mm focal length, bare-gold coated off-axis parabolic mirror with through hole was used to collimate the generated THz beam, and to separate the pump beam. After propagating through a Teflon filter, which blocked the residual pump, the collimated THz beam was guided towards an EOS setup for characterization. The EOS setup is similar to the one described in section 4.4.1. Less than 1% of the pump beam was separated by a CaF_2 wedge before the THz generation stage to be used as the probe beam for the EOS. A 2-inch diameter, 50.8 mm focal length, bare-gold coated off-axis parabolic mirror with through hole was used to focus the THz beam into the EOS nonlinear crystal. The probe beam was delayed by a motorized delay stage (Physik Instrumente Q-545), and then combined with the THz beam via the through hole of the off-axis parabolic mirror. The two beams were overlapped and focused into a 0.15 mm-thick <110>-cut GaP crystal for EOS, due to the pockles effect, the THz field modifies the refractive index of the GaP proportional to the

[3]This section is adapted from [54].

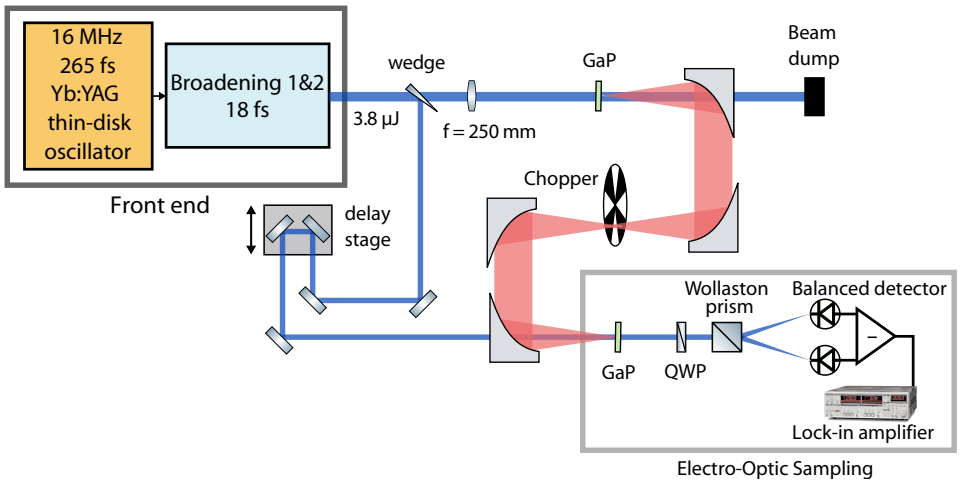

Figure 4.15: Experimental setup of THz generation in GaP via optical rectification, and the detection by electro-optic sampling. BS: beam splitter; QWP: quarter-wave plate.

field strength. By detecting the changes in the polarization state of the probe beam, the THz field can be resolved. To perform lock-in detection, the THz beam was mechanically chopped at a frequency of 1 kHz. The THz power was measured at the position of the EOS crystal by a commercial Golay cell detector (Tydex GC-1P).

Figure 4.16(a) shows the EOS trace of the generated THz transient in 0.2 mm-thick GaP crystal, which was acquired in a 10 minutes scan with 30ms integration constant. Figure 4.16(b) shows the retrieved spectrum. Multiple dips appeared across the whole spectrum range, due to the THz absorption by water vapor molecules in the surrounding air (46% relative humidity in the laboratory atmosphere) [200], which fit well with the water absorption lines obtained from the HITRAN database [201].

Figure 4.16(c) shows the retrieved spectra of the generated THz pulses in 2 mm, 1 mm, and 0.2 mm thick GaP crystal, with the corresponding power of 100 μW, 50 μW and 7 μW, respectively. The broadest spectrum was generated in 0.2 mm GaP with a cutoff frequency above 6 THz at 40 dB level. Compare to 0.2 mm GaP, a 2 mm GaP provided 10 times more average power, with a narrower spectrum as the trade off.

The large amplitude of the FID at the trailing edge of the EOS trace indicates a high amount of the generated THz pulses was absorbed by water vapor molecules in air. Therefore, a higher output power of the generated THz transients can be expected by extracting water of atmospheric from system.

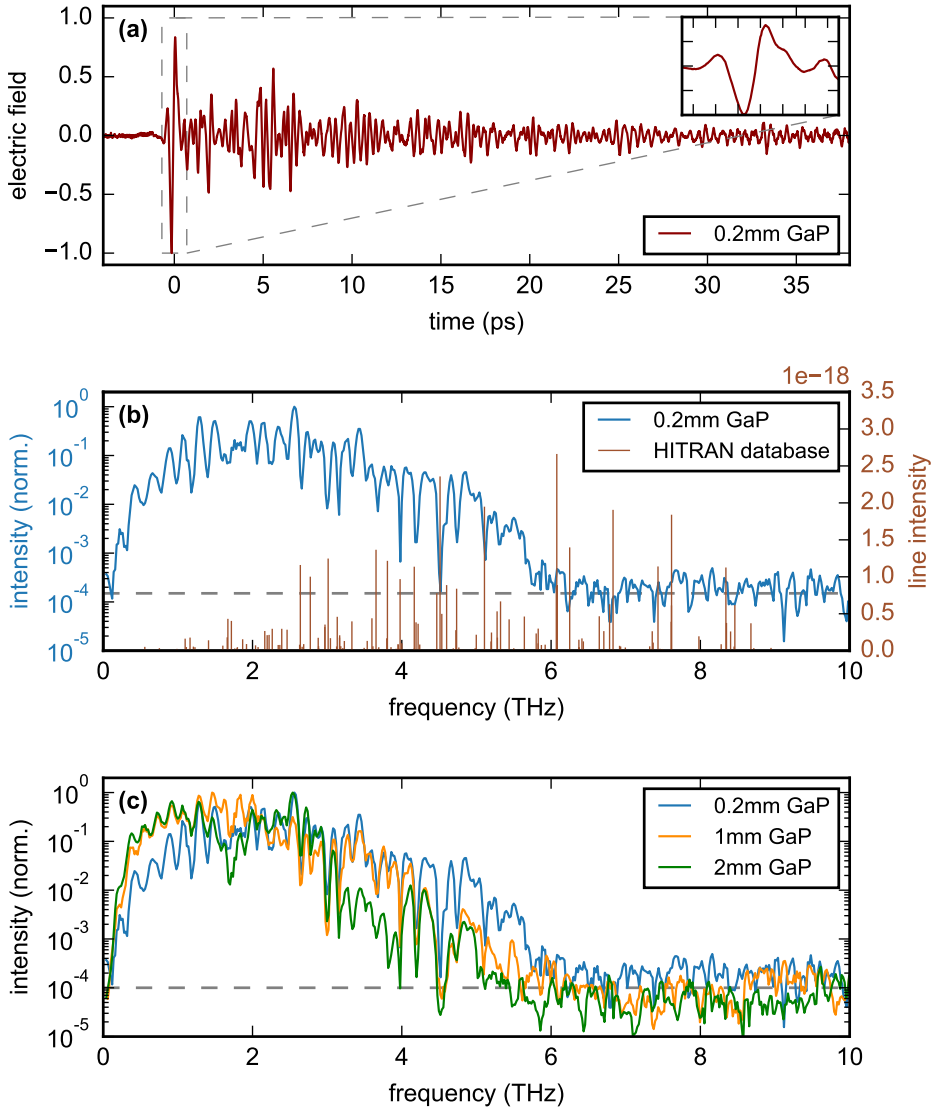

Figure 4.16: (a) Electric field of THz transient generated in a 0.2 mm-thick GaP crystal, measured by electro-optic sampling containing a 0.15 mm-thick GaP crystal. The free induction decay can be observed at the trailing edge of the waveform, which indicates the absorption of the generated THz pulses by water vapor molecules. The inset shows the zoomed in region around the main peak. (b) Corresponding retrieved spectrum of the waveform shown in panel (a). The brown lines show water absorption lines from the HITRAN database [201]. (c) Spectra of the THz pulses generated from different thicknesses of GaP at same peak intensity of 97 GW/cm^2.

4.6 Conclusion

In conclusion, this chapter presented results on generating broadband coherent pulses based on a high-power Kerr-lens mode-locked Yb:YAG thin-disk oscillator at 16 MHz repetition [26]. Two external nonlinear spectral broadening stages based on multi-pass spectral broadening in bulk was employed to compress the 265 fs pulses of the oscillator to 18 fs. Using these pulses, investigation on (i) further broadening in gas filled SR-PCF and (ii) extending spectral coverage towards MIR and THz were carried out. Preliminary compression of 2.85 μJ, 18 fs pulses down to 9.6 fs was demonstrated in a gas-filled SR-PCF. Such intense, broadband coherent sources operating at megahertz repetition rate in NIR wavelength, can be an ideal source for field-resolved NIR spectroscopy, or field synthesis, if CEP-stability were improved [29, 69]. Extension towards MIR spectral range via IPDFG in (i) phase matched crystal LGS and (ii) RQPM in polycrystalline ZnSe and ZnS were demonstrated. The phase matched IPDFG provides much higher efficiency at proper phase matching angle, while with RQPM a very broad phase-matching bandwidth could be achieved without restrains on the incident angle, however, at the cost of efficiency. It was observed that the temporal profile of the generated MIR pulses and their spectrum, strongly coupled to spatial inhomogeneity of the nonlinear crystal. Generation of broadband THz pulse with 0.1 mW output power and 6 THz cutoff frequency was demonstrated. The presented broadband coherent pulse generation in VIS-NIR, MIR and THz range at MHz repetition rate holds promise to pave the way for spectroscopy at a higher SNR.

Chapter 5

Conclusion and Outlook

In conclusion, this work demonstrated a prototype OPCPA-based parallel field synthesizer based on the generation of CEP-stable ultrabroadband continuum driven directly from a 5 kHz picosecond home-built high power Yb:YAG thin-disk amplifier, and its application in NIR field-resolved spectroscopy.

The generated CEP-stable ultrabroadband SC contains 4 μJ energy with a spectrum spanning from 450 nm to beyond 2500 nm, and can serve as an ideal seed pulse for OPCPAs and high energy field-synthesizers. Without the need for additional complex temporal synchronization. Further extension of the ultra-broadband, CEP-stable spectrum to MIR was demonstrated. The numerical analysis suggested the energy of the MIR can be scaled up to 60 μJ, when the system is used to full potential.

Seeded by the generated CEP-stable ultrabroadband continuum in the VIS and NIR, a prototype OPCPA-based parallel field synthesizer was demonstrated. Two OPCPA channels centered at 2 μm and 1 μm boosted the energy of the seed pulses to 25 μJ. Temporally compression of each channel resulted in 18 fs and 6 fs pulses at 2 μm and 1 μm respectively. It was shown numerically, that by using the remaining energy of the Yb:YAG thin-disk amplifier to pump additional OPCPA, further energy scaling of synthesized light transient to 4 mJ is feasible. Despite the remaining long-term drifts, the short-term spatial and temporal stability of the synthesizer was verified by using 1 μm pulses to resolve the electric field of the 2 μm pulses with sub-cycle precision.

As the first application of such system, NIR field-resolved spectroscopy of water molecules is demonstrated. A detection sensitivity comparable to the conventional spectroscopy techniques was achieved, limited to the stability of the interferometer and the relatively low repetition rate of the frontend.

A different approach utilizing cascaded quadratic nonlinearity for supercontinuum generation was introduced, which leads to a lower threshold power for supercontinuum generation and a higher spectral density in the newly generated spectral region. Such supercontinuum with mixed polarization state paves the way to a new type of synthesizer:

cross-polarized pulse synthesizer. With a common amplification beam path for all spectral regions, this design could enhance the stability of the system, reduce the size and complexity, and most importantly reduce the temporal jitter initiated from systematic complexity.

To improve the signal-to-noise ratio and reduce the measurement time of NIR field resolved spectroscopy experiments, a 16 MHz source based on high power Yb:YAG thin-disk oscillator was developed. The 265 fs output pulses from the oscillator were compressed to 18 fs in two external nonlinear stages based on multi-pass spectral broadening in bulk. Further pulse compression in a gas filled SR-PCF resulted in generating a broadband spectrum with a FTL of 4.5 fs. In addition to the broad spectral coverage in the NIR region, further extensions to MIR and THz were presented. It was shown a broad MIR spectrum from 5 - 20 μm could be generated either using phase matched IPDFG in LGS crystal with high efficiency, or RQPM in polycrystalline ZnSe and ZnS with low efficiency but higher spectral coverage. Broadband THz generation at MHz repetition rate were demonstrated with up to 0.1 mW output power. The high power Yb:YAG thin-disk based laser enabled the generation and detection of THz spectra up to nearly 6 THz.

Advances in the ytterbium laser technology over the last decade combined with OPCPAs present a new perspective for reaching higher peak- and average-powers. Coherent combination of several OPCPA channels hold promise for synthesizing, multi-octave waveforms and generating sub-cycle pulses with unprecedented peak and average power. Further energy scaling of light transients to beyond 4 mJ can be achieved by using a 5 kHz, 1 kW, 200 mJ Yb:YAG thin-disk amplifier as the driving laser [20]. Advancing the frontiers of high peak- and average-power tailored light transients can open up unprecedented opportunities in attosecond and high-field physics.

SC generation by harvesting the cascaded quadratic nonlinearity at ZDW offers a new route towards Watt-level SC generation. The required lower peak intensity for SC generation due to the high effective nonlinear refractive index in a nonlinear medium, allows for a looser focusing condition with a lower power density.

Seeded by such cross-polarized SC, a new type of high-energy wave synthesizer based on cross-polarized wave synthesis [22] holds promise to enhance the stability of the generated light transients by reducing the size and complexity of the system.

The intense, broadband coherent sources operating at megahertz repetition rate in NIR wavelength can be an ideal source for field-resolved NIR spectroscopy, or field synthesis, if CEP-stability were improved [29, 69]. With the extension towards MIR, field resolved MIR spectroscopy provides huge potential in improving molecular detection sensitivity and coverage for probing complex, real-world biological settings. Moreover, the extension towards THz in a solid-state emitter offers a promising method for producing broadband THz pulses, with a wide range of applications in THz imaging and spectroscopy at rapid acquisition time and enhanced signal-to-noise ratio.

Appendix

List of Publications

Peer reviewed articles:

- H. Fattahi, A. Alismail, **H. Wang**, J. Brons, O. Pronin, T. Buberl, L. Vámos, G. Arisholm, A. M. Azzeer, and F. Krausz, "High-power, 1-ps, all-Yb:YAG thin-disk regenerative amplifier," *Optics Letters* **41** (6), pp. 1126-–1129, 2016, `https://doi.org/10.1364/OL.41.001126`.

- T. Buberl, A. Alismail, **H. Wang**, N. Karpowicz, and H. Fattahi, "Self-compressed, spectral broadening of a Yb:YAG thin-disk amplifier," *Optics Express* **24** (10), pp. 10286–10294, 2016, `https://doi.org/10.1364/OE.24.010286`.

- H. Fattahi, **H. Wang**, A. Alismail, G. Arisholm, V. Pervak, A. M. Azzeer, and F. Krausz, "Near-PHz-bandwidth, phase-stable continua generated from a Yb:YAG thin-disk amplifier," *Optics Express* **24** (21), pp. 24337–24346, 2016, `https://doi.org/10.1364/OE.24.024337`.

- A. Alismail, **H. Wang**, N. Altwaijry, and H. Fattahi, "Carrier-envelope phase stable, 5.4 μJ, broadband, mid-infrared pulse generation from a 1-ps, Yb:YAG thin-disk laser," *Applied Optics* **56** (17), pp. 4990–4994, 2017, `https://doi.org/10.1364/AO.56.004990`.

- **H. Wang**, A. Alismail, G. Barbiero, M. Wendl, and H. Fattahi, "Cross-polarized, multi-octave supercontinuum generation," *Optics Letters* **42** (13), pp. 2595–2598, 2017, `https://doi.org/10.1364/OL.42.002595`.

- A. Alismail, **H. Wang**, J. Brons, and H. Fattahi, "20 mJ, 1 ps Yb:YAG thin-disk regenerative amplifier," *Journal of Visualized Experiments: JoVE* (125), 2017, `https://doi.org/10.3791/55717`.

- **H. Wang***, A. Alismail*, G. Barbiero, R. N. Ahmad, and H. Fattahi "High energy, sub-cycle, field synthesizers," *IEEE journal of selected topics in quantum electronics* **25** (4), pp. 1–12, 2019, https://doi.org/10.1109/JSTQE.2019.2924151.

- A. Alismail*, **H. Wang***, G. Barbiero, N. Altwaijry, S. A. Hussain, V. Pervak, W. Schweinberger, A. M. Azzeer, F. Krausz, and H. Fattahi, "Multi-octave, CEP-stable source for high-energy field synthesis," *Science Advances*, **6** (7), eaaq1526, 2020, https://doi.org/10.1126/sciadv.aax3408.

- G. Barbiero, **H. Wang**, J. Brons, B.-H. Chen, V. Pervak, and H. Fattahi, "Super-octave terahertz solid-state emitter driven by Yb:YAG thin-disk oscillator," *Journal of Physics B: Atomic, Molecular and Optical Physics*, **53** (12), pp. 125601, 2020, https://doi.org/10.1088/1361-6455/ab8049.

Conference contributions:

- H. Fattahi, **H. Wang**, A. Alismail, and F. Krausz, "Towards high-power, multi-TW light transients," in *CLEO: Applications and Technology*, pp. SM1M–6, Optical Society of America, 2016, https://doi.org/10.1364/CLEO_SI.2016.SM1M.6.

- A. Alismail, **H. Wang**, A. Azzeer, F. Krausz, and H. Fattahi, "Towards multi-mJ, OPCPA-based field synthesizer," in *The European Conference on Lasers and Electro-Optics*, pp. CG–P–20, Optical Society of America, 2017, https://www.osapublishing.org/abstract.cfm?uri=cleo_europe-2017-CG_P_20.

- **H. Wang**, A. Alismail, G. Barbiero, M. Wendl, F. Krausz , and H. Fattahi, "Cross-polarized supercontinuum generation in $LiNbO_3$ for a multi-mJ waveform synthesizer," in *The European Conference on Lasers and Electro-Optics*, pp. CG–4–2, Optical Society of America, 2017, https://www.osapublishing.org/abstract.cfm?uri=cleo_europe-2017-CG_4_2.

- **H. Wang**, A. Alismail, and H. Fattahi, "Supercontinuum generation in lithium niobate with an enhanced nonlinearity," in *Ultrafast Optics XI*, 2017.

- A. Alismail, **H. Wang**, G. Barbiero, S. A. Hussain, W. Schweinberger, F. Krausz, and H. Fattahi, "Near-infrared molecular fieldoscopy," in *CLEO: Applications and Technology*, pp. AF3K–5, Optical Society of America, 2019, https://doi.org/10.1364/CLEO_AT.2019.AF3K.5.

- A. Alismail, **H. Wang**, G. Barbiero, S. A. Hussain, W. Schweinberger, F. Krausz, and H. Fattahi, "Near-infrared molecular fieldoscopy of water," in *Multiphoton Microscopy*

in the Biomedical Sciences XIX, **10882**, p. 1088231, International Society for Optics and Photonics, 2019, https://doi.org/10.1117/12.2507604.

- A. Alismail, **H. Wang**, G. Barbiero, and H. Fattahi, "All ytterbium frontend for high-energy field synthesizers," in *The European Conference on Lasers and Electro-Optics*, pp. CF–9–4, Optical Society of America, 2019, https://www.osapublishing.org/abstract.cfm?uri=CLEO_Europe-2019-cf_9_4.

- A. Alismail, **H. Wang**, G. Barbiero, F. Krausz, and H. Fattahi, "Near-infrared fieldoscopy of water," in *The European Conference on Lasers and Electro-Optics*, pp. CD–2–2, Optical Society of America, 2019, https://www.osapublishing.org/abstract.cfm?uri=CLEO_Europe-2019-cd_2_2.

- G. Barbiero, R.N. Ahmad, **H. Wang**, F. Köttig, D. Novoa, F. Tani, J. Brons, P.S.J. Russell, F. Krausz, and H. Fattahi, "v," in *The European Conference on Lasers and Electro-Optics*, pp. Cf–1–2, Optical Society of America, 2019, https://www.osapublishing.org/abstract.cfm?uri=CLEO_Europe-2019-cf_1_2.

- **H. Wang**, G. Barbiero, F. Krausz, and H. Fattahi, "5-20 μm, mid-infrared pulse generation from a 16 MHz, Yb:YAG thin-disk oscillator in polycrystalline ZnSe," in *Ultrafast Optics XII*, 2019.

- G. Barbiero, R. N. Ahmad, **H. Wang**, F. Köttig, J. Brons, D. Schade, F. Tani, P. S. Russell, F. Krausz, and H. Fattahi, "Sub-10 fs, 45 W, 3 μJ pulses from a Yb:YAG thin-disk oscillator," in *Ultrafast Optics XII*, 2019.

Data Archiving

The experimental raw data, the data processing files, and the original figures can be found on the Data Archive Server of the Laboratory for Attosecond Physics at the Max Planck Institute of Quantum Optics: `//AFS/ipp-garching.mpg.de/mpq/lap/publication_archive`.

For each figure, the archived data can be found under the folder of corresponding chapter and the subfolder of the figure. The archived data include relevant files such as: the experimental raw data, MATLAB scripts for the data analysis in .m format, Python scripts for the data analysis in .ipynb or .py format, Origin projects in .opj format, and the figure in .pdf or .png format. An overview of the archived data structure is summarized in the following table.

folder	subfolder	content
Ch. 2	Fig. 2.1	plot (.pdf), simulation script (.py)
	Fig. 2.2	plot (.pdf), simulation script (.py)
	Fig. 2.3	plot (.pdf), simulation script (.py)
	Fig. 2.4	schematic (.pdf)
	Fig. 2.5	schematic (.pdf)
	Fig. 2.6	schematic (.pdf)
	Fig. 2.7	schematic (.pdf)
	Fig. 2.8	schematic (.png)
Ch. 3	Fig. 3.1	plot (.pdf), plotting script (.opj), original data
	Fig. 3.2	schematic (.pdf), reprint Contemporary Physics
	Fig. 3.3	schematic (.pdf)
	Fig. 3.4	schematic (.pdf)
	Fig. 3.5	plot (.pdf), analysis script (.m), original data
	Fig. 3.6	plot (.pdf), analysis script (.opj), original data
	Fig. 3.7	schematic (.pdf)
	Fig. 3.8	plot (.pdf), analysis script (.m), original data
	Fig. 3.9	plot (.pdf), analysis script (.ipynb), original data
	Fig. 3.10	plot (.pdf), analysis script (.m), original data
	Fig. 3.11	plot (.pdf), analysis script (.m, .ipynb), original data
	Fig. 3.12	schematic (.pdf)

	Fig. 3.13	plot (.pdf), analysis script (.m), original data
	Fig. 3.14	plot (.pdf), analysis script (.ipynb), original data
	Fig. 3.15	plot (.pdf), analysis script (.m), original data
	Fig. 3.16	plot (.pdf), analysis script (.m, .ipynb), original data
	Fig. 3.17	plot (.pdf), analysis script (.m), original data
	Fig. 3.18	plot (.pdf), analysis script (.ipynb), original data
	Fig. 3.19	plot (.pdf), analysis script (.ipynb), original data
	Fig. 3.20	plot (.pdf), analysis script (.m, .ipynb), original data
	Fig. 3.21	schematic (.pdf)
	Fig. 3.22	image (.png), original data
	Fig. 3.23	plot (.pdf), analysis script (.ipynb), original data
	Fig. 3.24	plot (.pdf), analysis script (.m), original data
	Fig. 3.25	plot (.pdf), analysis script (.m), original data
	Fig. 3.26	plot (.pdf), analysis script (.ipynb), original data
	Fig. 3.27	plot (.png), analysis script (.m), original data
	Fig. 3.28	schematic (.pdf)
	Fig. 3.29	plot (.pdf), analysis script (.m), original data
	Fig. 3.30	schematic (.pdf), plot (.png), analysis script (.ipynb), original data
	Fig. 3.31	schematic (.pdf)
	Fig. 3.32	plot (.pdf), analysis script (.m), original data
	Fig. 3.33	plot (.pdf), analysis script (.m), original data
	Fig. 3.34	plot (.pdf), analysis script (.m), original data
	Fig. 3.35	plot (.pdf), analysis script (.m), original data
	Fig. 3.36	plot (.pdf), analysis script (.m), original data
	Fig. 3.37	plot (.pdf), analysis script (.m), original data
	Fig. 3.38	plot (.pdf), analysis script (.m, .py), original data
	Fig. 3.39	plot (.pdf), analysis script (.m), original data
	Fig. 3.40	plot (.pdf), analysis script (.m), original data
Ch. 4	Fig. 4.1	schematic (.pdf)
	Fig. 4.2	plot (.pdf), analysis script (.m), original data
	Fig. 4.3	plot (.pdf), analysis script (.m), original data
	Fig. 4.4	plot (.pdf), analysis script (.m), original data
	Fig. 4.5	schematic (.pdf)
	Fig. 4.6	plot (.png)
	Fig. 4.7	plot (.pdf), analysis script (.ipynb), original data
	Fig. 4.8	plot (.pdf), analysis script (.ipynb), original data
	Fig. 4.9	plot (.pdf), analysis script (.ipynb), original data
	Fig. 4.10	plot (.pdf), analysis script (.m), original data
	Fig. 4.11	image (.png), schematic (.pdf)
	Fig. 4.12	plot (.pdf), analysis script (.ipynb), original data
	Fig. 4.13	plot (.pdf), analysis script (.ipynb), original data

Fig. 4.14	plot (.pdf), analysis script (.ipynb), original data
Fig. 4.15	schematic (.pdf)
Fig. 4.16	plot (.pdf), analysis script (.ipynb), original data

Bibliography

[1] Theodore H Maiman. Stimulated optical radiation in ruby. *nature*, 187(4736):493–494, 1960.

[2] Benjamin P Abbott, Rich Abbott, TD Abbott, Fausto Acernese, Kendall Ackley, Carl Adams, Thomas Adams, Paolo Addesso, RX Adhikari, VB Adya, et al. Gw170817: observation of gravitational waves from a binary neutron star inspiral. *Physical Review Letters*, 119(16):161101, 2017.

[3] Thomas Brabec and Ferenc Krausz. Intense few-cycle laser fields: Frontiers of nonlinear optics. *Reviews of Modern Physics*, 72(2):545, 2000.

[4] Ferenc Krausz and Misha Ivanov. Attosecond physics. *Reviews of Modern Physics*, 81(1):163, 2009.

[5] Ahmed H Zewail. Femtochemistry: Atomic-scale dynamics of the chemical bond. *The Journal of Physical Chemistry A*, 104(24):5660–5694, 2000.

[6] Villy Sundström. Femtobiology. *Annu. Rev. Phys. Chem.*, 59:53–77, 2008.

[7] W Sibbett, AA Lagatsky, and CTA Brown. The development and application of femtosecond laser systems. *Optics Express*, 20(7):6989–7001, 2012.

[8] Peter F Moulton. Spectroscopic and laser characteristics of Ti:Al_2O_3. *JOSA B*, 3(1):125–133, 1986.

[9] David E Spence, P Np Kean, and Wilson Sibbett. 60-fsec pulse generation from a self-mode-locked ti:sapphire laser. *Optics letters*, 16(1):42–44, 1991.

[10] Robert Szipöcs, Kárpát Ferencz, Christian Spielmann, and Ferenc Krausz. Chirped multilayer coatings for broadband dispersion control in femtosecond lasers. *Optics letters*, 19(3):201–203, 1994.

[11] A Stingl, M Lenzner, Ch Spielmann, F Krausz, and R Szipöcs. Sub-10-fs mirror-dispersion-controlled Ti:sapphire laser. *Optics letters*, 20(6):602–604, 1995.

[12] Axel Kasper and Klaus-Juergen Witte. 10-fs pulse generation from a unidirectional kerr-lens mode-locked Ti: sapphire ring laser. *Optics letters*, 21(5):360–362, 1996.

[13] Donna Strickland and Gerard Mourou. Compression of amplified chirped optical pulses. *Optics communications*, 56(3):219–221, 1985.

[14] Lin Xu, Ch Spielmann, A Poppe, T Brabec, Ferenc Krausz, and TW Hänsch. Route to phase control of ultrashort light pulses. *Optics letters*, 21(24):2008–2010, 1996.

[15] Samuel Bohman, Akira Suda, Tsuneto Kanai, Shigeru Yamaguchi, and Katsumi Midorikawa. Generation of 5.0 fs, 5.0 mJ pulses at 1 kHz using hollow-fiber pulse compression. *Optics letters*, 35(11):1887–1889, 2010.

[16] Wolfgang Schweinberger, Annkatrin Sommer, Elisabeth Bothschafter, Jiang Li, Ferenc Krausz, Reinhard Kienberger, and Martin Schultze. Waveform-controlled near-single-cycle milli-joule laser pulses generate sub-10 nm extreme ultraviolet continua. *Optics letters*, 37(17):3573–3575, 2012.

[17] Adrian Wirth, M Th Hassan, Ivanka Grguraš, Justin Gagnon, Antoine Moulet, Tran Trung Luu, S Pabst, R Santra, ZA Alahmed, AM Azzeer, et al. Synthesized light transients. *Science*, page 1210268, 2011.

[18] Guenter Huber, Christian Kränkel, and Klaus Petermann. Solid-state lasers: status and future. *JOSA B*, 27(11):B93–B105, 2010.

[19] Joerg Koerner, Christian Vorholt, Hartmut Liebetrau, Martin Kahle, Diethard Kloepfel, Reinhard Seifert, Joachim Hein, and Malte C Kaluza. Measurement of temperature-dependent absorption and emission spectra of Yb:YAG, Yb:LuAG, and Yb:CaF 2 between 20°C and 200°C and predictions on their influence on laser performance. *JOSA B*, 29(9):2493–2502, 2012.

[20] Thomas Nubbemeyer, Martin Kaumanns, Moritz Ueffing, Martin Gorjan, Ayman Alismail, Hanieh Fattahi, Jonathan Brons, Oleg Pronin, Helena G Barros, Zsuzsanna Major, et al. 1 kW, 200 mJ picosecond thin-disk laser system. *Optics Letters*, 42(7):1381–1384, 2017.

[21] Hanieh Fattahi, Helena G Barros, Martin Gorjan, Thomas Nubbemeyer, Bidoor Alsaif, Catherine Y Teisset, Marcel Schultze, Stephan Prinz, Matthias Haefner, Moritz Ueffing, et al. Third-generation femtosecond technology. *Optica*, 1(1):45–63, 2014.

[22] Haochuan Wang, Ayman Alismail, Gaia Barbiero, Raja Naeem Ahmad, and Hanieh Fattahi. High Energy, Sub-Cycle, Field Synthesizers. *IEEE Journal of Selected Topics in Quantum Electronics*, 25(4):1–12, 2019.

[23] Maximilian Wendl, Maximilian Högner, and Hanieh Fattahi. Theoretical Study: High Harmonic Generation by Light Transients. *Applied Sciences*, 8(5):7281–7292, may 2018.

[24] Tenio Popmintchev, Ming-Chang Chen, Dimitar Popmintchev, Paul Arpin, Susannah Brown, Skirmantas Ališauskas, Giedrius Andriukaitis, Tadas Balčiunas, Oliver D Mücke, Audrius Pugzlys, et al. Bright coherent ultrahigh harmonics in the kev x-ray regime from mid-infrared femtosecond lasers. *science*, 336(6086):1287–1291, 2012.

[25] Ioachim Pupeza, Marinus Huber, Michael Trubetskov, Wolfgang Schweinberger, Syed A Hussain, Christina Hofer, Kilian Fritsch, Markus Poetzlberger, Lenard Vamos, Ernst Fill, et al. Field-resolved infrared spectroscopy of biological systems. *Nature*, 577(7788):52–59, 2020.

[26] Jonathan Brons, Vladimir Pervak, Dominik Bauer, Dirk Sutter, Oleg Pronin, and Ferenc Krausz. Powerful 100-fs-scale Kerr-lens mode-locked thin-disk oscillator. *Optics Letters*, 41(15):3567–3570, 2016.

[27] Mauro Nisoli, Sandro De Silvestri, Orazio Svelto, R Szipöcs, K Ferencz, Ch Spielmann, S Sartania, and Ferenc Krausz. Compression of high-energy laser pulses below 5 fs. *Optics letters*, 22(8):522–524, 1997.

[28] CP Hauri, W Kornelis, FW Helbing, A Heinrich, Arnaud Couairon, André Mysyrowicz, Jens Biegert, and Ursulla Keller. Generation of intense, carrier-envelope phase-locked few-cycle laser pulses through filamentation. *Applied Physics B*, 79(6):673–677, 2004.

[29] O Pronin, Marcus Seidel, F Lücking, J Brons, E Fedulova, M Trubetskov, V Pervak, A Apolonski, Th Udem, and Ferenc Krausz. High-power multi-megahertz source of waveform-stabilized few-cycle light. *Nature communications*, 6:6988, 2015.

[30] Ioachim Pupeza, D Sánchez, Jinwei Zhang, Nicolai Lilienfein, Marcus Seidel, Nicholas Karpowicz, T Paasch-Colberg, Irina Znakovskaya, M Pescher, W Schweinberger, et al. High-power sub-two-cycle mid-infrared pulses at 100 MHz repetition rate. *Nature Photonics*, 9(11):721, 2015.

[31] Christoph Jocher, Tino Eidam, Steffen Hädrich, Jens Limpert, and Andreas Tünnermann. Sub 25 fs pulses from solid-core nonlinear compression stage at 250 W of average power. *Optics letters*, 37(21):4407–4409, 2012.

[32] Florian Emaury, Clara J Saraceno, Benoit Debord, Debashri Ghosh, Andreas Diebold, Frederic Gèrôme, Thomas Südmeyer, Fetah Benabid, and Ursula Keller.

Efficient spectral broadening in the 100-W average power regime using gas-filled kagome HC-PCF and pulse compression. *Optics Letters*, 39(24):6843–6846, 2014.

[33] Steffen Hädrich, Manuel Krebs, Armin Hoffmann, Arno Klenke, Jan Rothhardt, Jens Limpert, and Andreas Tünnermann. Exploring new avenues in high repetition rate table-top coherent extreme ultraviolet sources. *Light: Science & Applications*, 4(8):e320–e320, 2015.

[34] Mauro Nisoli, Sandro De Silvestri, and Orazio Svelto. Generation of high energy 10 fs pulses by a new pulse compression technique. *Applied Physics Letters*, 68(20):2793–2795, 1996.

[35] Steffen Hädrich, Marco Kienel, Michael Müller, Arno Klenke, Jan Rothhardt, Robert Klas, Thomas Gottschall, Tino Eidam, András Drozdy, Péter Jójárt, et al. Energetic sub-2-cycle laser with 216 W average power. *Optics letters*, 41(18):4332–4335, 2016.

[36] Jan Schulte, Thomas Sartorius, Johannes Weitenberg, Andreas Vernaleken, and Peter Russbueldt. Nonlinear pulse compression in a multi-pass cell. *Optics Letters*, 41(19):4511–4514, 2016.

[37] Johannes Weitenberg, Andreas Vernaleken, Jan Schulte, Akira Ozawa, Thomas Sartorius, Vladimir Pervak, Hans-Dieter Hoffmann, Thomas Udem, Peter Russbüldt, and Theodor W Hänsch. Multi-pass-cell-based nonlinear pulse compression to 115 fs at 7.5 μJ pulse energy and 300 W average power. *Optics express*, 25(17):20502–20510, 2017.

[38] Moritz Ueffing, Simon Reiger, Martin Kaumanns, Vladimir Pervak, Michael Trubetskov, Thomas Nubbemeyer, and Ferenc Krausz. Nonlinear pulse compression in a gas-filled multipass cell. *Optics letters*, 43(9):2070–2073, 2018.

[39] Kilian Fritsch, Markus Poetzlberger, Vladimir Pervak, Jonathan Brons, and Oleg Pronin. All-solid-state multipass spectral broadening to sub-20 fs. *Optics letters*, 43(19):4643–4646, 2018.

[40] Gaia Barbiero, Raja N Ahmad, Haochuan Wang, Felix Köttig, David Novoa, Francesco Tani, Jonathan Brons, Philip St J Russell, Ferenc Krausz, and Hanieh Fattahi. Towards 45 watt single-cycle pulses from Yb:YAG thin-disk oscillators. In *2019 Conference on Lasers and Electro-Optics Europe & European Quantum Electronics Conference (CLEO/Europe-EQEC)*, pages 1–1. IEEE, 2019.

[41] Raja Naeem Ahmad. Towards generation of single-cycle high power laser pulses. Master's thesis, Ludwig–Maximilians–Universität München, 2019.

[42] Robert W Boyd. *Nonlinear optics*. Elsevier, 2008.

[43] Richard L Sutherland. *Handbook of nonlinear optics*. CRC press, 2003.

[44] Franz X Kärtner. *Few-cycle laser pulse generation and its applications*, volume 95. Springer Science & Business Media, 2004.

[45] Cristian Manzoni and Giulio Cerullo. Design criteria for ultrafast optical parametric amplifiers. *Journal of Optics*, 18(10):103501, 2016.

[46] Andrew Weiner. *Ultrafast optics*, volume 72. John Wiley & Sons, 2011.

[47] Jean-Claude Diels and Wolfgang Rudolph. *Ultrashort laser pulse phenomena*. Elsevier, 2006.

[48] G Herziger, H Weber, and R Poprawe. *Laser Physics and Applications*. Springer, 2007.

[49] Rick Trebino. *Frequency-resolved optical gating: the measurement of ultrashort laser pulses*. Springer Science & Business Media, 2012.

[50] Andrius Baltuška, Takao Fuji, and Takayoshi Kobayashi. Controlling the carrier-envelope phase of ultrashort light pulses with optical parametric amplifiers. *Physical review letters*, 88(13):133901, 2002.

[51] David J Jones, Scott A Diddams, Jinendra K Ranka, Andrew Stentz, Robert S Windeler, John L Hall, and Steven T Cundiff. Carrier-envelope phase control of femtosecond mode-locked lasers and direct optical frequency synthesis. *Science*, 288(5466):635–639, 2000.

[52] Steven T Cundiff and Jun Ye. Colloquium: Femtosecond optical frequency combs. *Reviews of Modern Physics*, 75(1):325, 2003.

[53] Ayman Alismail, Haochuan Wang, Gaia Barbiero, Najd Altwaijry, Syed Ali Hussain, Volodymyr Pervak, Wolfgang Schweinberger, Abdallah M. Azzeer, Ferenc Krausz, and Hanieh Fattahi. Multi-octave, cep-stable source for high-energy field synthesis. *Science Advances*, 6(7):eaax3408, 2020.

[54] Gaia Barbiero, Haochuan Wang, Jonathan Brons, Bo-Han Chen, Vladimir Pervak, and Hanieh Fattahi. Broadband terahertz solid-state emitter driven by Yb:YAG thin-disk oscillator. *Journal of Physics B: Atomic, Molecular and Optical Physics*, 53(12):125601, 2020.

[55] A Apolonski, A Poppe, G Tempea, Ch Spielmann, Th Udem, RHTW Holzwarth, Theodor W Hänsch, and Ferenc Krausz. Controlling the phase evolution of few-cycle light pulses. *Physical Review Letters*, 85(4):740, 2000.

[56] Sebastian Gröbmeyer, Jonathan Brons, Marcus Seidel, and Oleg Pronin. Carrier-envelope-offset frequency stable 100 w-level femtosecond thin-disk oscillator. *Laser & Photonics Reviews*, 13(3):1800256, 2019.

[57] Antoine Monmayrant, Sébastien Weber, and Béatrice Chatel. A newcomer's guide to ultrashort pulse shaping and characterization. *Journal of Physics B: Atomic, Molecular and Optical Physics*, 43(10):103001, 2010.

[58] Audrius Dubietis, G Tamošauskas, R Šuminas, Vytautas Jukna, and Arnaud Couairon. Ultrafast supercontinuum generation in bulk condensed media. *Lithuanian Journal of Physics*, 57(3):113–157, 2017.

[59] N Minkovski, GI Petrov, SM Saltiel, O Albert, and J Etchepare. Nonlinear polarization rotation and orthogonal polarization generation experienced in a single-beam configuration. *JOSA B*, 21(9):1659–1664, 2004.

[60] Theresa Buberl, Ayman Alismail, Haochuan Wang, Nicholas Karpowicz, and Hanieh Fattahi. Self-compressed, spectral broadening of a Yb:YAG thin-disk amplifier. *Optics express*, 24(10):10286–10294, 2016.

[61] K Osvay, L Canova, C Durfee, AP Kovács, Á Börzsönyi, O Albert, and R Lopez Martens. Preservation of the carrier envelope phase in generation of cross polarized wave. In *Conference on Lasers and Electro-Optics*, page JTuD39. Optical Society of America, 2009.

[62] Lorenzo Canova, Stoyan Kourtev, Nikolay Minkovski, Aurélie Jullien, Rodrigo Lopez-Martens, Olivier Albert, and Solomon M Saltiel. Efficient generation of cross-polarized femtosecond pulses in cubic crystals with holographic cut orientation. *Applied Physics Letters*, 92(23):231102, 2008.

[63] Arnaud Cotel, A Jullien, N Forget, O Albert, Gilles Cheriaux, and C Le Blanc. Nonlinear temporal pulse cleaning of a 1-μm optical parametric chirped-pulse amplification system. *Applied Physics B*, 83(1):7–10, 2006.

[64] U Keller. Ultrafast all-solid-state laser technology. *Applied Physics B*, 58(5):347–363, 1994.

[65] Ursula Keller, Kurt J Weingarten, Franz X Kartner, Daniel Kopf, Bernd Braun, Isabella D Jung, Regula Fluck, Clemens Honninger, Nicolai Matuschek, and J Aus

Der Au. Semiconductor saturable absorber mirrors (sesam's) for femtosecond to nanosecond pulse generation in solid-state lasers. *IEEE Journal of selected topics in QUANTUM ELECTRONICS*, 2(3):435–453, 1996.

[66] KF Mak, Marcus Seidel, O Pronin, MH Frosz, A Abdolvand, V Pervak, A Apolonski, Ferenc Krausz, JC Travers, and P St J Russell. Compressing μj-level pulses from 250 fs to sub-10 fs at 38-mhz repetition rate using two gas-filled hollow-core photonic crystal fiber stages. *Optics letters*, 40(7):1238–1241, 2015.

[67] OE Martinez, JP Gordon, and RL Fork. Negative group-velocity dispersion using refraction. *JOSA A*, 1(10):1003–1006, 1984.

[68] O Martinez. 3000 times grating compressor with positive group velocity dispersion: Application to fiber compensation in 1.3-1.6 μm region. *IEEE Journal of Quantum Electronics*, 23(1):59–64, 1987.

[69] Marcus Seidel, Gunnar Arisholm, Jonathan Brons, Vladimir Pervak, and Oleg Pronin. All solid-state spectral broadening: an average and peak power scalable method for compression of ultrashort pulses. *Optics express*, 24(9):9412–9428, 2016.

[70] Bo-Han Chen, Martin Kretschmar, Dominik Ehberger, Andreas Blumenstein, Peter Simon, Peter Baum, and Tamas Nagy. Compression of picosecond pulses from a thin-disk laser to 30fs at 4w average power. *Optics express*, 26(4):3861–3869, 2018.

[71] Annkatrin Sommer, EM Bothschafter, SA Sato, Clemens Jakubeit, Tobias Latka, Olga Razskazovskaya, Hanieh Fattahi, Michael Jobst, W Schweinberger, Vage Shirvanyan, et al. Attosecond nonlinear polarization and light–matter energy transfer in solids. *Nature*, 534(7605):86, 2016.

[72] Yunpei Deng, Alexander Schwarz, Hanieh Fattahi, Moritz Ueffing, Xun Gu, Marcus Ossiander, Thomas Metzger, Volodymyr Pervak, Hideki Ishizuki, Takunori Taira, et al. Carrier-envelope-phase-stable, 1.2 mJ, 1.5 cycle laser pulses at 2.1 μm. *Optics letters*, 37(23):4973–4975, 2012.

[73] Nicolas Bigler, Justinas Pupeikis, Stefan Hrisafov, L Gallmann, Christopher R Phillips, and Ursula Keller. High-power OPCPA generating 1.7 cycle pulses at 2.5 μm. *Optics express*, 26(20):26750–26757, 2018.

[74] Kyung-Han Hong, Chien-Jen Lai, Jonathas Siqueira, Peter Krogen, Jeffrey Moses, Martin Smrz, Luis E Zapata, and Franz X Kärtner. Multi-mJ, kHz, 2.1-μm OPCPA for high-flux soft X-ray high-harmonic radiation. In *Quantum Information and Measurement*, pages JW2A–5. Optical Society of America, 2014.

[75] Yanchun Yin, Jie Li, Xiaoming Ren, Kun Zhao, Yi Wu, Eric Cunningham, and Zenghu Chang. High-efficiency optical parametric chirped-pulse amplifier in BiB_3O_6 for generation of 3 mJ, two-cycle, carrier-envelope-phase-stable pulses at 1.7 μm. *Optics letters*, 41(6):1142–1145, 2016.

[76] M Neuhaus, Harald Fuest, M Seeger, Johannes Schötz, M Trubetskov, P Russbueldt, HD Hoffmann, Eberhard Riedle, Zs Major, Vladimir Pervak, et al. 10 W CEP-stable few-cycle source at 2 μm with 100 kHz repetition rate. *Optics express*, 26(13):16074–16085, 2018.

[77] A Dubietis, G Jonušauskas, and A Piskarskas. Powerful femtosecond pulse generation by chirped and stretched pulse parametric amplification in BBO crystal. *Optics Communications*, 88(4-6):437–440, 1992.

[78] Audrius Dubietis, Rytis Butkus, and Algis Petras Piskarskas. Trends in chirped pulse optical parametric amplification. *IEEE Journal of selected topics in quantum electronics*, 12(2):163–172, 2006.

[79] Cristian Manzoni, Oliver D Mücke, Giovanni Cirmi, Shaobo Fang, Jeffrey Moses, Shu-Wei Huang, Kyung-Han Hong, Giulio Cerullo, and Franz X Kärtner. Coherent pulse synthesis: towards sub-cycle optical waveforms. *Laser & Photonics Reviews*, 9(2):129–171, 2015.

[80] Valentin G Dmitriev, Gagik G Gurzadyan, and David N Nikogosyan. *Handbook of nonlinear optical crystals*, volume 64. Springer, 2013.

[81] David S Hum and Martin M Fejer. Quasi-phasematching. *Comptes Rendus Physique*, 8(2):180–198, 2007.

[82] Giulio Cerullo, Mauro Nisoli, Salvatore Stagira, and SANDRO De Silvestri. Sub-8-fs pulses from an ultrabroadband optical parametric amplifier in the visible. *Optics letters*, 23(16):1283–1285, 1998.

[83] Bruno E Schmidt, Nicolas Thiré, Maxime Boivin, Antoine Laramée, Francois Poitras, Guy Lebrun, Tsuneyuki Ozaki, Heide Ibrahim, and Francois Légaré. Frequency domain optical parametric amplification. *Nature communications*, 5(1):1–8, 2014.

[84] M Baudrier-Raybaut, R Haidar, Ph Kupecek, Ph Lemasson, and E Rosencher. Random quasi-phase-matching in bulk polycrystalline isotropic nonlinear materials. *Nature*, 432(7015):374, 2004.

[85] Jinwei Zhang, Kilian Fritsch, Qing Wang, Ferenc Krausz, Ka Fai Mak, and Oleg Pronin. Intra-pulse difference-frequency generation of mid-infrared (2.7–20 μm) by random quasi-phase-matching. *Optics letters*, 44(12):2986–2989, 2019.

[86] TW Hänsch. A proposed sub-femtosecond pulse synthesizer using separate phase-locked laser oscillators. *Optics Communications*, 80(1):71–75, 1990.

[87] SE Harris and AV Sokolov. Subfemtosecond pulse generation by molecular modulation. *Physical review letters*, 81(14):2894, 1998.

[88] Han-Sung Chan, Zhi-Ming Hsieh, Wei-Hong Liang, AH Kung, Chao-Kuei Lee, Chien-Jen Lai, Ru-Pin Pan, and Lung-Han Peng. Synthesis and measurement of ultrafast waveforms from five discrete optical harmonics. *Science*, 331(6021):1165–1168, 2011.

[89] Robert K Shelton, Long-Sheng Ma, Henry C Kapteyn, Margaret M Murnane, John L Hall, and Jun Ye. Phase-coherent optical pulse synthesis from separate femtosecond lasers. *Science*, 293(5533):1286–1289, 2001.

[90] Günther Krauss, Sebastian Lohss, Tobias Hanke, Alexander Sell, Stefan Eggert, Rupert Huber, and Alfred Leitenstorfer. Synthesis of a single cycle of light with compact erbium-doped fibre technology. *Nature photonics*, 4(1):33, 2010.

[91] Stefan Rausch, Thomas Binhammer, Anne Harth, Franz X Kärtner, and Uwe Morgner. Few-cycle femtosecond field synthesizer. *Optics express*, 16(22):17410–17419, 2008.

[92] Cristian Manzoni, S-W Huang, Giovanni Cirmi, Paolo Farinello, Jeffrey Moses, FX Kärtner, and G Cerullo. Coherent synthesis of ultra-broadband optical parametric amplifiers. *Optics letters*, 37(11):1880–1882, 2012.

[93] Oliver D Mucke, Shaobo Fang, Giovanni Cirmi, Giulio Maria Rossi, Shih-Hsuan Chia, Hong Ye, Yudong Yang, Roland Mainz, Cristian Manzoni, Paolo Farinello, et al. Toward waveform nonlinear optics using multimillijoule sub-cycle waveform synthesizers. *IEEE J. Sel. Top. Quantum Electron.*, 21(5):1–12, 2015.

[94] Edmond Treacy. Optical pulse compression with diffraction gratings. *IEEE Journal of quantum Electronics*, 5(9):454–458, 1969.

[95] Olga Razskazovskaya, Ferenc Krausz, and V Pervak. Multilayer coatings for femto- and attosecond technology. *Optica*, 4(1):129–138, 2017.

[96] Andrew M Weiner, Daniel E Leaird, JS Patel, and John R Wullert. Programmable shaping of femtosecond optical pulses by use of 128-element liquid crystal phase modulator. *IEEE Journal of Quantum Electronics*, 28(4):908–920, 1992.

[97] Steven T Cundiff and Andrew M Weiner. Optical arbitrary waveform generation. *Nature Photonics*, 4(11):760, 2010.

[98] Frederic Verluise, Vincent Laude, Z Cheng, Ch Spielmann, and Pierre Tournois. Amplitude and phase control of ultrashort pulses by use of an acousto-optic programmable dispersive filter: pulse compression and shaping. *Optics letters*, 25(8):575–577, 2000.

[99] M Th Hassan, Adrian Wirth, Ivanka Grguraš, Antoine Moulet, Tran Trung Luu, Justin Gagnon, Volodymyr Pervak, and Eleftherios Goulielmakis. Invited article: attosecond photonics: synthesis and control of light transients. *Review of scientific instruments*, 83(11):111301, 2012.

[100] Tran Trung Luu, M Garg, S Yu Kruchinin, Antoine Moulet, M Th Hassan, and Eleftherios Goulielmakis. Extreme ultraviolet high-harmonic spectroscopy of solids. *Nature*, 521(7553):498–502, 2015.

[101] M Th Hassan, Tran Trung Luu, Antoine Moulet, O Raskazovskaya, P Zhokhov, Manish Garg, Nicholas Karpowicz, AM Zheltikov, V Pervak, Ferenc Krausz, et al. Optical attosecond pulses and tracking the nonlinear response of bound electrons. *Nature*, 530(7588):66–70, 2016.

[102] Oliver H Heckl, Jochen Kleinbauer, Dominik Bauer, Sascha Weiler, Thomas Metzger, and Dirk H Sutter. Ultrafast thin-disk lasers. In *Ultrashort Pulse Laser Technology*, pages 93–115. Springer, 2016.

[103] Luis E Zapata, Hua Lin, Anne-Laure Calendron, Huseyin Cankaya, Michael Hemmer, Fabian Reichert, W Ronny Huang, Eduardo Granados, Kyung-Han Hong, and Franz X Kärtner. Cryogenic Yb:YAG composite-thin-disk for high energy and average power amplifiers. *Optics letters*, 40(11):2610–2613, 2015.

[104] M Schulz, R Riedel, A Willner, T Mans, C Schnitzler, P Russbueldt, J Dolkemeyer, E Seise, T Gottschall, S Hädrich, et al. Yb: YAG Innoslab amplifier: efficient high repetition rate subpicosecond pumping system for optical parametric chirped pulse amplification. *Optics letters*, 36(13):2456–2458, 2011.

[105] F Röser, T Eidam, J Rothhardt, O Schmidt, DN Schimpf, J Limpert, and A Tünnermann. Millijoule pulse energy high repetition rate femtosecond fiber chirped-pulse amplification system. *Optics letters*, 32(24):3495–3497, 2007.

[106] P Russbueldt, T Mans, G Rotarius, J Weitenberg, HD Hoffmann, and R Poprawe. 400 W Yb: YAG Innoslab fs-amplifier. *Optics express*, 17(15):12230–12245, 2009.

[107] Cory Baumgarten, Michael Pedicone, Herman Bravo, Hanchen Wang, Liang Yin, Carmen S Menoni, Jorge J Rocca, and Brendan A Reagan. 1 J, 0.5 kHz repetition rate picosecond laser. *Optics Letters*, 41(14):3339–3342, 2016.

[108] Bruno E Schmidt, Arvid Hage, Torsten Mans, François Légaré, and Hans Jakob Wörner. Highly stable, 54 mJ Yb-InnoSlab laser platform at 0.5 kW average power. *Optics Express*, 25(15):17549–17555, 2017.

[109] P Russbueldt, T Mans, J Weitenberg, HD Hoffmann, and R Poprawe. Compact diode-pumped 1.1 kW Yb:YAG Innoslab femtosecond amplifier. *Optics letters*, 35(24):4169–4171, 2010.

[110] Michele Puppin, Yunpei Deng, Oliver Prochnow, Jan Ahrens, Thomas Binhammer, Uwe Morgner, Marcel Krenz, Martin Wolf, and Ralph Ernstorfer. 500 kHz OPCPA delivering tunable sub-20 fs pulses with 15 W average power based on an all-ytterbium laser. *Optics express*, 23(2):1491–1497, 2015.

[111] Vesna Markovic, Andreas Rohrbacher, Peter Hofmann, Wolfgang Pallmann, Simonette Pierrot, and Bojan Resan. 160 W 800 fs Yb:YAG single crystal fiber amplifier without CPA. *Optics express*, 23(20):25883–25888, 2015.

[112] Xavier Délen, Yoann Zaouter, Igor Martial, Nicolas Aubry, Julien Didierjean, Clemens Hönninger, Eric Mottay, François Balembois, and Patrick Georges. Yb:YAG single crystal fiber power amplifier for femtosecond sources. *Optics letters*, 38(2):109–111, 2013.

[113] Fabien Lesparre, Jean Thomas Gomes, Xavier Délen, Igor Martial, Julien Didierjean, Wolfgang Pallmann, Bojan Resan, Frederic Druon, François Balembois, and Patrick Georges. Yb:YAG single-crystal fiber amplifiers for picosecond lasers using the divided pulse amplification technique. *Optics letters*, 41(7):1628–1631, 2016.

[114] Jan Rothhardt, Carolin Rothhardt, Michael Müller, Arno Klenke, Marco Kienel, Stefan Demmler, Tino Elsmann, Manfred Rothhardt, Jens Limpert, and Andreas Tünnermann. 100 W average power femtosecond laser at 343 nm. *Optics letters*, 41(8):1885–1888, 2016.

[115] Shigeki Tokita, Junji Kawanaka, Yasukazu Izawa, Masayuki Fujita, and Toshiyuki Kawashima. 23.7-W picosecond cryogenic-Yb:YAG multipass amplifier. *Optics express*, 15(7):3955–3961, 2007.

[116] Kyung-Han Hong, Aleem Siddiqui, Jeffrey Moses, Juliet Gopinath, John Hybl, F Ömer Ilday, Tso Yee Fan, and Franz X Kärtner. Generation of 287 W, 5.5 ps pulses at 78 MHz repetition rate from a cryogenically cooled Yb:YAG amplifier seeded by a fiber chirped-pulse amplification system. *Optics letters*, 33(21):2473–2475, 2008.

[117] Kyung-Han Hong, Juliet T Gopinath, Darren Rand, Aleem M Siddiqui, Shu-Wei Huang, Enbang Li, Benjamin J Eggleton, John D Hybl, Tso Yee Fan, and Franz X

Kärtner. High-energy, kHz-repetition-rate, ps cryogenic Yb:YAG chirped-pulse amplifier. *Optics letters*, 35(11):1752–1754, 2010.

[118] Luis E Zapata, F Reichert, M Hemmer, and FX Kärtner. 250 W average power, 100 kHz repetition rate cryogenic Yb:YAG amplifier for OPCPA pumping. *Optics letters*, 41(3):492–495, 2016.

[119] David C Brown, Joseph M Singley, Katie Kowalewski, James Guelzow, and Victoria Vitali. High sustained average power cw and ultrafast Yb:YAG near-diffraction-limited cryogenic solid-state laser. *Optics express*, 18(24):24770–24792, 2010.

[120] Brendan A Reagan, Cory Bamgarten, Keith Wernsing, Herman Bravo, Mark Woolston, Alden Curtis, Federico J Furch, Bradley M Luther, Dinesh Patel, Carmen S Menoni, et al. 1 Joule, 100 Hz repetition rate, picosecond CPA laser for driving high average power soft x-ray lasers. In *CLEO: Science and Innovations*, pages SM1F–4. Optical Society of America, 2014.

[121] Michael Hemmer, F Reichert, K Zapata, M Smrz, A-L Calendron, H ankaya, KH Hong, F Kärtner, and L Zapata. Picosecond, 115 mJ energy, 200 Hz repetition rate cryogenic Yb:YAG bulk-amplifier. In *CLEO: Science and Innovations*, pages STu4O–3. Optical Society of America, 2015.

[122] JM Smith, TJ Butcher, PD Mason, K Ertel, PJ Phillips, S Banerjee, M De Vido, O Chekhlov, M Divoky, J Pilar, et al. 100J-level nanosecond pulsed Yb:YAG cryo-cooled DPSSL amplifier. In *Solid State Lasers XXVII: Technology and Devices*, volume 10511, page 105110T. International Society for Optics and Photonics, 2018.

[123] Chun-Lin Chang, Peter Krogen, Kyung-Han Hong, Luis E Zapata, Jeffrey Moses, Anne-Laure Calendron, Houkun Liang, Chien-Jen Lai, Gregory J Stein, Phillip D Keathley, et al. High-energy, kHz, picosecond hybrid Yb-doped chirped-pulse amplifier. *Optics express*, 23(8):10132–10144, 2015.

[124] Thomas Metzger, Alexander Schwarz, Catherine Yuriko Teisset, Dirk Sutter, Alexander Killi, Reinhard Kienberger, and Ferenc Krausz. High-repetition-rate picosecond pump laser based on a yb:yag disk amplifier for optical parametric amplification. *Optics letters*, 34(14):2123–2125, 2009.

[125] Oleg Pronin, Jonathan Brons, Christian Grasse, Vladimir Pervak, Gerhard Boehm, M-C Amann, Vladimir L Kalashnikov, Alexander Apolonski, and Ferenc Krausz. High-power 200 fs Kerr-lens mode-locked Yb: YAG thin-disk oscillator. *Optics letters*, 36(24):4746–4748, 2011.

[126] Jakub Novák, Jonathan T Green, Thomas Metzger, Tomáš Mazanec, Bedřich Himmel, Martin Horáček, Zbyněk Hubka, Robert Boge, Roman Antipenkov, František Batysta, et al. Thin disk amplifier-based 40 mJ, 1 kHz, picosecond laser at 515 nm. *Optics express*, 24(6):5728–5733, 2016.

[127] František Batysta, Roman Antipenkov, Jakub Novák, Jonathan T Green, Jack A Naylon, Jakub Horáček, Martin Horáček, Zbyněk Hubka, Robert Boge, Tomáš Mazanec, et al. Broadband OPCPA system with 11 mJ output at 1 kHz, compressible to 12 fs. *Optics express*, 24(16):17843–17848, 2016.

[128] Stephan Prinz, Maximilian Schnitzenbaumer, Dionysios Potamianos, Marcel Schultze, Sebastian Stark, Matthias Häfner, Catherine Y Teisset, Christoph Wandt, Knut Michel, Reinhard Kienberger, et al. Thin-disk pumped optical parametric chirped pulse amplifier delivering CEP-stable multi-mJ few-cycle pulses at 6 kHz. *Optics express*, 26(2):1108–1124, 2018.

[129] Jan-Philipp Negel, André Loescher, Andreas Voss, Dominik Bauer, Dirk Sutter, Alexander Killi, Marwan Abdou Ahmed, and Thomas Graf. Ultrafast thin-disk multipass laser amplifier delivering 1.4 kW (4.7 mJ, 1030 nm) average power converted to 820 W at 515 nm and 234 W at 343 nm. *Optics express*, 23(16):21064–21077, 2015.

[130] Robert Jung, Johannes Tümmler, and Ingo Will. Regenerative thin-disk amplifier for 300 mJ pulse energy. *Optics express*, 24(2):883–887, 2016.

[131] Dominik Bauer, Ivo Zawischa, Dirk H Sutter, Alexander Killi, and Thomas Dekorsy. Mode-locked Yb:YAG thin-disk oscillator with 41 μJ pulse energy at 145 W average infrared power and high power frequency conversion. *Optics express*, 20(9):9698–9704, 2012.

[132] SV Marchese, CRE Baer, AG Engqvist, S Hashimoto, DJHC Maas, M Golling, T Südmeyer, and U Keller. Femtosecond thin disk laser oscillator with pulse energy beyond the 10-microjoule level. *Optics Express*, 16(9):6397–6407, 2008.

[133] Sergio V Marchese, Thomas Südmeyer, Matthias Golling, Rachel Grange, and Ursula Keller. Pulse energy scaling to 5 μJ from a femtosecond thin disk laser. *Optics letters*, 31(18):2728–2730, 2006.

[134] Frieder Beirow, Michael Eckerle, Benjamin Dannecker, Tom Dietrich, Marwan Abdou Ahmed, and Thomas Graf. Radially polarized passively mode-locked thin-disk laser oscillator emitting sub-picosecond pulses with an average output power exceeding the 100 W level. *Optics express*, 26(4):4401–4410, 2018.

[135] Waldemar Schneider, Andrey Ryabov, Cs Lombosi, Tom Metzger, Zs Major, József A Fülöp, and Peter Baum. 800-fs, 330-μJ pulses from a 100-W regenerative Yb:YAG thin-disk amplifier at 300 kHz and THz generation in $LiNbO_3$. *Optics letters*, 39(23):6604–6607, 2014.

[136] Hanieh Fattahi, Haochuan Wang, Ayman Alismail, Gunnar Arisholm, Vladimir Pervak, Abdallah M Azzeer, and Ferenc Krausz. Near-PHz-bandwidth, phase-stable continua generated from a Yb:YAG thin-disk amplifier. *Optics express*, 24(21):24337–24346, 2016.

[137] Moritz Ueffing, Robert Lange, Tobias Pleyer, Vladimir Pervak, Thomas Metzger, Dirk Sutter, Zsuzsanna Major, Thomas Nubbemeyer, and Ferenc Krausz. Direct regenerative amplification of femtosecond pulses to the multimillijoule level. *Optics letters*, 41(16):3840–3843, 2016.

[138] Robert Jung, Johannes Tümmler, Thomas Nubbemeyer, and Ingo Will. Thin-disk ring amplifier for high pulse energy. *Optics express*, 24(5):4375–4381, 2016.

[139] Luis E Zapata, Simon Schweisthal, Jelto Thesinga, Collette Zapata, Matthias Schust, Liu Yizhou, Mikhail Pergament, and Franz X Kaertner. Joule-class 500 Hz Cryogenic Yb:YAG Chirped Pulse Amplifier. In *CLEO: Science and Innovations*, pages SM4E–1. Optical Society of America, 2019.

[140] Catherine Teisset, Marcel Schultze, Robert Bessing, Matthias Häfner, Jens Rauschenberger, Dirk Sutter, and Thomas Metzger. Picosecond thin-disk regenerative amplifier with high average power for pumping optical parametric amplifiers. In *CLEO: Science and Innovations*, pages CTh5C–6. Optical Society of America, 2013.

[141] M Hentschel, R Kienberger, Ch Spielmann, Georg A Reider, N Milosevic, Thomas Brabec, Paul Corkum, Ulrich Heinzmann, Markus Drescher, and Ferenc Krausz. Attosecond metrology. *Nature*, 414(6863):509, 2001.

[142] Sabine Keiber, Shawn Sederberg, Alexander Schwarz, Michael Trubetskov, Volodymyr Pervak, Ferenc Krausz, and Nicholas Karpowicz. Electro-optic sampling of near-infrared waveforms. *Nature Photonics*, 10(3):159, 2016.

[143] Hanieh Fattahi. Sub-cycle light transients for attosecond, X-ray, four-dimensional imaging. *Contemporary Physics*, 57(4):580–595, 2016.

[144] Shu-Wei Huang, Giovanni Cirmi, Jeffrey Moses, Kyung-Han Hong, Siddharth Bhardwaj, Jonathan R Birge, Li-Jin Chen, Enbang Li, Benjamin J Eggleton, Giulio Cerullo, et al. High-energy pulse synthesis with sub-cycle waveform control for strong-field physics. *Nature Photonics*, 5(8):475, 2011.

[145] Giulio Maria Rossi, Roland E Mainz, Fabian Scheiba, Yudong Yang, Giovanni Cirmi, and Franz X Kartner. Half-cycle mJ-level CEP-stable pulses from parametric waveform synthesis. In *Conference on Lasers and Electro-Optics/Pacific Rim*, pages F2A–1. Optical Society of America, 2018.

[146] Roland E Mainz, Yudong Yang, Giulio Maria Rossi, Fabian Scheiba, Giovanni Cirmi, and Franz X Kärtner. Controlled HHG with a sub-cycle mJ-level parametric waveform synthesizer. In *Conference on Lasers and Electro-Optics/Pacific Rim*, pages Th3B–5. IEEE, 2018.

[147] Vladimir Chvykov, Huabao Cao, Roland Nagymihaly, Mikhail P Kalashnikov, Nikita Khodakovskiy, Richard Glassock, Lutz Ehrentraut, Matthias Schnuerer, and Károly Osvay. High peak and average power Ti:sapphire thin disk amplifier with extraction during pumping. *Optics Letters*, 41(13):3017–3020, 2016.

[148] Hanieh Fattahi. Design of a multi-terawatt field synthesizer (LWS-pro). In *Third-generation femtosecond technology*, pages 107–126. Springer, 2016.

[149] Hanieh Fattahi, Ayman Alismail, Haochuan Wang, Jonathan Brons, Oleg Pronin, Theresa Buberl, Lénárd Vámos, Gunnar Arisholm, Abdallah M Azzeer, and Ferenc Krausz. High-power, 1-ps, all-Yb:YAG thin-disk regenerative amplifier. *Optics letters*, 41(6):1126–1129, 2016.

[150] Hanieh Fattahi, Alexander Schwarz, Xiao Tao Geng, Sabine Keiber, Dong Eon Kim, Ferenc Krausz, and Nicholas Karpowicz. Decoupling chaotic amplification and nonlinear phase in high-energy thin-disk amplifiers for stable OPCPA pumping. *Optics express*, 22(25):31440–31447, 2014.

[151] Clara J Saraceno, Florian Emaury, Cinia Schriber, Martin Hoffmann, Matthias Golling, Thomas Südmeyer, and Ursula Keller. Ultrafast thin-disk laser with 80 μJ pulse energy and 242 W of average power. *Optics Letters*, 39(1):9–12, 2014.

[152] Jonathan Brons, Vladimir Pervak, Elena Fedulova, Dominik Bauer, Dirk Sutter, Vladimir Kalashnikov, Alexander Apolonskiy, Oleg Pronin, and Ferenc Krausz. Energy scaling of kerr-lens mode-locked thin-disk oscillators. *Optics letters*, 39(22):6442–6445, 2014.

[153] Hanieh Fattahi, Catherine Yuriko Teisset, Oleg Pronin, Atsushi Sugita, Roswitha Graf, Vladimir Pervak, Xun Gu, Thomas Metzger, Zsuzsanna Major, Ferenc Krausz, et al. Pump-seed synchronization for MHz repetition rate, high-power optical parametric chirped pulse amplification. *Optics express*, 20(9):9833–9840, 2012.

[154] Alexander Schwarz, Moritz Ueffing, Yunpei Deng, Xun Gu, Hanieh Fattahi, Thomas Metzger, Marcus Ossiander, Ferenc Krausz, and Reinhard Kienberger. Active stabilization for optically synchronized optical parametric chirped pulse amplification. *Optics Express*, 20(5):5557–5565, 2012.

[155] ID Jung, FX Kärtner, Nl Matuschek, DH Sutter, F Morier-Genoud, G Zhang, U Keller, V Scheuer, M Tilsch, and T Tschudi. Self-starting 6.5-fs pulses from a Ti:sapphire laser. *Optics letters*, 22(13):1009–1011, 1997.

[156] Nikolai Tolstik, Andreas Pospischil, Evgeni Sorokin, and Irina T Sorokina. Graphene mode-locked Cr:ZnS chirped-pulse oscillator. *Optics express*, 22(6):7284–7289, 2014.

[157] Daniel Herrmann, Laszlo Veisz, Raphael Tautz, Franz Tavella, Karl Schmid, Vladimir Pervak, and Ferenc Krausz. Generation of sub-three-cycle, 16 TW light pulses by using noncollinear optical parametric chirped-pulse amplification. *Optics letters*, 34(16):2459–2461, 2009.

[158] Christian Homann, Maximilian Bradler, Michael Förster, Peter Hommelhoff, and Eberhard Riedle. Carrier-envelope phase stable sub-two-cycle pulses tunable around 1.8 μm at 100 kHz. *Optics letters*, 37(10):1673–1675, 2012.

[159] S Hädrich, J Rothhardt, M Krebs, S Demmler, J Limpert, and A Tünnermann. Improving carrier-envelope phase stability in optical parametric chirped-pulse amplifiers by control of timing jitter. *Optics letters*, 37(23):4910–4912, 2012.

[160] J Galinis, G Tamošauskas, I Gražulevičiūtė, E Keblytė, V Jukna, and A Dubietis. Filamentation and supercontinuum generation in solid-state dielectric media with picosecond laser pulses. *Physical Review A*, 92(3):033857, 2015.

[161] Anne-Laure Calendron, Hüseyin Çankaya, Giovanni Cirmi, and Franz X Kärtner. White-light generation with sub-ps pulses. *Optics express*, 23(11):13866–13879, 2015.

[162] OH Heckl, Clara J Saraceno, CRE Baer, Thomas Südmeyer, YY Wang, Yu Cheng, F Benabid, and Ursulla Keller. Temporal pulse compression in a xenon-filled Kagome-type hollow-core photonic crystal fiber at high average power. *Optics express*, 19(20):19142–19149, 2011.

[163] Lauryna Lotscher, Lenard Vamos, Laszlo Veisz, and Alexander Apolonski. Long-term stability of nonlinear pulse compression using solid-core large-mode-area fibers. *Journal of Lasers, Optics & Photonics*, 2(3), 2015.

[164] Ieva Gražulevičiūtė, Milda Skeivytė, Enrika Keblytė, Justinas Galinis, Gintaras Tamošauskas, and Audrius Dubietis. Supercontinuum generation in YAG and sapphire with picosecond laser pulses. *Lithuanian Journal of Physics*, 55(2), 2015.

[165] Giulio Cerullo, A Baltuška, Oliver D Mücke, and Caterina Vozzi. Few-optical-cycle light pulses with passive carrier-envelope phase stabilization. *Laser & Photonics Reviews*, 5(3):323–351, 2011.

[166] Robert A Kaindl, Matthias Wurm, Klaus Reimann, Peter Hamm, Andrew M Weiner, and Michael Woerner. Generation, shaping, and characterization of intense femtosecond pulses tunable from 3 to 20 μm. *JOSA B*, 17(12):2086–2094, 2000.

[167] H Pires, M Baudisch, D Sanchez, M Hemmer, and Jens Biegert. Ultrashort pulse generation in the mid-IR. *Progress in Quantum Electronics*, 43:1–30, 2015.

[168] Valentin Petrov. Frequency down-conversion of solid-state laser sources to the mid-infrared spectral range using non-oxide nonlinear crystals. *Progress in Quantum Electronics*, 42:1–106, 2015.

[169] Matthias Hohenleutner, Fabian Langer, Olaf Schubert, Matthias Knorr, U Huttner, Stephan W Koch, M Kira, and Rupert Huber. Real-time observation of interfering crystal electrons in high-harmonic generation. *Nature*, 523(7562):572–575, 2015.

[170] Florian Adler, Michael J Thorpe, Kevin C Cossel, and Jun Ye. Cavity-enhanced direct frequency comb spectroscopy: technology and applications. *Annual Review of Analytical Chemistry*, 3:175–205, 2010.

[171] Albert Schliesser, Nathalie Picqué, and Theodor W Hänsch. Mid-infrared frequency combs. *Nature photonics*, 6(7):440, 2012.

[172] Henry Timmers, Abijith Kowligy, Alex Lind, Flavio C Cruz, Nima Nader, Myles Silfies, Gabriel Ycas, Thomas K Allison, Peter G Schunemann, Scott B Papp, et al. Molecular fingerprinting with bright, broadband infrared frequency combs. *Optica*, 5(6):727–732, 2018.

[173] Jens Biegert, Philip K Bates, and Olivier Chalus. New mid-infrared light sources. *IEEE Journal of Selected Topics in Quantum Electronics*, 18(1):531–540, 2011.

[174] Gunnar Arisholm. General numerical methods for simulating second-order nonlinear interactions in birefringent media. *JOSA B*, 14(10):2543–2549, 1997.

[175] Gunnar Arisholm. Advanced numerical simulation models for second-order nonlinear interactions. In *Laser Optics' 98: Fundamental Problems of Laser Optics*, volume 3685, pages 86–97. International Society for Optics and Photonics, 1999.

[176] Kiyoshi Kato, Kentaro Miyata, Ludmila Isaenko, Sergei Lobanov, Vitaliy Vedenyapin, and Valentin Petrov. Phase-matching properties of $LiGaS_2$ in the 1.025–10.5910 μm spectral range. *Optics letters*, 42(21):4363–4366, 2017.

[177] John C Travers, Wonkeun Chang, Johannes Nold, Nicolas Y Joly, and Philip St J Russell. Ultrafast nonlinear optics in gas-filled hollow-core photonic crystal fibers. *JOSA B*, 28(12):A11–A26, 2011.

[178] Tatiana Amotchkina, Hanieh Fattahi, Yurij A Pervak, Michael Trubetskov, and Vladimir Pervak. Broadband beamsplitter for high intensity laser applications in the infra-red spectral range. *Optics express*, 24(15):16752–16759, 2016.

[179] Hanieh Fattahi. *Third-Generation Femtosecond Technology*. Springer, 2015.

[180] K Kato. Temperature-tuned 90^o phase-matching properties of lib_3o_5. *IEEE journal of quantum electronics*, 30(12):2950–2952, 1994.

[181] Michael Porer, Jean-Michel Ménard, and Rupert Huber. Shot noise reduced terahertz detection via spectrally postfiltered electro-optic sampling. *Optics letters*, 39(8):2435–2438, 2014.

[182] Wolfgang Schweinberger, Lenard Vamos, Jia Xu, Syed A Hussain, Christoph Baune, Sebastian Rode, and Ioachim Pupeza. Interferometric delay tracking for low-noise Mach-Zehnder-type scanning measurements. *Optics Express*, 27(4):4789–4798, 2019.

[183] Richard G Brewer and RL Shoemaker. Optical free induction decay. *Physical Review A*, 6(6):2001, 1972.

[184] Ayman Alismail, Haochuan Wang, Gaia Barbiero, Syed Ali Hussain, Wolfgang Schweinberger, Ferenc Krausz, and Hanieh Fattahi. Near-infrared molecular fieldoscopy of water. In *Multiphoton Microscopy in the Biomedical Sciences XIX*, volume 10882, page 1088231. International Society for Optics and Photonics, 2019.

[185] Haochuan Wang, Ayman Alismail, Gaia Barbiero, Maximilian Wendl, and Hanieh Fattahi. Cross-polarized, multi-octave supercontinuum generation. *Optics letters*, 42(13):2595–2598, 2017.

[186] Binbin Zhou, Hairun Guo, and Morten Bache. Energetic mid-ir femtosecond pulse generation by self-defocusing soliton-induced dispersive waves in a bulk quadratic nonlinear crystal. *Optics express*, 23(5):6924–6936, 2015.

[187] Binbin Zhou and Morten Bache. Dispersive waves induced by self-defocusing temporal solitons in a beta-barium-borate crystal. *Optics letters*, 40(18):4257–4260, 2015.

[188] Katarzyna Krupa, Alexis Labruyère, Alessandro Tonello, BM Shalaby, Vincent Couderc, Fabio Baronio, and AB Aceves. Polychromatic filament in quadratic media: spatial and spectral shaping of light in crystals. *Optica*, 2(12):1058–1064, 2015.

[189] Rosvaldas Šuminas, Gintaras Tamošauskas, Vytautas Jukna, Arnaud Couairon, and Audrius Dubietis. Second-order cascading-assisted filamentation and controllable supercontinuum generation in birefringent crystals. *Optics express*, 25(6):6746–6756, 2017.

[190] Kale Beckwitt, Frank W Wise, Liejia Qian, Larry A Walker, and Edesly Canto-Said. Compensation for self-focusing by use of cascade quadratic nonlinearity. *Optics letters*, 26(21):1696–1698, 2001.

[191] R Šuminas, G Tamošauskas, G Valiulis, and A Dubietis. Spatiotemporal light bullets and supercontinuum generation in β-BBO crystal with competing quadratic and cubic nonlinearities. *Optics letters*, 41(9):2097–2100, 2016.

[192] RA Ganeev, IA Kulagin, AI Ryasnyansky, RI Tugushev, and T Usmanov. Characterization of nonlinear optical parameters of KDP, $LiNbO_3$ and BBO crystals. *Optics communications*, 229(1-6):403–412, 2004.

[193] RA Ganeev, IA Kulagin, AI Ryasnyanskii, RI Tugushev, and T Usmanov. The nonlinear refractive indices and nonlinear third-order susceptibilities of quadratic crystals. *Optics and Spectroscopy*, 94(4):561–568, 2003.

[194] Matteo Conforti and Fabio Baronio. Extreme high-intensity and ultrabroadband interactions in anisotropic β-BaB_2O_4 crystals. *JOSA B*, 30(4):1041–1047, 2013.

[195] D Majus, G Tamošauskas, I Gražulevičiūtė, N Garejev, A Lotti, A Couairon, D Faccio, and A Dubietis. Nature of spatiotemporal light bullets in bulk Kerr media. *Physical review letters*, 112(19):193901, 2014.

[196] A Brodeur and SL Chin. Band-gap dependence of the ultrafast white-light continuum. *Physical review letters*, 80(20):4406, 1998.

[197] Johannes Weitenberg, Tobias Saule, Jan Schulte, and Peter Rußbüldt. Nonlinear Pulse Compression to Sub-40 fs at 4.5 μJ Pulse Energy by Multi-Pass-Cell Spectral Broadening. *IEEE Journal of Quantum Electronics*, 53(6):1–4, 2017.

[198] John M Dudley, Goëry Genty, and Stéphane Coen. Supercontinuum generation in photonic crystal fiber. *Reviews of modern physics*, 78(4):1135, 2006.

[199] Qitian Ru, Nathaniel Lee, Xuan Chen, Kai Zhong, Georgiy Tsoy, Mike Mirov, Sergey Vasilyev, Sergey B Mirov, and Konstantin L Vodopyanov. Optical parametric oscillation in a random polycrystalline medium. *Optica*, 4(6):617–618, 2017.

[200] Martin Van Exter, Ch Fattinger, and D Grischkowsky. Terahertz time-domain spectroscopy of water vapor. *Optics letters*, 14(20):1128–1130, 1989.

[201] Iouli E Gordon, Laurence S Rothman, Christian Hill, Roman V Kochanov, Y Tan, Peter F Bernath, Manfred Birk, V Boudon, Alain Campargue, KV Chance, et al. The HITRAN2016 molecular spectroscopic database. *Journal of Quantitative Spectroscopy and Radiative Transfer*, 203:3–69, 2017.

Acknowledgements

At this moment, I would like to express my sincere gratitude to many people, without their help this work would not have been done. My eternal gratitude goes to:

Prof. Dr. Ferenc Krausz for providing me the opportunity to join LAP group and conduct PhD research. Thank you for your invaluable guidance and continuous support of the projects during my entire PhD. Your passion, vision and power of execution towards science and research greatly encouraged me.

Dr. Hanieh Fattahi for being my immediate supervisor and your patient guidance of my PhD project. I leanred a lot from you, and it was always pleasure to work and discuss with you during the last 5 years. Your enthusiasm towards science greatly affected me (and also Ayman I believe). The group "Hayha" will be always in my memory.

Prof. Dr. Matthias Kling for being my immediate supervisor and taking care of my contract during the last year of my PhD. Without you, I would have faced lots of difficulties during coronavirus crisis.

Dr. Ayman Alismail for being a wonderful team mate and office mate, for those lab time together in the LEX cleanroom. Your calm and optimistic character together with your deep knowledge about our laser system helped us to go through many laser broken moments. And a big thank you for your generosity in every aspect.

Gaia Barbiero for the constant help during the "RED" project. Your spirit of tidy up things changed the cleanroom and also largely affected me in the daily life.

Previous team members, Theresa Buberl, Najd Altwaijry, Maximilian Wendl, and Naeem Ahmad. Thank you all for the assitance and cooperation throughout this work. It was an honor to work with you all.

Dr. Helena Barros and Dr. Zsuzsanna Major for former direct supervision.

MPQ and LMU colleagues: Dr. Thomas Nubbemeyer, Dr. Moritz Ueffing, Martin Kaumanns, Florian Saran, Dr. Lénárd Vámos, Dr. Jonathan Brons, Prof. Dr. Oleg Pronin, Dr. Nicholas Karpowicz, Dr. Matthew Weidman, Dr. Wolfgang Schweinberger, Syed Ali Hussain, Dr. Jinwei Zhang and Dr. Bo-Han Chen for the discussion and contribution to this work.

Dr. Gunnar Arisholm for the collaboration on "SISYFOS" simulation. And Dr. Felix Köttig for the collaboration on SR-PCF project.

Dr. Vladimir Pervak and Dr. Tatiana Amotchkina for designing and fabricating the broadband beam splitters and various optics.

The whole LAP group, it is a pleasure to work in such a group full of talented scientists from different fields.

The IMPRS-APS for the scholarship and continuous support.

My father and mother for the spiritual support from the other side of the world.

My wife Xin, for endless love and constant support. You are truly the backstage hero in my life.